Numerical Study of the Morphological Instability of Metallic Nanowires

Auteur : Eloudrhiri, Rayane
Promoteur(s) : Nguyen, Ngoc Duy
Faculté : Faculté des Sciences appliquées
Diplôme : Master en ingénieur civil physicien, à finalité approfondie
Année académique : 2024-2025
URI/URL : http://hdl.handle.net/2268.2/24702

University of Liège
School of Engineering and Computer Science

Numerical study of the morphological instability of metallic nanowires

Academic supervisor
Prof. Ngoc Duy Nguyen

Jury members
Prof. David Colignon
Prof. Benoît Vanderheyden

Master's thesis completed by Rayane Eloudrhiri
in order to obtain the degree of Master of Science in Engineering Physics

Academic year 2024 – 2025

Abstract

Metallic nanowire networks are increasingly investigated as potential transparent conductive materials (TCMs) in electronic and optoelectronic applications. However, their thermal stability remains a major challenge due to the morphological instability that leads to nanowire breakup at elevated temperatures. The aim of this thesis is to analyze and characterize the breakup dynamics of metallic nanowires under surface-driven evolution, in order to provide insights into the optimization of nanowire networks. To this end, a diffuse-interface phase-field model based on the Cahn–Hilliard equation is developed and validated.

Following a detailed theoretical and numerical foundation, the phase-field model is implemented with a semi-implicit Fourier spectral scheme and a diffuse filtering scheme, to provide a more stable scheme to numerical oscillations and subsequent instabilities. An in-depth parametric study of free-standing nanowires in two configurations, single wires and junctions, is performed. Scaling laws for breakup time t_b and instability wavelength λ are systematically derived as functions of the configuration geometrical properties. Results confirm a $t_b \propto R^4$ scaling and instability wavelengths $\lambda \geq \lambda_c$ for finite-length nanowires, consistent with the predictions of Nichols and Mullins. Additionally, the influence of the initial morphology is investigated, comparing the idealized circular cross-section to a closer representation of the real structure of silver nanowires, namely a pentagonal cross-section. The results show faster breakup dynamics due to the high curvature at the corners of the pentagonal cross-section, revealing the importance of considering realistic geometries in phase-field modeling.

The phase-field model is extended using the Smoothed Boundary Method (SBM) to simulate substrate-supported nanowires. The results demonstrate a consistent slowdown in the instability dynamics due to the restriction of perturbation modes, as predicted by McCallum *et al.* . Scaling laws from the free-standing case are preserved, confirming the robustness of the phase-field approach.

Finally, the work concludes by proposing future extensions to account for grain-level anisotropy, electro-thermo-mechanical coupling, and mesh adaptivity. These improvements aim to enhance the predictive capabilities of phase-field modeling in a diversity of real-world nanowire applications.

Résumé

Les réseaux de nanofils métalliques suscitent un intérêt croissant en tant que matériaux transparents conducteurs (TCMs) pour les applications en électronique et en optoélectronique. Toutefois, leur stabilité thermique reste un enjeu majeur en raison de l'instabilité morphologique qui conduit à la fragmentation des nanofils à haute température. L'objectif de ce mémoire est d'analyser et de caractériser la dynamique de fragmentation des nanofils métalliques soumise à une évolution de surface, afin de proposer des pistes d'optimisation pour la stabilité des réseaux de nanofils. Pour cela, un modèle '*phase-field*', basé sur l'équation de Cahn–Hilliard, est développé et validé.

Après avoir posé un cadre théorique et numérique, le modèle phase-field est implémenté à l'aide d'un schéma spectral de Fourier semi-implicite couplé à un '*diffuse filtering scheme*', dans l'objectif d'obtenir une meilleure stabilité face aux oscillations numériques et aux instabilités associées. Une étude paramétrique approfondie est menée sur des nanofils en suspension libre, dans deux configurations : un nanofil isolé et une jonction de nanofils. Des lois en puissance reliant le temps de fragmentation t_b et la longueur d'onde λ de l'instabilité aux propriétés géométriques des configurations sont systématiquement établies. Les résultats confirment une loi de type $t_b \propto R^4$ et une longueur d'onde critique $\lambda \geq \lambda_c$ pour les nanofils de longueur finie, en accord avec les prédictions de Nichols et Mullins. De plus, l'influence de la morphologie initiale est étudiée en comparant la section circulaire idéalisée à une représentation plus réaliste des nanofils d'argent, à savoir une section pentagonale. Les résultats révèlent une dynamique de fragmentation accélérée en raison de la forte courbure aux sommets, soulignant l'importance d'intégrer des géométries réalistes dans les modèles '*phase-field*'.

Le modèle est ensuite étendu à l'aide de la Smoothed Boundary Method (SBM) pour simuler des nanofils déposés sur substrat. Les résultats montrent un ralentissement cohérent de la dynamique d'instabilité, dû à la restriction des modes de perturbation, conformément aux prédictions de McCallum *et al.* Les lois en puissance observées dans le cas suspendu sont conservées, attestant de la robustesse de l'approche phase-field.

Enfin, le travail se conclut par des perspectives d'extension du modèle pour intégrer l'anisotropie à l'échelle des grains, le couplage électro-thermo-mécanique, ainsi que l'adaptativité du maillage. Ces améliorations visent à renforcer les capacités prédictives de la modélisation par phase-field dans une variétés d'applications réelles de nanofils.

Acknowledgments

Over the past year, and throughout the last years in general, I have been fortunate enough to be surrounded by many people who brought me their support. I would like to dedicate this section to them.

First and foremost, I would like to thank my academic supervisor, Prof. Nguyen, for his guidance, patience, and understanding. Your support has been invaluable, and I am grateful for the time you devoted to discussing my work. Your insights and suggestions have helped me improve both my research and my writing. Thanks to you, I am now armed and ready for the start of my research journey.

I would also like to thank Amaury Baret for his kindness, his patience, and his guidance throughout the years spent working on this thesis. Our discussions were not only insightful but also a real pleasure to have. You have had a significant role in sustaining my motivation and strengthening my desire to pursue a research career, and for that, I am grateful.

I also want to thank François Balty for his continuous support and careful review of this thesis, which has been of great help. I am grateful for the role you played in helping me grow as a researcher.

I also want to express my gratitude to the members of the research group for their support, encouragement. Their good mood and camaraderie made working in the lab a treat.

I also want to thank Guillian Bryndza for the many discussions we had around the topic of phase-field modeling, which helped me overcome several challenges during this work.

I would also like to thank my friends for their support and continuous help in keeping me motivated. A particular thank you to Charles Jacquet, Philippe Tevoedjre, and Guillaume Delporte, whose support throughout this endeavor has been invaluable. Our daily check-ins and academic support throughout this endeavor helped me stay calm and collected while strengthening my resilience, often, inspired by a citation from Camus, we would share when we felt down: '*One must imagine Sisyphus happy.*' I am equally thankful to Melissa Kaci, Julia Baumgarten, and my best friends Sebastien Rogister, Tom Dogné, and Noé Burnel, for sharing this experience with me.

Finally and most importantly, I could not conclude this section without giving my most heartfelt gratitude to my family for their unconditional love and support. Your trust, encouragement, and unwavering belief in me have given me the strength to stand where I am today.

Contents

Introduction

Context

Transparent electrodes (TEs) are essential in modern optoelectronic applications such as touchscreens, OLED displays, solar cells, and wearable electronics. Recently, with the increasing demand for flexible electronics and for low-cost processes, innovative transparent conducting materials (TCMs) are required to replace the industry standard, Indium-Tin Oxide (ITO), which suffers from their brittleness and scarcity [1–3]. In this context, metallic nanowires (NWs), especially polyol-grown silver (Ag) nanowires, have emerged as a promising alternative thanks to their remarkable opto-electronic properties, low cost and ease of manufacturing (e.g. liquid solution process) allowing industrial scaling [1, 4–6]. However, metallic nanowires suffers from a limited thermal stability [7]. When the temperature becomes sufficiently high (around $300 - 350\,°\mathrm{C}$ for AgNWs), the nanowires undergo a transformation into a series of evenly-spaced chunks which leads to the loss of conductivity of the network. This phenomenon is known as morphological instability and is a major limitation to technical applications where high-temperature annealing is required.

Objectives

The main goal of this thesis is to investigate the morphological instability of metallic nanowires numerically using the phase-field formalism, specifically the Cahn-Hilliard equation with variable mobility [8–13]. The goals are to further assess the relevance of the phase-field formalism by reproducing and extending on the work of Roy *et al.* [14]. A dimensional analysis of some key parameters of the morphological instability is performed. In addition, the impact of geometric features is studied to further approach the real structure of metallic nanowires. The phase-field formalism is then extended to consider the case of metallic nanowire networks deposited on a substrate. The Smoothed Boundary Method (SBM) [15] is used to model the boundary conditions at the nanowire-substrate interface. A parallel between the numerical results and the theoretical predictions of Nichols and Mullins [16, 17] and McCallum *et al.* [18] is then drawn out to further validate the approach.

Outline

This thesis is divided into five chapters.

The state of the art as well as the theoretical concept needed for understanding the work are presented in Chapter 1.

The methodology employed in the study is described in Chapter 2 where the implementation of the phase-field formalism is discussed. Numerical experiments are performed in order to validate the presented implementation and a further discussion on a first idealised description of a nanowire is performed.

In Chapter 3, the implemented model is used to extend the study on free-standing nanowires by providing a thorough non-dimensional analysis of the key parameters of the morphological instability. A first consideration of the initial morphology of the nanowires is then performed in order to assess possible discrepancies between the idealised structure of a nanowire and a closer representation of the real structure.

Then, in Chapter 4, the model is further extended to consider the influence of a flat substrate on which the nanowires have been deposited. The theory of the Smoothed Boundary Method (SBM) is introduced and discussed in the case of the phase-field formalism, deriving a contact angle boundary condition and discussing its relevance with the literature. The results for the case of a single nanowire on a substrate are presented and compared to the theoretical predictions of Nichols and Mullins.

Finally, Chapter 5 concludes the thesis by summarizing the findings and proposing directions for future work.

Chapter 1

State of the art

This first chapter introduces the context and the theoretical concepts needed for the study of the morphological instability of metallic nanowires. It is structured in three parts.
The notion of metallic nanowires (MNWs) is first introduced within the broader context of transparent conducting materials and electrodes. This section begins by defining transparent conducting materials (TCMs), discussing their various fields of applications and introducing the relevant properties and a means to compare different types of TCMs through a Figure of Merit (FoM). The focus then shifts to metallic nanowires, emphasizing their advantages over the currently most used TCM, Indium-Tin Oxides (ITOs). Different electrical activation methods are then reviewed, with a particular focus on thermal annealing, which sheds light on the thermal instability that takes place at the nanowire scale.
Following the introduction of the thermal instability, the second section focuses on the concept of morphological instability starting from the broad theoretical description first made by Plateau-Rayleigh in liquid-jets. The discrepancies between Plateau-Rayleigh predictions and what is observed experimentally are then discussed.
Finally, a detailed description of phase-field modeling theory, the approach applied in this study, is provided by first introducing its emergence in microstructural evolution studies and then detailing the mathematical formulation and the underlying physical principles.

1.1 Metallic nanowires

1.1.1 Transparent conducting materials

Transparent conducting materials (TCMs) constitute a special class of materials which exhibit both high electrical conductivity and high optical transparency [19]. In practice, materials which have high electrical conductivity, such as metals, are optically opaque whereas optically transparent materials such as glass, polymers or certain metal oxides are electrical insulators.

Optical Transparency and Electrical Conductivity

This tradeoff between electrical conductivity and optical transparency of solid media can be understood in a simplified fashion through energy bandgap theory in solid state physics. Indeed, electrical insulators are often optically transparent because of their large energy bandgap, i.e. an energy band in which electrons cannot be located, which allows photons from the visible spectrum to pass through leading to electronic transitions associated with an absorption process. On the other hand, metals have a high density of states at the Fermi level which leads to high electrical conductivity but also to high absorption of photons in the visible spectrum, associated to their opacity in the visible range. The difference between electrical insulating materials and metals is further illustrated in Figure 1.1. A more detailed description of energy band gap theory and photon absorption, can be found in Brennan [20] and similar textbooks.

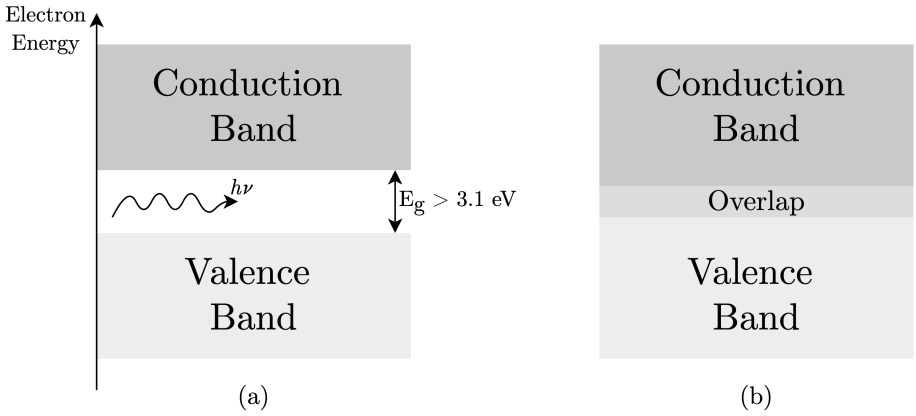

Figure 1.1. *Energy band diagram of* (a) *electrical insulators* (b) *metals. The photon energy* $E = h\nu$*, where* h *is Planck's constant and* ν *is the frequency of the incident light, can lead to absorption only if it is larger than the forbidden bandgap. Thus, if the bandgap energy if larger than the highest energy of the visible spectrum, i.e. in the near-ultraviolet range, the material is optically transparent.*

Classification of Transparent Conducting Materials

Since the discovery of wide bandgap (above 3.1 eV) semiconductors in the 1950s [3], TCMs have played an important role in many industrial applications such as solar cells, transparent heaters, touch screens, OLED displays and many others. TCMs are typically used as transparent (conducting) electrodes (TCEs or TEs) in their various applications, where the dual optimization of the electrical conductivity and the optical transparency is crucial. For instance, in solar cell applications, the optical transparency is provided by the transmittance coefficient in the visible spectrum, typically represented by the value at its mean wavelength, roughly 550 nm [21].
In 1976, Haacke proposed a Figure of Merit (FoM) to compare different families of TCMs for photovoltaic applications [22]. The proposed FoM is constructed as follows:

$$\text{FoM} = \frac{T^{10}}{R_s},$$

where the power of the transmittance T is chosen such that the FoM is maximized for transmittance values higher than 90%. Figure 1.2 presents a plot of transmittance as a function of the sheet resistance for different families of TCMs. The FoM iso-values lines provide a simple criterion for comparing their optoelectronic performance. The higher the FoM, the better the TCM is for optoelectronic applications. The region of interest can then be identified as the upper left corner of the plot, at high FoM values. Two families of TCMs lie in this region, transparent conducting oxides (TCOs), especially Indium-Tin Oxides, and metallic nanowire networks, especially silver-based nanowire networks (Ag-MNWs) [3].

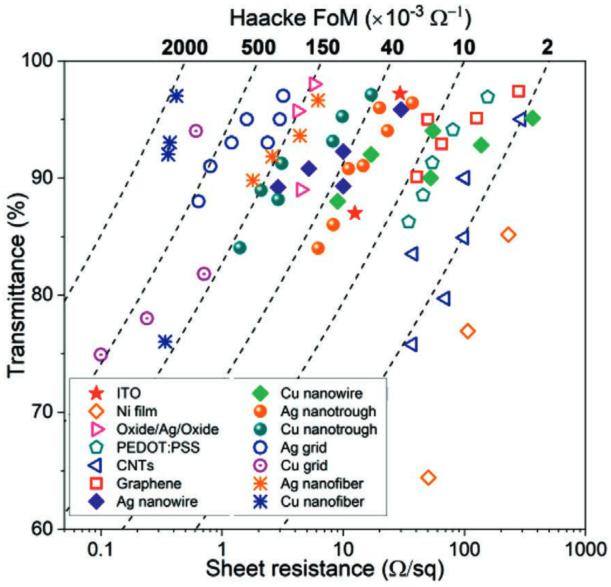

Figure 1.2. *Haacke's Figure of Merit (FoM) for different families of TCMs* [3]. *The iso-values lines represent the FoM. For increasing values of the FoM, the isolines are closer to the upper left corner where the transmittance is maximized and the sheet resistance is minimized. Emerging TCMs are compared to the industry leading ITOs.*

Transparent Conducting Oxides

Transparent conducting oxides (TCOs) and more particularly Indium-Tin Oxide (ITO) are the industry leading choice for transparent electrodes. They are heavily-doped wide bandgap (above 3.1 eV) semiconductors. After more than 60 years of research, ITO has now reached process stability and maturity [2]. However, with the fast growing technological market, new requirements for TCMs have surfaced. In particular, the market now aims towards flexible electronics, therefore the TEs required for these new devices must be able to bend without losing their functionality. Unfortunately, one of the major drawbacks of ITO films is their brittleness. In addition to their mechanical limitations, with the fast-growing demand of TEs, the scarcity of Indium and the high production cost in their synthesis [1] encouraged the search for alternatives which would alleviate these issues.
Thus the emerging TCMs must be low cost, use earth-abundant and non toxic chemical element, with competing conductivity and transparency to ITOs. This brings us to the core topic of this thesis: metallic nanowire network TCMs [2].

Metallic Nanowire Networks

Metallic nanowires (MNWs) are among the emerging TCMs and are one the most promising candidates, especially polyol-grown silver (Ag) nanowires [5]. Indeed, due to their intrinsically high electrical conductivity, tunable optical transparency and their relatively simple synthesis and deposition method, MNWs have the potential to replace ITOs. TCMs based on MNWs can be achieved by depositing a percolating network of MNWs onto an optically transparent substrate, such as glass. A network is said to be percolating when there exists at least one continuous path of conductive material from one side of the device to the other [4]. Thus the electrical conductivity is dependent on the density of the deposited MNWs [7, 23]. However, the denser the network, the less transparent it becomes. This tradeoff is one of the key elements in the optimization of MNW-based TCMs.

1.1.2 Electrical activation methods of Metallic Nanostructures

After depositing the MNWs, the network must be activated to ensure percolation since the contact resistance can be initially high between each nanowire [3]. This initially high resistance is caused by the initial point-like contact between each nanowire and can also be caused by organic residues which originates from the synthesis process and/or the solution based deposition. In the case of polyol grown nanowires, each nanowire are grown encapsulated in an organic shell of polyvinylpyrrolidone (PVP). The grown nanowires are then suspended in an organic solution (e.g. IPA). Additional details on the polyol process for metallic nanowires can be found in Sun *et al.* [5] and Nguyen *et al.* [3]. Therefore, activating the network requires a post-deposition treatment to promote the contact between each nanowires. There exists different post-deposition treatments, also referred to as activation methods: mechanical pressing, electrical annealing, thermal annealing, and others [6]. The most common one is thermal annealing, which consists in a gradual heating of the network leading to the decrease of the contact resistance [24].

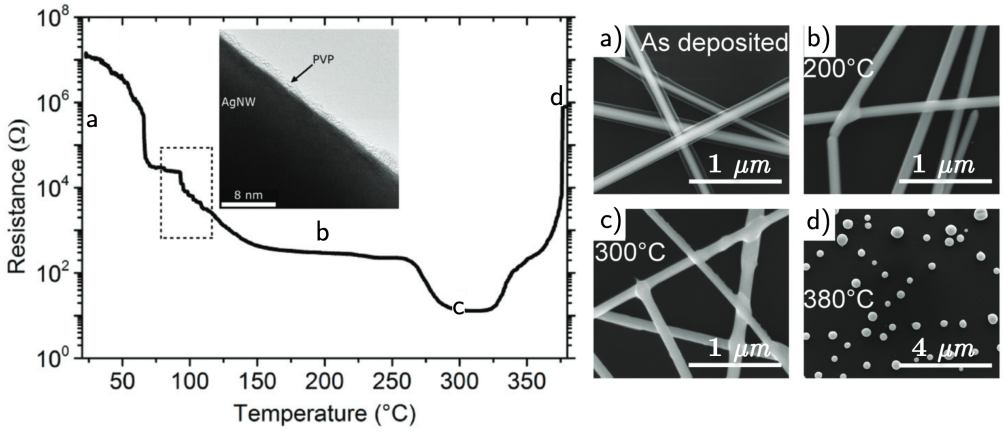

Figure 1.3. *Evolution of the electrical resistance with respect to the temperature during thermal annealing during a thermal ramp of* $15\,°C\,min^{-1}$. (a) *Scanning electron microscopy (SEM) image of the nanowire as deposited* (b) *Desorption of the organic residues and first occurence of observable local sintering* (c) *All junctions are sintered* (d) *Spheroidization of the whole network. Figure adapted from Langley et al.* [24].

Figure 1.3 shows the evolution of the electrical resistance of a AgNW network with respect to the temperature during thermal annealing. Three steps can be identified from it. Starting from the *in situ* nanowire network in Figure 1.3(a), the nanowires undergo,

1. Desorption of the organic residues (b)
2. Local sintering of the nanowires (b, c).
3. Spheroidization of the nanowires (d).

As can be seen from the figure, when the temperature becomes sufficiently high (in the range of $300 - 350\,°C$ for AgNW networks), the resistance increases rapidly and the network no longer percolates. Scanning electron microscopy (SEM) images reveal that the nanowires transform into a series of evenly-spaced dots which leads to the destruction of percolating paths across the network.

1.2 Morphological instability

In the literature, this phenomenon is often referred to as Plateau-Rayleigh instability, dewetting or spheroidization. This section focuses on the historical description of such instabilities and the discrepancies between the theoretical predictions and the experimental observations in metallic nanowires.

1.2.1 Theoretical description

In 1873, Joseph Plateau conducted a series of experiments which led to the observations of instability in liquid jets [25]. He observed that a *'vertically falling stream of water'* breaks up into a series of droplets if the length of the stream exceeds a multiple of the initial diameter of the stream. Later, in 1878, Lord Rayleigh provided a theoretical model to explain the phenomenon observed by Plateau [26]. His arguments were related on the minimization of surface energy. This analysis involves decomposing the initial capillary perturbation into a series of modes k, each growing at its own characteristic rate σ. His model confirmed Plateau's observations and predicted, by identifying the maximally growing mode, that the jet would break up into droplets with a characteristic wavelength of $\lambda = 9.016\,R_0$, with R_0 the initial radius of the jet. This phenomenon is now known as Plateau-Rayleigh instability.

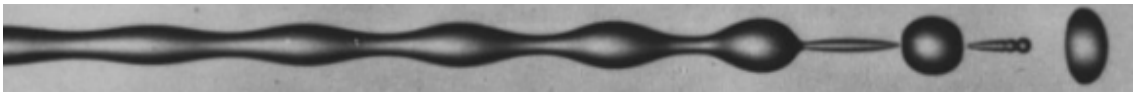

Figure 1.4. *Plateau-Rayleigh instability in a liquid jet. Adapted from* [27].

Following this description, Nichols and Mullins [16] worked on the stability of solids of revolution. By considering surface-driven mass transport as the primary driving force, they developed a numerical method to compute *'the kinetics of the shape changes of any solid of revolution'*. They found that the solution to a cylindrical rod is a series of equally-spaced spheres along the direction of the rod, which they named the spheroidization of the rod.

McCallum *et al.* [18] extended this work for the case of cylindrical rods deposited on a substrate with varying contact angle. Their work showed that the presence of the substrate provides a stabilizing effect to the morphological instability phenomenon. Indeed, their work showed an increasing trend of the non-dimensional growth rate σ_m with respect to the contact angle α modeling the presence of a substrate. The function relating σ_m to the contact angle α is represented in Figure 1.5.

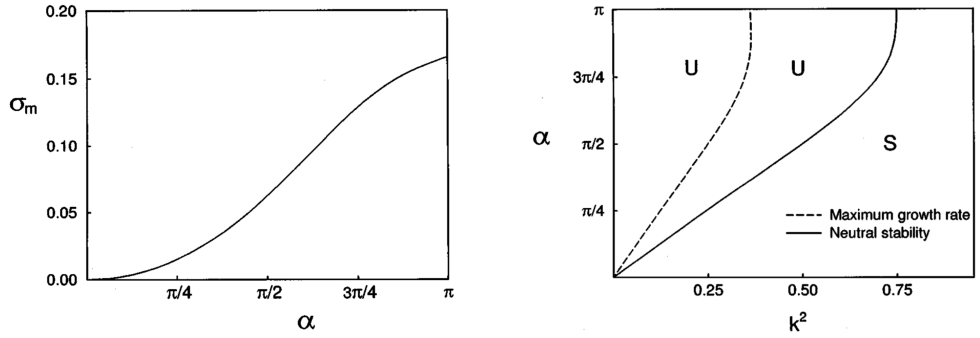

Figure 1.5. *Plot of* (a) *the maximum nondimensional growth rate* σ_m *with respect to the contact angle* α (b) *the (U)nstable and (S)table regions with respect to the contact angle* α. *The solid line represents the value of* k_c^2, *the critical nondimensional wavenumber associated to a nondimensional growth rate* $\sigma = 0$. *The dashed line represents the value of* k_m^2, *the nondimensional wavenumber associated to the maximum nondimensional growth rate* σ_m [18].

The maximally growing wavenumber, and consequently the wavelength of the instability, predicted by McCallum is of the same order of magnitude as the one predicted by Plateau-Rayleigh for free-standing jets. However, as the contact angle decreases, i.e. an increase of the contact angle α with the substrate, the maximally growing wavenumber k_m decreases. This results in a longer instability wavelength λ and a smaller growth rate σ_m, leading to delayed instability kinetics. The presence of the substrate is thus stabilizing.

1.2.2 Application to metallic nanowires

In their experimental work, Langley *et al.* [24] found that the distance between the nanoparticles after spheroidization is of the same order of magnitude as the one predicted by Plateau-Rayleigh but is slightly larger. Inspired by observations and by the work of McCallum, Balty *et al.* [28] showed that the predictions provided by McCallum's are in better agreement with the measurements in an extended series of experiments summarized in Figure 1.6. Knowing that, McCallum's model provides a good theoretical framework to understand the morphological instability of metallic nanowires, paving the way towards stabilization strategies and a better understanding of the mechanism at play at that scale.
However, the model is limited to the description of idealized infinitely long truncated cylinders, and cannot take into account the effect of a junction between two nanowires, the effect of the length/radius ratio, the effect of the crystalline nature of the nanowire which yields a pentagonal cross-section, and more.

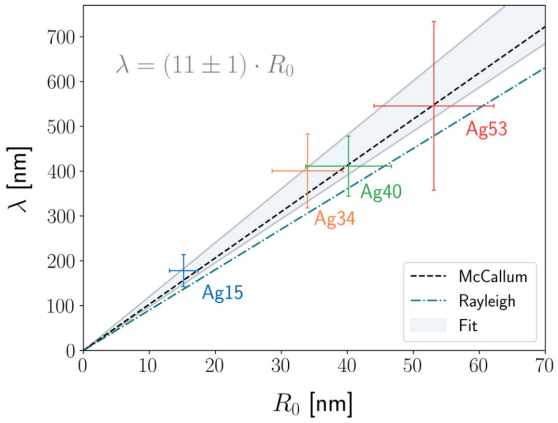

Figure 1.6. *Fitted mean instability wavelengths with respect to the initial mean radii R_0 of AgNWs samples. The grey area represents the confidence interval of the fitted curve. McCallum's theory predicts results closer to the experiments than Plateau-Rayleigh's* [28].

Numerical simulations are thus required to deepen the understanding of the phenomenon and to provide a more accurate and complete description of the morphological instability of metallic nanowires, which is the focus of this study. There exists several modeling theories one can utilize to model physics at the mesoscale, the scale encompassing the nanowire size, the scale in-between atomistic and macroscopic scales.
Molecular Dynamics (MD) is a powerful numerical tool for simulating the motion of atoms in a molecular system. However, MD is computationally expensive and is limited to the study of small systems over small time scales with time steps on the order of the femtoseconds [29]. It is thus ill-suited for the study of the morphological instability and the resulting necking of nanowires since it occurs over a range of a few seconds at around $T = 300\ ^\circ C$. One of the most promising theory for modeling physical processes at the mesoscale is the phase-field theory which gained popularity in the last decades for its versatility and ability to model complex geometries [30].

1.3 Background for phase-field modeling

In this section, both the theoretical context and the mathematical formulation of phase-field is presented. The interested reader is encouraged to consult the literature on which this section draws inspiration. Peter Voorhees, one of the leading experts in the field, put together a series of video capsules to introduce the general phase-field framework as well as the initial motivation behind phase-field [31]. Similarly, Moelans *et al.* provided an insightful introduction to phase-field, from the historical background to the mathematical and physical derivation of the formalism, with fine details [32]. Additional details on the mathematical and physical formulation as well as insights in numerical modeling of phase-field equations can be found in Lee *et al.* [11]. Information on practical numerical implementation of phase-field can be found in *Programming Phase-Field Modeling* by S. Bulent Biner [33]. In addition, researchers from the Center for Hierarchical Materials Design at Northwestern University and

the National Institute of Standards and Technology built `PFHub`, an online community which aimed at supporting phase-field researchers [34, 35], where one can find benchmark problems as well as open-source implementation of phase-field solvers.
The theoretical context presented here has been adapted from these sources to fit the scope of the thesis by laying down the initial motivation upon which phase-field emerged and the formulation condenses insights, highlighting the key concepts relevant to the study.

1.3.1 Theoretical context

In solid materials, many important processes take place at the mesoscale. Mesoscale processes can impact on the measured macro-properties of a system [32]. Thus, accurate models which simulate the physics at that scale are required to better understand and predict the properties of physical systems.
Typically, the sharp-interface approach is used to study the physics of heterogeneous material systems at the mesoscale. However, many processes at this scale suffer from this mathematical definition and become almost intractable using this approach. Interface tracking with complex geometries (e.g. during dendritic growths) and topological changes (e.g. merging of two particles) are particularly challenging [36].
In this context, the case of a precipitate β growth in a matrix α is considered to highlight the shortcomings of the sharp-interface approach. The situation is schematised in Figure 1.7.

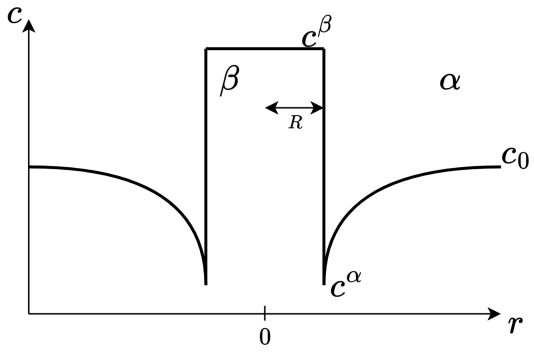

Figure 1.7. *Sharp interface approach to 1D growth of a spherical particle β of radius R in a matrix α. The figure represents the concentration profile along the radial direction. The concentration values c^β, c^α and c_0 are respectively the equilibrium concentration in the β phase, α phase and the alloy. Adapted from* [31, 32].

The precipitate in the β phase grows by diffusion. The concentration profile is solved using Fick's second law of diffusion [37] in both phases and the interface position, i.e. the radius R, is determined by the equilibrium condition at the interface. This writes as follows,

$$\begin{aligned} &\frac{\partial c^i}{\partial t} = D^i \nabla^2 c^i \quad , \quad i = \alpha, \beta \\ &\frac{\partial R}{\partial t} = D \frac{\partial c}{\partial r}\Big|_{r=R(t)} \\ &\mu^\alpha(c^\alpha_{int}) = \mu^\beta(c^\beta_{int}). \end{aligned} \tag{1.1}$$

The first equation, Fick's second law, is obtained by combining Fick's first law which states that the flux of particles is proportional to the gradient of concentration ∇c with the continuity equation [37]. The quantity D^i is the diffusion constant related to the phase i and c^i is the concentration of particles in the phase i. The second equation tracks the motion of the interface. Finally, the third equation describes the thermodynamic constraint which states that both phases are in equilibrium at the interface [11, 31, 32, 36, 37]. The issue with this approach is that both the concentration and radius update equations depend on the position of the interface which consequently depends on the composition in each phase. This kind of situtation is referred to as a free boundary problem, where the interface between phases is not fixed but evolves in time as part of the solution itself, rather than being known *a priori* [38].

A solution to this problem was introduced by Langer [39]. He proposed a description using a single equation which holds true in the entire domain. To achieve this, the sharp interface is approximated by a finite width interface, a so-called diffuse-interface, schematised in Figure 1.8. This approach was first thought to be *'too complex to be useful'* since it would require a fine enough mesh to render the diffuse-interface [31]. However, with the technological advances, the diffuse-interface approach is becoming the standard when studying microstructural evolution, in particular phase-field modeling.

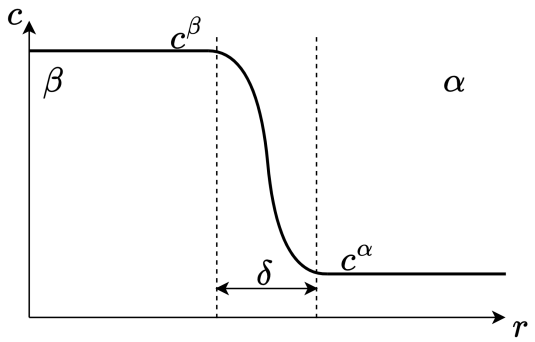

Figure 1.8. *Diffuse-interface approach to 1D growth of a spherical particle of radius R. Adapted from* [31, 32].

In this context, the microstructure is described by a set of continuous fields which vary smoothly across the interface. Within each phase, the field has the same value and meaning as in the sharp interface approach. The position of the free interface can be retrieved through contours of constant values of the field variable. In addition, no constraint is required at the interface. For example, consider the case of a binary system of composition c composed of an α and a β phase which respectively have a composition $c = c_\alpha^{eq}$ and $c = c_\beta^{eq}$ at equilibrium. The regions of the system where the field variable $c(\mathbf{x}, t) = c_\alpha^{eq}$ and $c(\mathbf{x}, t) = c_\beta^{eq}$ corresponds respectively to the α and β phase whereas the regions where $c(\mathbf{x}, t)$ is between c_α^{eq} and c_β^{eq} corresponds to the interface between both phases, as shown in Figure 1.9 [11].

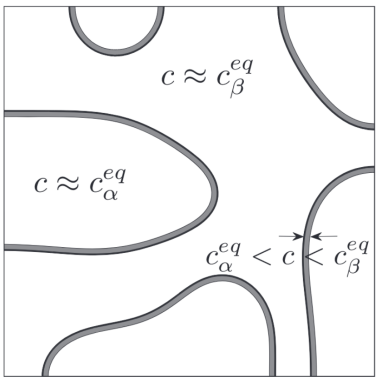

Figure 1.9. *Example of a two phase microstructure with a phase-field variable c in 2D.* [11].

1.3.2 Fundamental principles and Formulation

The microstructure is described by a set of continuous fields [8–11, 31, 33], i.e. the phase-field variables, field variables or order parameters. These variables can either be conserved or non-conserved depending on the phase-field model employed. A conserved order parameter often refers to the local composition (e.g. the local concentration c), whereas a non-conserved order parameter often refers to crystal structure or to the phase of a composition (e.g. solid-liquid). Conserved field variables satisfies a continuity equation which ensures conservation of the quantity whereas non-conserved field variables have no conservation constraint [8, 9].
The driving force of microstructural dynamics is the minimization of the free energy of the system, F, [8, 9, 31, 32] which can be written as,

$$F = F_{bulk} + F_{int} + F_{source} \ , \tag{1.2}$$

where F_{bulk}, F_{int} and F_{source} are respectively the free energy associated to the bulk of the system, to interfacial interactions and to additional sources of energy such as elastic strains, electromagnetic fields, and more [31, 32].
Classically, thermodynamic properties are assumed homogeneous throughout a system. However, in the case of phase-field modeling, the system is considered '*nonuniform*', i.e. '*a system having a spatial variation in one of its intensive scalar properties, such as composition or density*' [8]. The total free energy of a nonuniform system of volume Ω described by a conserved order parameter c is given by,

$$\begin{aligned} \mathcal{F}(c) &= \int_\Omega f d\Omega \ , \\ \text{with} \quad f &= f(c, \nabla c, \nabla^2 c, \ldots) \, . \end{aligned} \tag{1.3}$$

The local free energy density f can be expanded in a Taylor series around f_0, the free energy density of a uniform system or the bulk free energy density. Thus, the bulk free energy density f_0 represents the '*interaction of different components in a homogeneous system*' [40]. The thermodynamically relevant expression is logarithmic (Helmholtz) and is given by [11],

$$f_0(c) = \frac{1}{N_a}\{\omega c(1-c) + RT\left[(1-c)\ln(1-c) + c\ln c\right]\} \ , \tag{1.4}$$

with N_a the Avogadro number, ω the regular solution parameter, R the perfect gas constant, T the temperature and c the composition (more details in [11]).
In practice, the thermodynamically relevant expression of the free energy density of an homogeneous system is replaced by a polynomial approximation of degree four for practical and computational reasons,

$$f_0(c) = wg(c) = w(c - c_\alpha)^2(c - c_\beta)^2 \ , \tag{1.5}$$

where $g(c)$ is the polynomial function, w, c_α and c_β are constants chosen to fit the positions of the minima and the curvature at the minima, as shown in Figure 1.10.

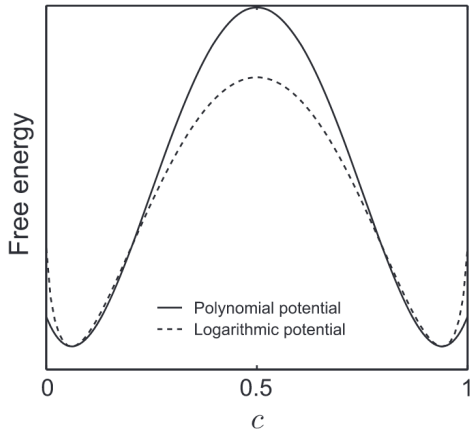

Figure 1.10. *Bulk free energy density f_0 of a binary mixture and its quartic approximation.* [11]

After some algebraic manipulations and assuming the system to be centrosymmetric, and thus isotropic, the free energy functional can be rewritten as,

$$\mathcal{F}(c) = \int_\Omega f_0(c) + \frac{\kappa}{2}|\nabla c|^2 d\Omega \ , \tag{1.6}$$

with κ the gradient energy coefficient. A more thorough derivation of the total free energy functional of a nonuniform isotropic binary system is available in Moelans *et al.* [32] or in Lee *et al.* [11].
This expression of the free energy functional is known as the Ginzburg-Landau [11, 31, 32] free energy functional. Thermodynamics informs us that for a closed system, at fixed temperature and volume, to be in equilibrium, its free energy must be minimized. Thus, an equilibrium state is reached when the composition field c is such that it extremizes the free energy functional,

$$\delta\mathcal{F} = 0 \ . \tag{1.7}$$

After some variational calculus, this leads to the Euler-Lagrange equation [31],

$$\frac{\partial f_0}{\partial c} - \kappa\nabla^2 c = 0 \ . \tag{1.8}$$

The solution c to this equation extremizes the free energy functional. However, there are no constraint on the average value of c in the system, i.e. the total mass is not conserved. To ensure mass conservation, a constraint is added through a Lagrange multiplier μ which leads to,

$$\mu = \frac{\delta \mathcal{F}}{\delta c} = \frac{\partial f_0}{\partial c} - \kappa \nabla^2 c \tag{1.9}$$

the generalized chemical potential [31].
Some authors skip the discussion on the constraint and directly define the chemical potential as the variational derivative of the free energy functional with respect to the order parameter c. The order parameter c is a conserved quantity and satisfies the continuity equation,

$$\frac{\partial c}{\partial t} + \nabla \cdot \mathbf{J} = 0 \ , \tag{1.10}$$

where $\mathbf{J}$, the diffusion flux, is given by,

$$\mathbf{J} = -M \nabla \mu \ , \tag{1.11}$$

where the the gradient of the chemical potential $\nabla \mu$ is the driving force of the diffusion, the thermodynamic force, and M is the mobility function [31, 32]. The mobility function M can be a function of the order parameter c as it stems from the combined effect of atomic mobilities of the system constituents [31, 32]. This leads to the Cahn-Hilliard equation,

$$\frac{\partial c}{\partial t} = \nabla \cdot \left[M \nabla \left(\frac{\partial f_0}{\partial c} - \kappa \nabla^2 c \right) \right] \ . \tag{1.12}$$

1.3.3 Applications

Phase-field modeling has been used in a wide range of applications from material sciences to biology and biomedical sciences (e.g. tumor growth [41]). In materials science, different scales can be identified. At the mesoscale, usage of the technique was reported in fracture mechanics [42], fluid dynamics [43], whereas at the microscale it was used for the study of solidification [44], grain growth and spinodal decomposition [45], coarsening kinetics [12, 46]. Indeed, provided a careful design of the free energy functional $\mathcal{F}$ of the studied system, various multiphysics problems can be studied. Following this downward trend in system scale, the phase-field formalism has eventually been extended to nanoscale systems.
Chockalingam *et al.* studied the sintering mechanism of silver nanoparticles by exploring the phase-field formalism. They were able to compare their numerical results with experimental observations which highlighted the strengths of the phase-field formalism at simulating physics at the nanoscale [47]. However, the considered model of sintering was limited to the case of 2D circular particles. Roy *et al.* [14] extended the study of the sintering mechanism to the case of 3D nanowires. They were able to produce results which were in good agreement with experimental observations in their idealised case of a free-standing nanowire configuration. The goal of the present work is notably to extend the results of Roy *et al.* to a more complex case of nanowire configurations, i.e. nanowires deposited on a substrate. This configuration would account for the interaction of the nanowires with the flat substrate on which they are deposited, thus improving the model of nanowire sintering.

Chapter 2

Methodology

This chapter aims at introducing the methodology used throughout this work, i.e. the phase-field model utilized as well as its specifics. First, a section is dedicated to the employed Variable Mobility Cahn-Hilliard equation. Then, the numerical method used to implement the model is detailed. Subsequently, numerical experiments are performed using the implemented model in order to asses its consistency and stability. The model solutions are then compared to peer-reviewed benchmark problems [38] in order to validate the model. Finally, some typical results concerning surface-enhanced breakups in free-standing nanowires are presented as a direct follow-up to Roy *et al.*'s work [14] which will be further extended in Chapter 3 and Chapter 4.

2.1 Phase-field modeling of a binary mixture

2.1.1 Formulation

The Cahn-Hilliard equation, derived in Section 1.3, is a fourth-order partial differential equation which describes the evolution of a conserved order parameter c. The equation writes as,

$$\frac{\partial c}{\partial t} = -\nabla \cdot \mathbf{J} = -\nabla \cdot (-M \nabla \mu) \ , \tag{2.1}$$

where $\mathbf{J}$ is the previously defined diffusion flux in Equation 1.11, M is the mobility function and μ is the generalized chemical potential defined as the variational derivative of the total free energy functional $\mathcal{F}$,

$$\mu = \frac{\delta \mathcal{F}}{\delta c} = \frac{\partial f_0}{\partial c} - \kappa \Delta^2 c = w g'(c) - \kappa \Delta^2 c \tag{2.2}$$

where $\mathcal{F}$ is the Ginzburg-Landau free energy functional describing isotropic binary systems, f_0 is the bulk free energy density, $wg'(c)$ its derivative with respect to c, w the height of the double well potential and κ is the gradient energy coefficient.
The Ginzburg-Landau free energy functional is defined as,

$$\mathcal{F}(c) = \int_\Omega f_0(c) + \frac{\kappa}{2} |\nabla c|^2 d\Omega \ . \tag{2.3}$$

2.1.2 Variable Mobility

Usually, the mobility M is considered constant and uniform across the domain which describes bulk-driven phase separation [12, 31]. However, as mentioned in the phase-field formulation in Section 1.3, the mobility can be a function of the composition i.e. the order parameter c [32]. Making the mobility dependent on the order parameter leads to changes in the phase separation dynamics. Most commonly used mobility functions are quadratic or quartic polynomials of the order parameter c which penalize the mobility in the bulk to enhance the mobility at the interface, thus leading to surface enhanced phase separation [10, 12, 48, 49]. The mobility function used in this study was introduced by Roy *et al.* [14] and is defined as,

$$M(c) = 2M_0\sqrt{|c - c^2|}\ , \tag{2.4}$$

where M_0 is the maximum mobility and c is the order parameter. It is an adaptation of the classical mobility function $M(c) = |1 - c^2|$ proposed by Langer *et al.* [13] for order parameters $c \in [-1, 1]$. Both functions are shown in Figure 2.1.

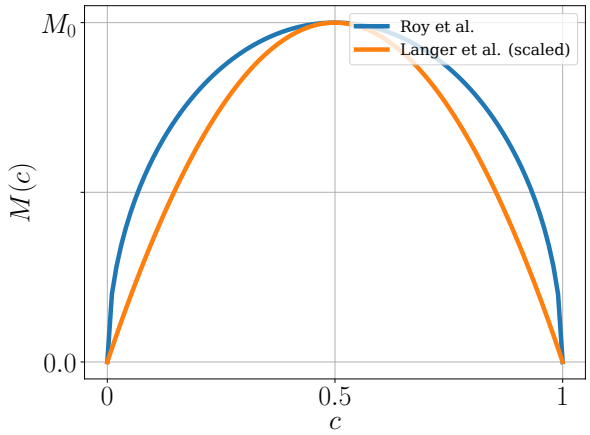

Figure 2.1. *Comparison of the mobility function proposed by Roy et al.* [14] *and the classical mobility function proposed by Langer et al* [13]. *The former has a smoother transition between the interfacial mobility and the bulk mobility. This smoother transition effectively reduces the stiffness of the equation, i.e. it improves its overall numerical stability* [50, 51].

The above figure shows the variable mobility with respect to the order parameter c. The mobility is maximum at the interface defined as $c \approx 0.5$ and minimum in the bulk defined as $c \approx 0$ and $c \approx 1$. This leads to surface-driven dynamics in the system. The mobility function can be found in different forms in the literature, but they all can be rewritten as [48],

$$M(c) = 4^n M_0 |c - c^2|^n\ . \tag{2.5}$$

2.1.3 Surface Diffusion in Silver Nanowires

Atomic diffusion is a key parameter when dealing with nanostructural evolution. In the case of metallic nanowires, Rhead [52] showed through experimental work that surface diffusion

is the dominant mass transport mechanism compared to bulk and grain diffusion. It was showed that self-diffusion coefficients fit an Arrhenius law, i.e. $D_s = D_0 \exp(Q_s/kT)$, with D_s, D_0 and Q_s respectively the self-diffusion coefficient, a preexponential constant and the activation energy for energy. Figure 2.2 shows the Arrhenius plot of silver surface, grain and bulk self-diffusion.

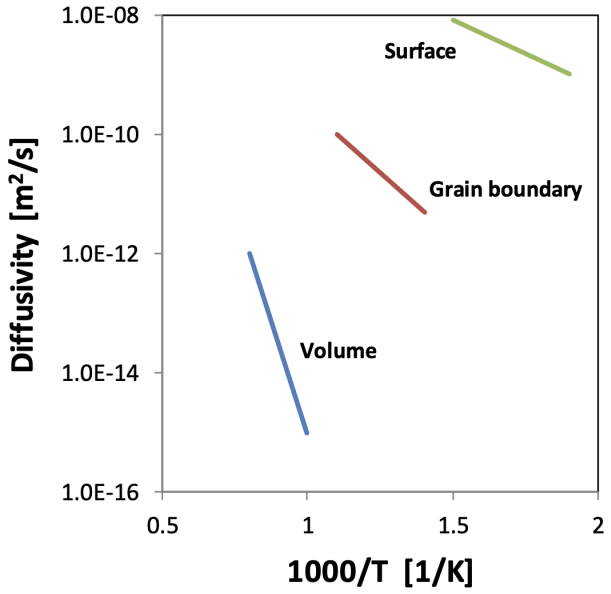

Figure 2.2. *Arrhenius plot of silver self-diffusion as a function of temperature.* [53]

It can be seen that at temperature where the morphological instability in AgNWs is observed i.e. $1/T \approx 1.6\,K^{-1}$ or $T = 600\,K$ [24], the surface self-diffusion is the dominant mechanism. Indeed, one can see that several orders of magnitude separate surface self-diffusion from grain boundary and bulk self-diffusion.
The mobility function $M(c)$ is related to the interdiffusion or self-diffusion coefficient D as shown by Moelans *et al.* [32]. In general, the mobility is defined as,

$$M(c) = \frac{D}{\partial^2 f_0/\partial c^2} \ . \tag{2.6}$$

In a simplified framework, modeling the surface self-diffusion as the dominant mechanism can be achieved by considering the mobility function as a function of c as shown in Equation 2.4.

2.2 Numerical method

Different numerical strategies can be employed for phase-field modeling [34]. Here is a brief overview of different spatial discretization methods used in phase-field modeling: Finite difference method, Finite element method, Finite volume method, Fourier spectral method. Each method has its own strengths and weaknesses. In this study, the Fourier spectral method is used to solve the phase-field model considered. This method is fairly simple to implement

and offer a high spatial error convergence rate [33, 54, 55]. However, due to the mathematical properties of the Fourier transform, the method is limited to periodic boundary conditions and to the use of regular grids for spatial discretization. The periodic boundary conditions are both a useful byproduct of the use of spectral methods, for example when dealing with infinite systems, and a limitation depending when no-flux conditions need to be applied on certain boundaries of the domain. Thus, certain strategies are employed to overcome these limitations, especially the use of voxelization to represent any arbitrary shape in a regular grid.

2.2.1 Fourier spectral method

The solution to Equation 2.1 using the Fourier spectral method starts by taking the forward Fourier transform of both sides of the equation, which leads to

$$\frac{\partial \hat{c}}{\partial t} = \left\{ \nabla \cdot (M(c) \nabla \mu) \right\}_k \tag{2.7}$$

$$\implies \frac{\partial \hat{c}}{\partial t} = j\mathbf{k} \cdot \left\{ M(c) \left[j\mathbf{k} \cdot (w\widehat{g'}(c) + \kappa k^2 \hat{c}) \right]_r \right\}_k , \tag{2.8}$$

where $\hat{c}$ is the Fourier transform of c, $\{\cdot\}_k$ denotes the Forward Fourier transform of the expression inside the square brackets, $[\cdot]_r$ denotes the Inverse Fourier transform of the expression in the brackets, j is the pure imaginary number, $\mathbf{k}$ and k are the wave vector and the wave vector magnitude respectively.
Thus the problem simplifies to solving a system of ODEs in the Fourier reciprocal space.

2.2.2 Time marching scheme

A time marching scheme is now needed to solve the system of ODEs in the Fourier reciprocal space. The simplest method is the Forward Euler method which is a first-order accurate method, as described by the equation

$$\hat{c}^{n+1} = \hat{c}^n + \Delta t \, j\mathbf{k} \cdot \left\{ M(c) \left[j\mathbf{k} \cdot \left(w\widehat{g'}(c^n) + \kappa k^2 \hat{c}^n \right) \right]_r \right\}_k , \tag{2.9}$$

where Δt is the time step and n is the time step index. Unfortunately, the Forward Euler method is only conditionally stable and suffer from a severe time step constraint, which can be derived by performing a Von-Neumann analysis, as summarized as follows.

Von-Neumann analysis

A numerical method is said to be stable or convergent if the numerical domain of dependence contains the exact domain of dependence of the model [56]. The domain of dependence of the model is related to the speed of propagation of the solution. In the case of the Cahn-Hilliard equation, the speed of the solution is related to the mobility function $M(c)$. The model is most limited when the mobility function is at its maximum i.e. $\texttt{max}(M(c)) = M_0$. Indeed, the mobility function represents the numerical speed of the model. The mobility function is then

substituted by its maximum value M_0,

$$\begin{aligned}\hat{c}^{n+1} &= \hat{c}^n + \Delta t\, j\mathbf{k} \cdot \left\{ M_0 \left[j\mathbf{k} \cdot (\, w\widehat{g'(c^n)} + \kappa k^2 \hat{c}^n \,) \right]_r \right\}_k \\ &= \hat{c}^n - \Delta t M_0 k^2 \left(w\widehat{g'(c^n)} + \kappa k^2 \hat{c}^n \right) \ .\end{aligned}$$

Considering the most limiting factor, i.e. the fourth-order term, the derivative of the bulk free energy density in the Fourier reciprocal space is considered negligible. Thus, one writes,

$$\hat{c}^{n+1} = \left(1 - \Delta t M_0 \kappa k^4\right) \hat{c}^n$$

This finally leads to the amplification factor,

$$|\lambda| = |1 - \Delta t M_0 \kappa k^4| \leq 1 \implies \Delta t M_0 \kappa k^4 \leq 1 \ .$$

The development then leads to the following Courant Friedrich Lewy (CFL) condition, which poses the constraint on the time step,

$$\Delta t = \texttt{CFL} \frac{1}{M_0 \kappa k^4} = \texttt{CFL} \frac{dx^4}{M_0 \kappa} \ . \tag{2.10}$$

The constraint on the time step is indeed severe, as increasing the temporal resolution by a factor of ten would require a corresponding ten-thousand-fold increase in spatial resolution to maintain the stability of the explicit scheme.

Semi-implicit treatment

To circumvent this constraint, a semi-implicit treatment, inspired by Zhu *et al.* [12], can be performed by splitting the mobility into two parts, i.e. $M(c) \rightarrow (M(c) - \alpha)$ and α, respectively the explicit and implicit contribution, with α the stabilization factor. This leads to a semi-implicit treatment of the fourth-order term. The scheme is then written as,

$$\begin{aligned}\frac{\hat{c}^{n+1} - \hat{c}^n}{\Delta t} = j\mathbf{k} \cdot \Big\{ (M(c) - \alpha) \left[j\mathbf{k} \cdot \left(w\widehat{g'(c^n)} + \kappa k^2 \hat{c}^n \right) \right]_r \Big\}_k \\ + \alpha j\mathbf{k} \cdot \left[j\mathbf{k} \cdot \left(w\widehat{g'(c^n)} + \kappa k^2 \hat{c}^{n+1} \right) \right] \ .\end{aligned} \tag{2.11}$$

Expanding the above equation and isolating both $\hat{c}^{n+1}$ and $\hat{c}^n$ leads to the following semi-implicit Fourier Spectral scheme,

$$\hat{c}^{n+1} = \hat{c}^n + \frac{\Delta t\, j\mathbf{k} \cdot \left\{ M(c) \left[j\mathbf{k} \cdot \left(w\widehat{g'(c^n)} + \kappa k^2 \hat{c}^n \right) \right]_r \right\}_k}{1 + \alpha \Delta t \kappa k^4} \ . \tag{2.12}$$

Zhu *et al.* [12] showed that choosing $\alpha = \frac{1}{2}(\texttt{max}(M(c)) + \texttt{min}(M(c)))$ alleviates the time step constraint of the explicit scheme.

2.2.3 Diffuse filtering scheme

In addition to the semi-implicit treatment, a diffuse filtering scheme inspired by Sinhababu *et al.* [57] is employed to further stabilize the scheme. Indeed, the Fourier spectral method is known to suffer from the Gibbs phenomenon which leads to numerical oscillations near interfaces. Thus a dealiasing method is employed to filter out high frequency Fourier modes that could potentially lead to unwanted numerical oscillations [55, 58]. The diffuse filtering scheme filters out Fourier modes of frequency higher than $|k| \geq k_{\text{cutoff}} = \frac{\sqrt{2}}{3}\frac{2\pi}{d}$ with d the lowest grid spacing in the real space. Following the notation in [57], it is defined as follows,

$$\mathcal{W}(\mathbf{k}) = \frac{1}{2}\left[1 + \tanh\left(\frac{k_{\text{cutoff}} - \sqrt{k_x^2 + k_y^2 + k_z^2}}{\zeta}\right)\right] , \tag{2.13}$$

with $\zeta = 3 \times \texttt{max}(\Delta k_x, \Delta k_y, \Delta k_z)$, with Δk_i the grid spacing in the i direction in the Fourier reciprocal space.
The filtered Fourier transform of an arbitrary function now writes $\{f\}_k \rightarrow \hat{f} \cdot \mathcal{W}(\mathbf{k})$. The filtered reciprocal space is represented in Figure 2.3.

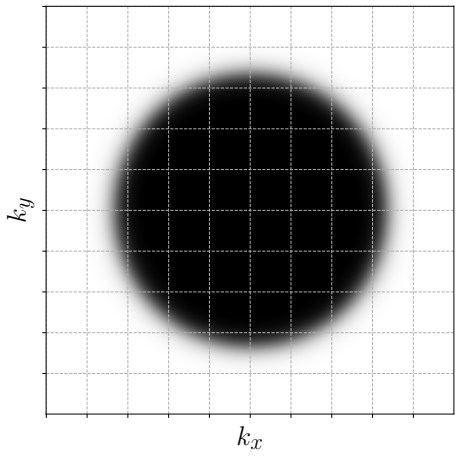

Figure 2.3. *Schematic of the filtered Fourier reciprocal space in 2D. The conserved Fourier modes are represented in the shaded area, from the lowest frequency, i.e. the origin of the Fourier reciprocal space, up to the limit $|k| = k_{cutoff}$. The rest of the reciprocal space is filtered out. Adapted from* [57].

2.2.4 Implementation

The numerical scheme implementation is detailed in Figure 2.4 and is inspired from [50]. The implementation is done in `Python3.8` using the `PyTorch` library [59]. `PyTorch` is a high-performance deep learning library which offers automatic differentiation and more importantly GPU acceleration which is crucial for solving phase-field problems since it requires a considerable amount of computation power [35]. The Fast Fourier Transforms (resp. Inverse Fast Fourier Transforms) are computed using `torch.fft.rfftn` (resp. `torch.fft.irfftn`) since the phase-field is real valued. In addition, the `gmsh` python library is used to generate

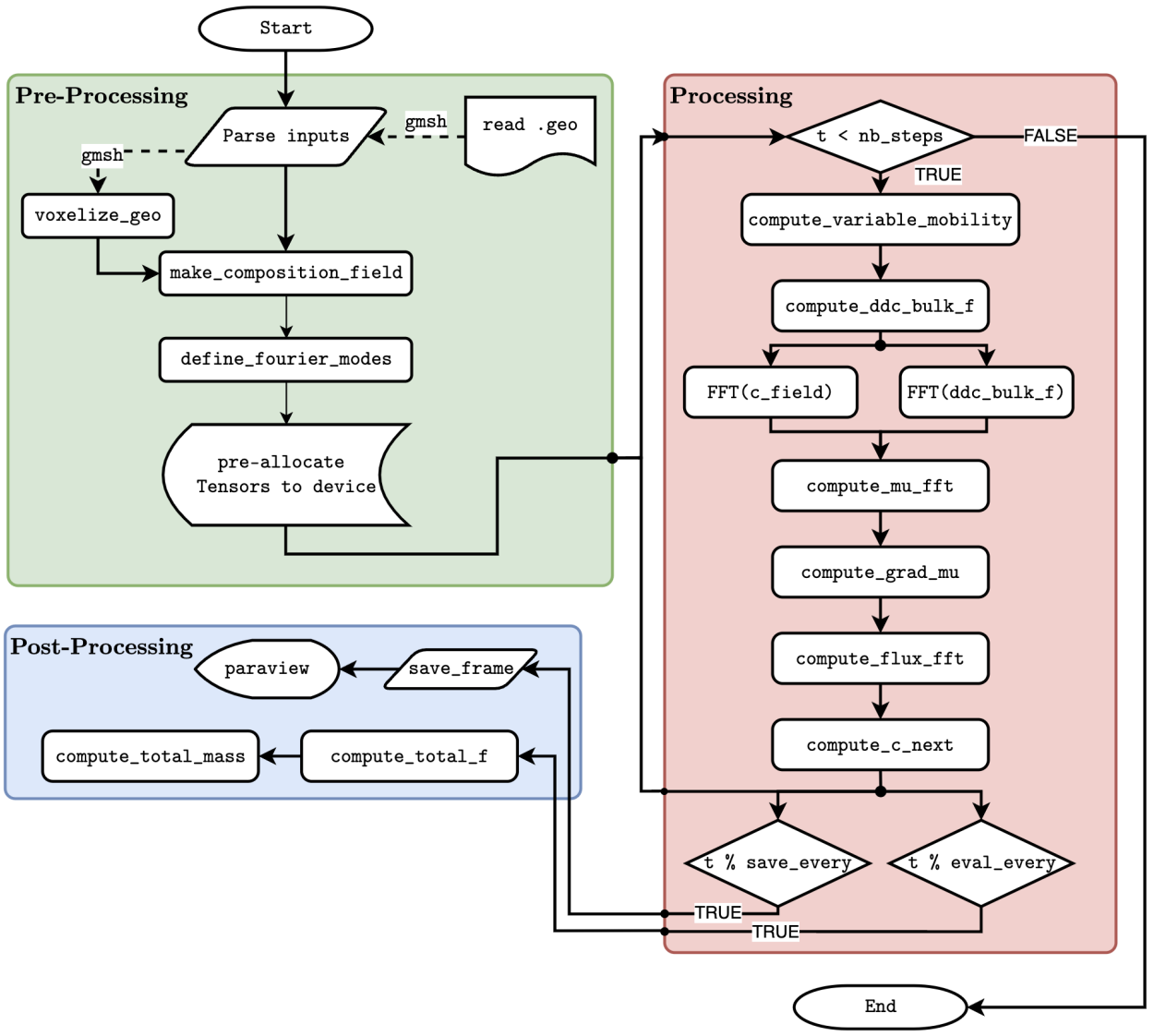

Figure 2.4. *Flowchart of the numerical scheme implementation. The numerical scheme is performed in three steps : Pre-Processing, Processing or the Time Marching Loop and the Post-Processing. The pre-processing consists in generating the composition field from either a prescribed function, a random field or a geometry generated using the* `gmsh` *software* [60]*. When the composition field is defined from a* `gmsh` *defined geometry, the geometry is voxelized, i.e. converted into a regular grid. Then, for optimization purposes, the tensors are pre-allocated on both the CPU and the GPU. The Processing or the Time Marching Loop implements the semi-implicit scheme defined in Equation 2.12. At each step, the variable mobility $M(c)$, is first computed in the real space as well as the derivative of the bulk free energy f_0, referred to as g. The Fourier Transform of the composition field c and of g are then computed. The chemical potential in the Fourier reciprocal space as well as its gradient in real space are computed, which leads, in juxtaposition with the previously computed mobility, to the composition flux* $\mathbf{J}$*. With every factor computed from Equation 2.12, the composition field at the next time step can be evaluated. The Post-Processing consists in either saving the results in binary* `.vtk` *files for later visualization in* `Paraview` [61] *or in* `.pt` *files for later analysis.*

geometries, i.e. the initial configuration of the phase-field which are then voxelize to fit the required regular grid. The details on voxelization are provided in Section 2.4. Finally, the visualisation is performed using `Paraview` [61].
Numerical experiments on the implemented model were performed on a `MacBook Pro 16" M1 Max` with 64 GB of RAM.

2.3 Numerical experiments

2.3.1 Benchmark problem

With the growing interest in the domain of phase-field modeling, Jokisaari *et al.* [38] put together a series of benchmark problems to assess the accuracy and efficiency of newly implemented phase-field solvers. The considered benchmark problem is the spinodal decomposition of a binary mixture which is a standard problem in phase-field modeling. Spinodal decomposition might be one of the simplest problem to model, but it is also highly relevant as the simulated physical phenomena are the basics of more challenging problems such as nanowire morphological instability.

Problem 1 statement

The free energy of the system is defined in Equation 2.3 using the quartic polynomial approximation of the bulk free energy density f_0,

$$f_0(c) = w(c - c_\alpha)^2(c - c_\beta)^2 \ , \tag{2.14}$$

with c_α and c_β the equilibrium composition in the bulk of the binary mixture α–β.
The mobility is considered constant and uniform across the domain. Finally, the considered model parameters from the benchmark [38] are the following,

$$w = 5 \ , \ \kappa = 2 \ , \ M = 5 \ , \ c_\alpha = 0.3 \ , \ c_\beta = 0.7 \ , \ c_0 = 0.5 \quad \text{and} \quad \epsilon = 0.01 \ . \tag{2.15}$$

The computational domain is defined as a square box of non-dimensional side length $L = 200\,(-)$ with periodic boundary conditions on all sides. The characteristic length is of the order of the diffuse interface width δ.
The initial condition is shown in Figure 2.5 and defined as,

$$\begin{aligned} c(x, y, 0) = c_0 + \epsilon[&\cos(0.105x)\cos(0.11y) + [\cos(0.13x)\cos(0.087x)]^2 \\ &+ \cos(0.025x - 0.15y)\cos(0.07x - 0.02y)] \ , \end{aligned} \tag{2.16}$$

where c_0 represents the average value of the composition across the domain and ϵ represents the amplitude of the perturbation. When studying spinodal decomposition, the initial condition is typically generated using a pseudo-random generator to simulate a random intitial state. However, for reproducibility purposes, Jokisaari *et al.* proposed the above definition to *'provide smoothly varying, relatively disordered field that are implementation-independent'* [38].

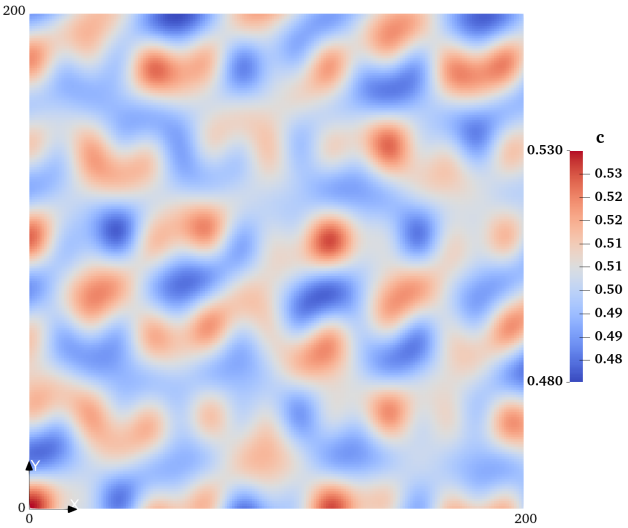

Figure 2.5. *Computational domain and initial condition of the benchmark problem. The initial condition is chosen as a superposition of cosine functions to mimic a random initial condition for reproducibility purposes.*

Problem 2 statement

In addition to this benchmark problem, the implemented model is compared to the results of Zhu *et al.* [12] which studied coarsening kinetics, using a variable mobility Cahn-Hilliard equation. Snapshots of the microstructural evolution are compared to the one presented in [12].
The computational domain is defined as a square box of side length $L = 1024\,(-)$ with periodic boundary conditions on all sides. The initial condition is defined as follows,

$$c(x, y, 0) = c_0 + \epsilon\,[0.5 - \texttt{RAND()}] \tag{2.17}$$

with c_0 the average or critical composition of the binary mixture and `RAND()` a random number generator ($X \sim \mathcal{U}(0, 1)$).
Zhu *et al.* relied on Langer [13] mobility function, $M(c) = |1-c^2|$ and a scaled order parameter $c \in [-1, 1]$ whereas the implemented model defines the order parameter as $c \in [0, 1]$. However, the goal is to compare the microstructural evolution under surface-driven phase separation conditions and not exact quantitative comparison.

2.3.2 Consistency and stability assessment

The phase-field model now implemented, the next step consists in checking the consistency and stability of the model. The consistency is ensured if the numerical solution converges to the real solution as the regular mesh is refined. As for the stability, using the CFL condition previously established in Equation 2.10, one can empirically assess whether further temporal refinement is needed.
The total free energy of the system is used as a metric to assess both the consistency and stability of the model as it is an integral quantity which is best suited for this purpose. It is compared to the one reported by Jokisaari *et al.* [38] for the benchmark problem.

Mesh refinement

Figure 2.6 shows the effect of the mesh size on the total free energy with respect to time.

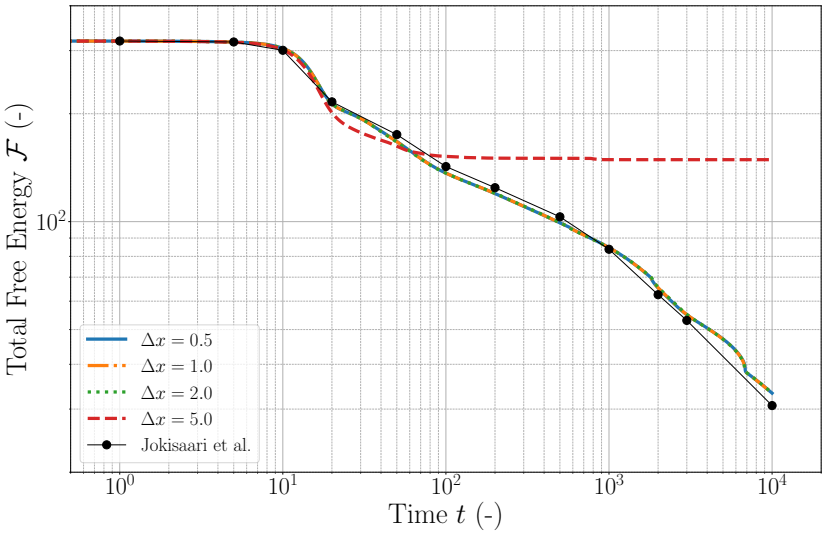

Figure 2.6. *Total free energy with respect to time for different Δx with a fixed time step $\Delta t = 0.5$. When the mesh size is sufficiently refined, the total free energy converges and the solution is consistent.*

One can see that as the mesh is refined, the total free energy converges to the one reported by Jokisaari *et al.* [38]. The slight discrepancies are mainly due to time marching scheme and the spatial discretization used in the implemented model. Jokisaari *et al.* used a time adaptive scheme as well as an adaptive mesh refinement. But for the purpose of this work, a fixed time step and uniform regular grid provide sufficient accuracy.
The Mean Square Error MSE is also computed over the simulated time and is reported in the following table.

Δx	MSE
5.0	56.4207
2.0	3.81102
1.0	3.75193
0.5	3.74367

Table 2.1. *Mean square error of the total free energy with respect to the mesh refinement.*

As the mesh becomes finer, the mean square error decreases less and less. In addition, for coarse meshes, the total free energy highly deviates from the expected trend. This is mainly due to the poor resolution of the interface. Indeed, to correctly capture the phase separation, the spatial discretization must be fine enough to resolve the interface between the two phases.

Stability assessment

The effect of temporal refinement at constant spatial discretization of the total free energy with respect to time is shown in Figure 2.7 which highlights that a good choice of the time step Δt must be in order.

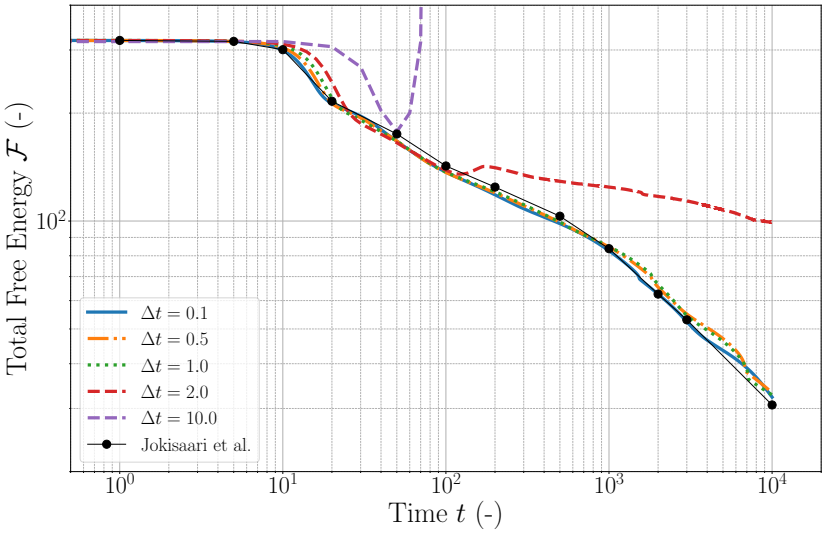

Figure 2.7. *Total free energy with respect to time for different values of Δt with a fixed mesh size $\Delta x = 1.0$. The scheme is unstable for $\Delta t \gtrsim 2.0$ as it ultimately results to a sudden increase in the total free energy at $t \approx 2 \times 10^2$ which is not physical since the total free energy is a strictly decreasing function of time* [11, 32, 37].

One can see that the scheme is unstable for $\Delta t \approx 2.0$ and the total free energy is subject to a sudden increase which is not physical. In addition, one can see that further temporal refinement does not significantly lead to a better precision of the solution and comes with a large computational cost. Thus, the time step is chosen as the 'largest' Δt that leads to a stricly decreasing total free energy.

2.3.3 Validation

The consistency and stability of the model now established, the model can be validated against another benchmark problem, i.e. Zhu *et al.* coarsening kinetics problem. Since the authors only provided snapshots of the microstructural evolution, the evolution of the total free energy is not reported. In addition, error maps are not reported since the initial condition relies on a random number generator. Thus, only the microstructural evolution behavior is assessed which is crucial in assessing the choice of the mobility function to model surface-driven phase separation. The simulation parameters are the following,

$$w = 1 \ , \ \kappa = 1 \ , \ M_0 = 0.5 \ , \ \alpha = 0.25 \ , \ \Delta x = 1.0 \quad \text{and} \quad \Delta t = 1.0 \ . \tag{2.18}$$

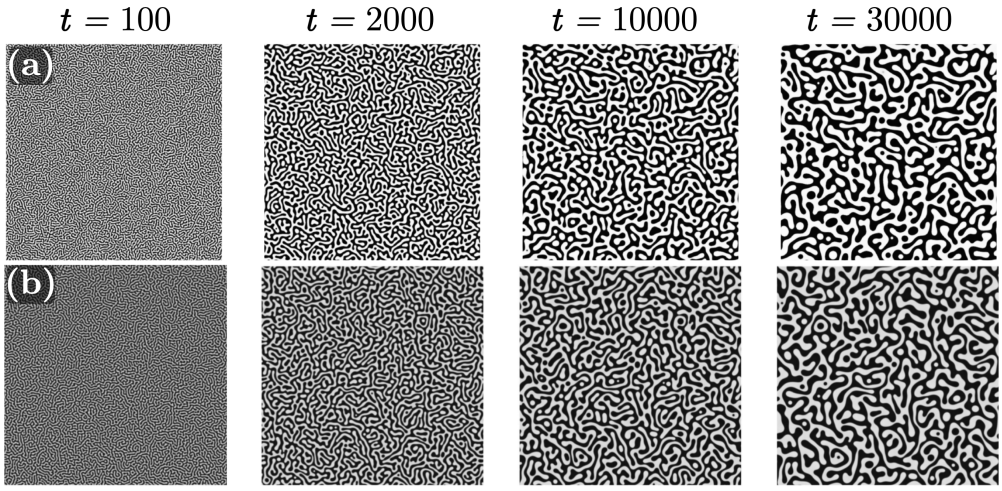

Figure 2.8. *Snapshots of the microstructural evolution of the coarsening kinetics problem.* (a) *implemented model,* (b) *Zhu et al.* [12].

In Figure 2.8, the time evolution of surface-driven phase separation captured by the implemented model is highlighted. The microstructural evolution behavior is consistent with the one reported in Zhu *et al.* [12]. Indeed, the coarsening kinetics predicted by the implemented model correctly captured the growth of the characteristic size of the grains at similar time scales. In addition, the resulting microstructure is consistent with the surface-driven specific microstructure reported in Zhu *et al.* [12].

2.4 Nanowire morphological instability

In this section, the implemented model is used to reproduce a selection of results presented in Roy *et al.* [14] which studied surface-enhanced breakups in free-standing nanowires.

2.4.1 Free standing nanowire model

The nanowire is approximated as a free-standing infinitely long cylinder of radius R. The physical domain is shown in Figure 2.9. In addition, two configurations are considered: a single straight wire of radius R, and a junction comprising two wires with radii R_1 and R_2 corresponding to the primary and secondary wires, respectively, intersecting at an angle θ, i.e. a relative orientation of θ. The geometry of the problem is constructed using the `gmsh` software [60].
The order parameter c in the phase-field model is defined as an indicator of whether a point belongs to the nanowire, the interface or the vacuum,

$$c(\mathbf{x},t) = \begin{cases} 1 & \text{if } \mathbf{x} \text{ in NW bulk (film)}, \\ 0.5 & \text{if } \mathbf{x} \text{ on the interface}, \\ 0 & \text{if } \mathbf{x} \text{ in vacuum bulk (vapor)}. \end{cases} \tag{2.19}$$

The contribution from the thermal annealing is modeled by adding a small stochastic perturbation to the order parameter c in the initial condition [62]:

$$c(\mathbf{x}, 0) = \texttt{make\_composition\_field()} + \epsilon\, \tilde{c}(\mathbf{x}) \ , \tag{2.20}$$

with `make_composition_field()` the function which performs the voxelisation algorithm of the prescribed geometry, ϵ the amplitude of the stochastic perturbation and $\tilde{c}(\mathbf{x}) \sim \mathcal{U}(-1, 1)$ the stochastic contribution modeling the perturbation.
The Cahn-Hilliard equation solves the dynamics of a conserved order parameter c. Thus, using this description, mass conservation is ensured as recalled in Section 1.3. In addition, the total free energy is minimized when the system reaches equilibrium. The dynamics implemented being surface-driven by design of $M(c)$, the minimization of the total free energy leads to the minimization of the surface energy of the rods.

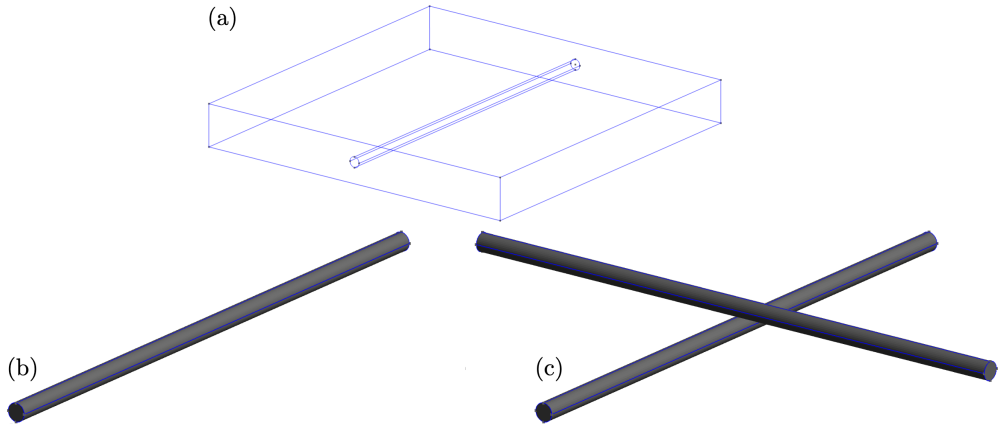

Figure 2.9. *Geometry of the* (a) *physical domain* (b) *single wire configuration* (c) *junction with* $\theta = \pi/2$. *The wire on the bottom (resp. top) is referred to as the primary (resp. secondary) wire. Visualization was performed in* `gmsh`.

2.4.2 Voxelisation

As previously mentioned in Section 2.2, the physical domain must be discretized as a regular grid. However, the geometry of the problem can be non-trivial and can thus lead to challenges in the discretisation. A discrete approximation of a digital object is referred to as a voxelisation [63]. Two approaches to voxelisation are presented and discussed in the following.

Binary voxelisation

This approach is performed by first defining a coarse unregular mesh in `gmsh` and then performing an octree search to find elements which are inside the prescribed volume of the nanowire. The voxelised nanowire is shown in Figure 2.10.

Figure 2.10. *Binary Voxelisation of the single nanowire geometry.* (a) *Side view* (b) *Cross-section of the voxelised geometry compared to the actual geometry (dark grey). Visualization performed in* `Paraview`.

This approach benefits from `gmsh` built-in CAD engine, which allows to define the geometry with ease. The octree search, performed using the `gmsh` API, efficiently identifies elements within the prescribed volume of the nanowire. However, for more complex geometries, this method may result in mislabeled grid points due to the coarse mesh, potentially introducing numerical errors. In addition, this approach results in a sharp interface representation of the geometry, which is not consistent with the principles of the phase-field formalism, i.e. the use of a diffuse-interface to smoothly transition between phases. Nevertheless, for the purpose of validating the model and the implementation, this approach is utilized to reproduce the results presented in Roy *et al.* [14], as their study assumes an initial condition with a sharp interface.
Methods such as anti-aliasing [63], which purpose is to smooth interfaces, can be used to recover a diffuse interface approach. However, instead of relying on the initial binary voxelisation, a more consistent approach, non-binary voxelisation, is presented in the following section.

Non-binary voxelisation

This approach is based on the equilibrium composition profile of the Cahn-Hilliard equation. The order parameter describing the composition c is given by,

$$c(x) = \frac{1}{2}\left[1 - \tanh\left(\frac{x - x_0}{\delta}\right)\right], \tag{2.21}$$

with $\delta = \sqrt{\frac{2\kappa}{w}}$ the characteristic length of the diffuse interface, x_0 the position of the interface. The equilibrium profile is shown in Figure 1.8. Essentially, the function acts as a mask which smoothly transitions from one phase to the other. More generally, the order parameter c can be defined in 3D as,

$$c(\mathbf{x}) = \frac{1}{2}\left[1 - \tanh\left(\frac{d(\mathbf{x})}{\delta}\right)\right], \tag{2.22}$$

with $d(\mathbf{x})$ the signed-distance of each point $\mathbf{x}$ in the domain Ω from the nominal surface of the desired geometry [64].

The signed-distance function $d(\mathbf{x})$ is defined as the distance from the surface of the geometry, with a sign indicating whether the point is inside or outside the geometry, i.e.

$$d(\mathbf{x}) = \begin{cases} -\text{dist}(\mathbf{x}, \partial\Omega_c), & \mathbf{x} \in \Omega_c, \\ 0, & \mathbf{x} \in \partial\Omega_c, \\ +\text{dist}(\mathbf{x}, \partial\Omega_c), & \mathbf{x} \notin \Omega_c, \end{cases} \tag{2.23}$$

with $\partial\Omega_c$ the nominal surface of the geometry and $\text{dist}(\mathbf{x}, \partial\Omega) = \min_{\mathbf{x}_n \in \partial\Omega} ||\mathbf{x} - \mathbf{x_n}||$ the Euclidean distance from the point $\mathbf{x}$ to the surface $\partial\Omega$. The signed-distance function is illustrated in Figure 2.11.

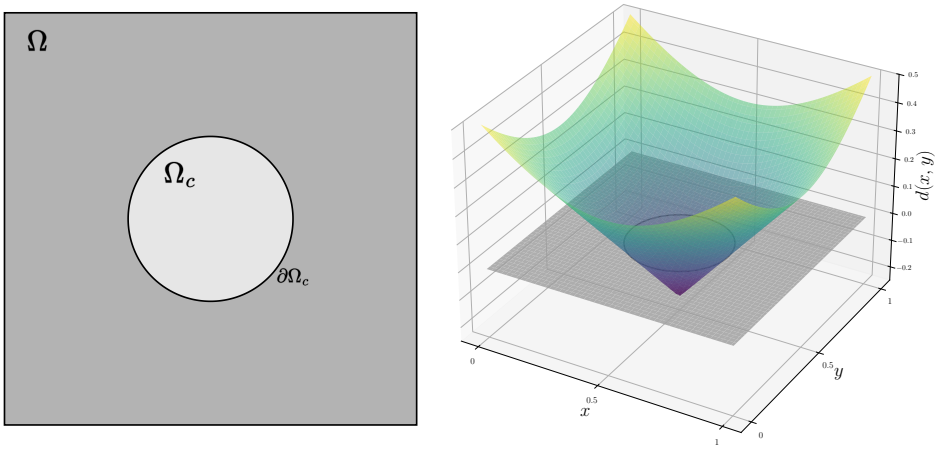

(a) (b)

Figure 2.11. (a) *Physical domain* Ω*, the prescribed geometry* Ω_c *and the nominal surface* $\partial\Omega_c$*.* (b) *The signed-distance function* $d(\mathbf{x})$*. The function is negative inside the* Ω_c *and positive outside.*

A signed-distance function $d(\mathbf{x})$ can then be defined for the desired geometry of the problem. Thus, the geometry can be voxelised by defining an appropriate signed-distance function $d(\mathbf{x})$ and by discretising the physical domain with a regular grid. The voxelised nanowire is shown in Figure 2.12 and a side-by-side comparison with the binary voxelisation of an x-y slice is shown in Figure 2.13.

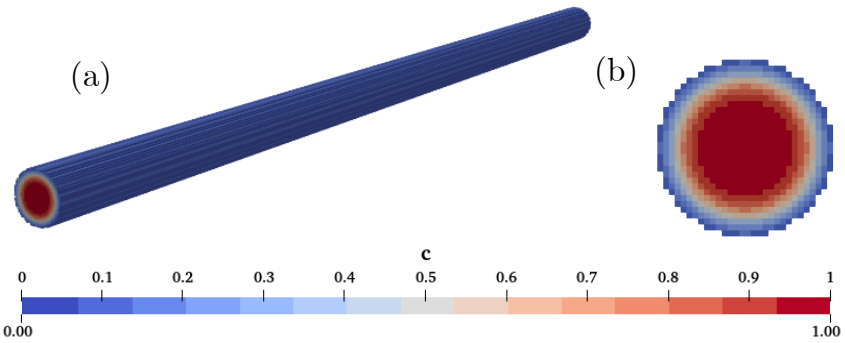

Figure 2.12. *Non-Binary Voxelisation of the single nanowire geometry.* (a) *Side view* (b) *Cross-section of the voxelised geometry. The actual geometry coincides with* $c = 0.5$. *Visualization performed in* `Paraview`.

This approach is more flexible and offers a better control over the effect of the stochastic noise. In addition, the resulting voxelised geometry is better aligned with the phase-field formalism as the interface is not sharp and defined in accordance to the model parameters. However, the signed-distance function $d(\mathbf{x})$ must be defined for each geometry and can be challenging for non-trivial geometries.

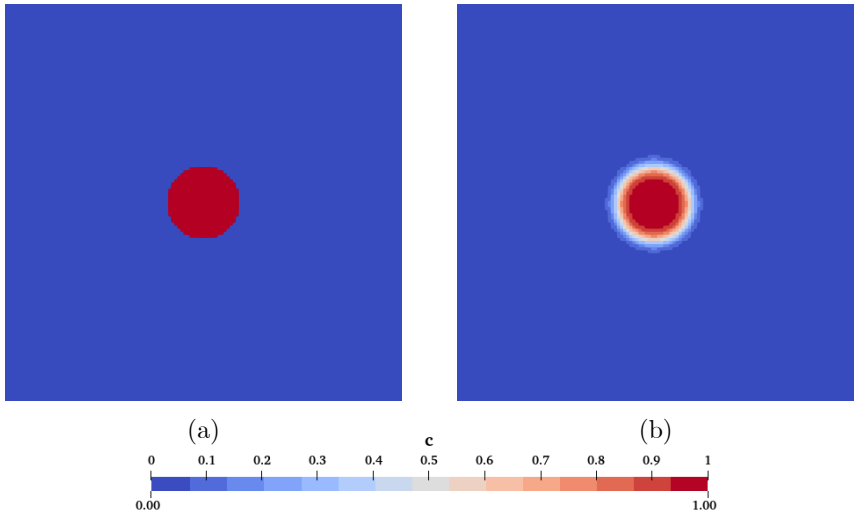

Figure 2.13. *Image of an x-y slice view of the initial condition in the* (a) *binary* (b) *non-binary voxelisation approach. As stated, the non-binary voxelisation provide a smooth transition from one phase to the other. Visualization was performed in* `Paraview`.

2.4.3 Results and comparison

Prior to the presentation of the results of the study, the implemented method is compared to the results presented in Roy *et al.* [14]. This verification was performed on both, the single wire and the junction, configurations relying on a binary voxelisation for reproduction purposes. The simulation parameters used for this battery of tests are presented in Table 2.2.

For the sake of clarity, the non-dimensionalisation steps of the parameters are detailed in Chapter 3.

Parameter	Value
R_1	6.0
R_2	6.0
κ	1.0
w	1.0
M_0	0.5
α	0.5
ϵ	10^{-3}
Δx	0.5
Δt	1.0

Table 2.2. *Non-dimensional simulation parameters used by Roy et al.* [14].

Single wire

The breakups of both infinitely long and finite single free-standing nanowires are respectively shown in Figure 2.14. The results of the breakup are in good agreement with Roy's.

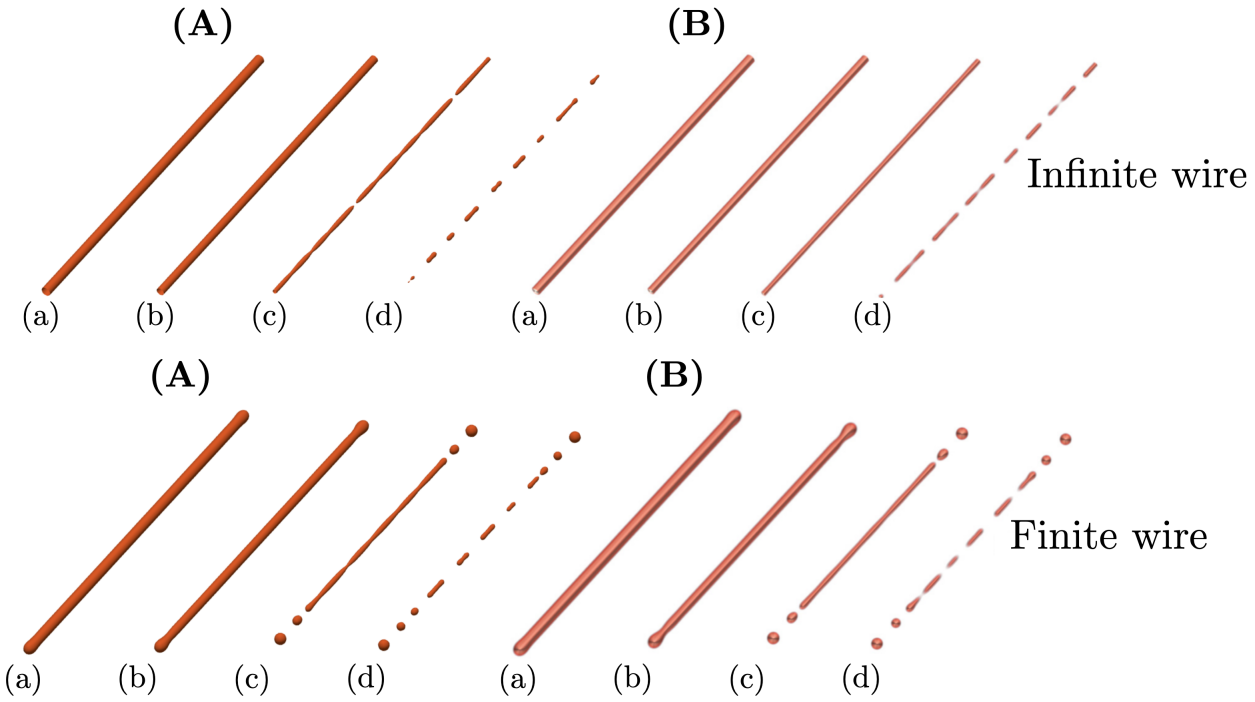

Figure 2.14. *Single free-standing nanowire simulation from* (A) *the implemented model* (B) *Roy et al. at* (a) $t = 500$ (b) $t = 1500$ (c) $t = 2700$ (d) $t = 2800$. *The simulation results represent the contour plot of the composition field* ($c = 0.5$) [14].

Indeed, the free ends of the finite nanowire retract and bulge out. As the ends retracts, necking starts to form which then lead to the breakup of the nanowire into a series of spherical chunks. In addition, the spherical chunks are not of the same size, due to the coarsening of the wire. In the case of the infinitely long nanowire, the wire starts by coarsening until the instabilities grow sufficiently to induce necking and subsequent breakup of the nanowire. The fragmentation in a series of spherical chunks observed in both simulations is in good agreement with the literature recalled in Chapter 1. Nichols and Mullins predicted that free-standing rods breakup into a series of chunks due to the surface energy minimization. The fragmentation is mediated by the maximally growing wavelength λ of the inital perturbation.

Junction

The breakups in the junction configuration are presented in Figure 2.15. The observed evolution in good agreement with the results obtained in [14]. The proximity between the two nanowires leads to local sintering. In addition, necking occurs at the location of the junction on each nanowire as shown in Figure 2.16. As the wires coarsen and the instabilities grow, further necking is observed at the junction which lead to the breakup of the junction, leaving behind a spherical chunk. Afterwards, the free ends of the broken junction retracts and bulge out, leading to the formation of spherical chunks. This highlights two distinct mechanisms, the initial breakup of the junction into a central chunk and the subsequent breakup of the free ends. The free ends breakup is similar to the one observed in the single wire configuration.

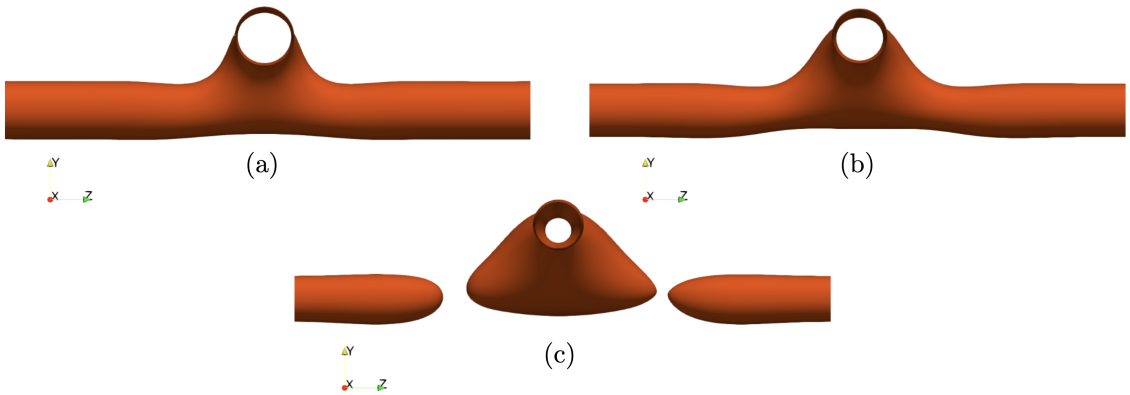

Figure 2.16. *Zoom view of the junction of the two nanowires at* (a) $t = 500$ (b) $t = 1000$ (c) $t = 1750$ *from the implemented model. The junction simultaneously undergoes necking and coarsening.*

The implemented model is thus able to reproduce the results presented in Roy *et al.* [14]. In the following chapter, the study performed by Roy *et al.* is extended by first discussing the influence of the non-dimensionalisition of the parameters on the dynamics. Then, thanks to the implemented voxelisation algorithm, the influence of the initial shape of the nanowire is studied.

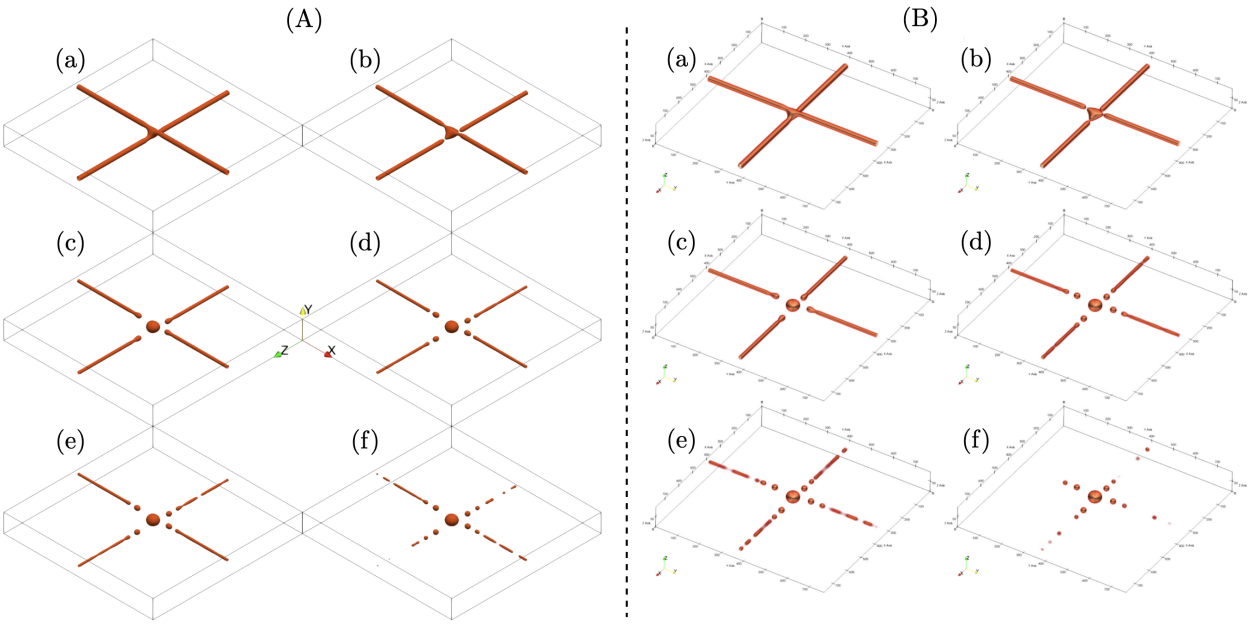

Figure 2.15. *Simulation* (A) *from the implemented model* (B) *Roy et al. of the morphological evolution of two intersecting nanowires* ($\theta = 90°$) *at* (a) $t = 1000$ (b) $t = 1750$ (c) $t = 2500$ (d) $t = 2750$ (e) $t = 2800$ (f) $t = 2900$. [14]. *The slight differences between frames* (e) *and* (f) *are due to the stochastic nature of the initial condition.*

Chapter 3

Free-standing nanowire

This chapter investigates the dynamics of morphological instability by extending the results on the free-standing nanowire configuration. First, a non-dimensional analysis is performed on the model equation to shed light on the influence of the different characteristic physical parameters on the parameters of interest i.e. the breakup time t_b and the wavelength of the instability λ. Extending on the work of Roy *et al.* [14], two configurations are considered: a single free-standing nanowire and a junction made from two free-standing nanowires. Finally, a discussion on the geometrical consideration is performed. The influence of the nanowire initial shape is presented to bridge between the numerical approximation and the experimental observations.

3.1 Non-dimensional analysis

Dimensionless equations are such that relationships between the physical parameters hold true no matter the scale of the system [65]. In addition, Buckingham–π theorem provides a tool to identify the number of dimensionless independent quantities that affects a dimensionless dependent quantity, i.e.

$$\Pi_0 = f(\Pi_1, \Pi_2, \ldots, \Pi_{n-k}) \tag{3.1}$$

with n the number of independent quantities and k the number of dimensionally independent quantities.
In this context, the Cahn-Hilliard equation can be non-dimensionalized by considering the following characteristic quantities [65, 66],

$$x = L^* x' \quad \text{and} \quad t = T^* t' \tag{3.2}$$

where L^* and T^* are respectively the length and time characteristic quantities.
Following this definition and considering the order parameter c to be non-dimensional as

recalled in Section 2.4, Equation 2.1 can be rewritten as,

$$\begin{aligned}
\frac{1}{T^*}\frac{\partial c}{\partial t'} &= \frac{1}{L^*}\nabla' \cdot \left[M(c)\frac{1}{L^*}\nabla' \left(wg'(c) - \frac{\kappa}{(L^*)^2}\Delta' c \right) \right] \\
\frac{\partial c}{\partial t'} &= \nabla' \cdot \left[M_0 w \frac{T^* E^*}{(L^*)^5} m(c) \nabla' \left(g'(c) - \kappa \frac{L^*}{w}\Delta' c \right) \right] \\
\implies \frac{\partial c}{\partial t'} &= \nabla' \cdot \left[\tilde{M}(c) \nabla' \left(g'(c) - \tilde{\kappa}\Delta' c \right) \right]
\end{aligned} \tag{3.3}$$

with the scaled non-dimensional mobility $\tilde{M}$ and the scaled non-dimensional gradient energy $\tilde{\kappa}$ given by,

$$\tilde{M}(c) = M_0 w \frac{T^*}{(L^*)^2} m(c) \quad \text{and} \quad \tilde{\kappa} = \frac{\kappa}{w}\frac{1}{(L^*)^2} \ , \tag{3.4}$$

where $m(c)$ is the normalised mobility function defined in Equation 2.4.
In addition, a characteristic energy E^* can be defined [66]. Following this non-dimensionalisation, the defined characteristic quantities can be expressed in terms of the physical parameters of the Cahn-Hilliard equation as

$$L^* \approx \sqrt{\frac{\kappa}{w}} \quad , \quad T^* \approx \frac{\kappa}{w^2 M_0} \quad \text{and} \quad E^* \approx \sqrt{\frac{\kappa^3}{w}} \ . \tag{3.5}$$

The characteristic length L^* is proportional to the characteristic length of the diffuse interface δ_c and is taken such that $L^* = 1$ unit length corresponding to a diffuse interface thickness $(0.05 < c < 0.95)$ of $\xi_c = 2.944\,\delta_c$ [38].
The general organization of the results is initially inspired by the approach used by Mao *et al.* [66] as their work provides a comprehensive framework for non-dimensional analysis of phase-field models. The goal is to carry out phase-field simulations of the morphological instability that nanowires, in different configurations, undergo. The two quantities of interest are the breakup time t_b, i.e. the time of appearance of the first morphological failure, and the wavelength of the instability λ, i.e. the spacing between each resulting nanodot. The quantities are recorded for different combinations of the characteristic quantities and of the geometrical parameters, yielding

$$t_b = f(\ldots; L^*, T^*, E^*) \quad \text{and} \quad \lambda = g(\ldots; L^*, T^*, E^*) \ , \tag{3.6}$$

the functional dependencies of quantities of interest. The wavelength λ is defined as the distance between two consecutive nanodots along the wire-axis and the breakup time t_b as the time at which the first pinch-off occurs, i.e. the onset of ovulation. To quantitatively determine the latter, a dimensionless parameter, the driving force Γ, is defined as,

$$\Gamma(t) = \frac{\Delta\mu(t)}{\Delta\mu(0)} \tag{3.7}$$

where $\Delta\mu$ is the difference between the highest and lowest value of the chemical potential at time t and $t = 0$ is the initial time of the simulation.
This indicator is inspired by the approach that Amos *et al.* [67] utilised to quantify the

spheroidization dynamics of finite length metallic rods under volume-driven diffusion. An example of the driving force Γ during the transformation of a finite length nanowire is given in Figure 3.1.

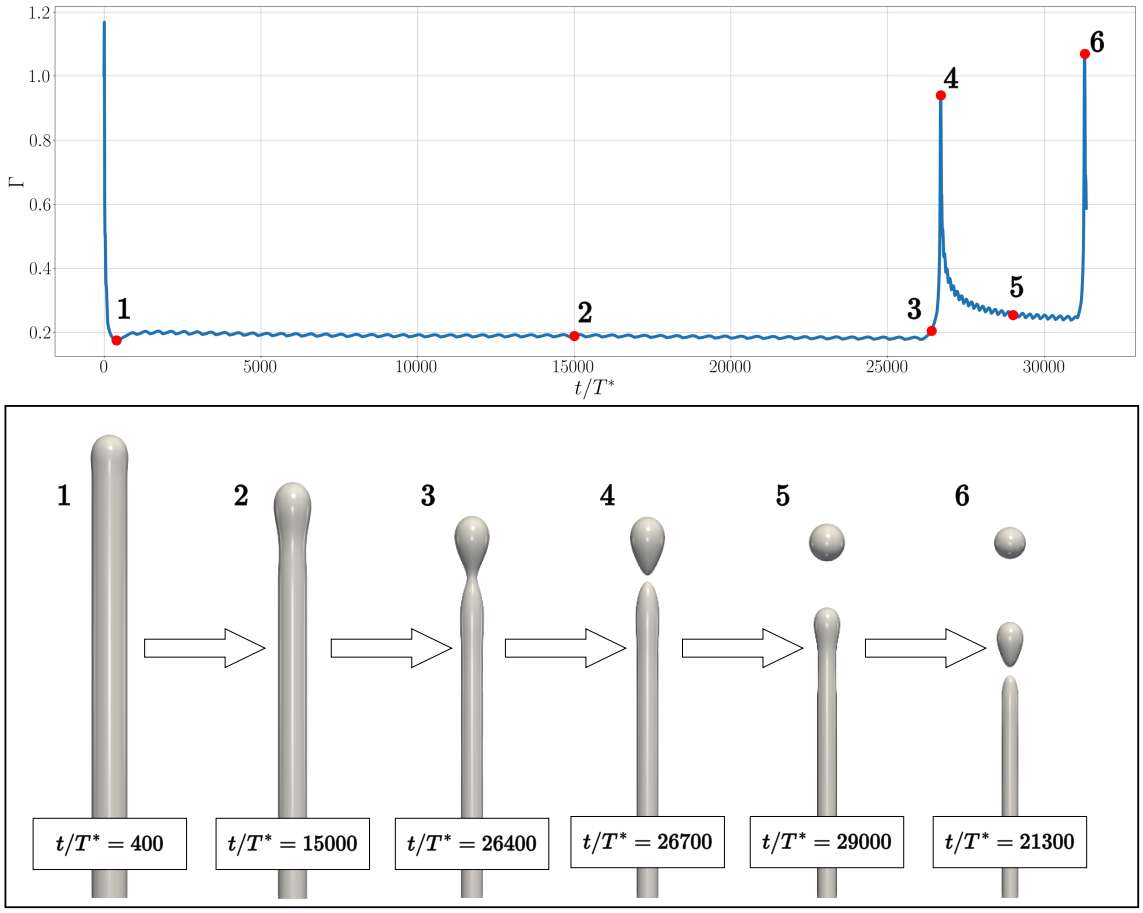

Figure 3.1. *Example of the driving force Γ with respect to time for a finite nanowire of length $L/L^* = 150$ and radius $R/L^* = 3$ with $T^* = 0.1$ and $E^* = 1$. The top figure represents the evolution of the driving force Γ at different dimensionless times t/T^*. The bottom figure shows contour plot ($c = 0.5$) snapshots from the morphological evolution of the nanowire. The breakup time t_b is defined as the time at which the driving force Γ reaches a steep increase (point 4) which matches with the pinch-off of the nanowire.*

The breakup time t_b is then defined as the time at which a steep increase of the driving force Γ occurs. In addition, the spatial (resp. time) refinement factor ρ (resp. ω) is defined as the ratio between the characteristic length L^* (resp. characteristic time T^*) and the mesh size Δx (resp. the time step Δt).
The goal is to provide a framework to better understand the instability mechanism and to shed light on possible ways to control the onset of instability, which would be relevant in the optimization of nanowire-based devices.

3.2 Geometrical considerations

Polyol-grown Silver nanowires are known for their distinct polycrystalline structure, which leads to a regular pentagonal cross-section. This morphology arises from their synthesis (polyol process), which starts from a multiply twinned nanoparticle seed (MTP) that grows through Ostwald ripening with the assistance of PVP [5, 21]. The cross-section and a schematic illustration of the polyol process from a MTP to a pentagonal nanowire are shown in Figure 3.2.

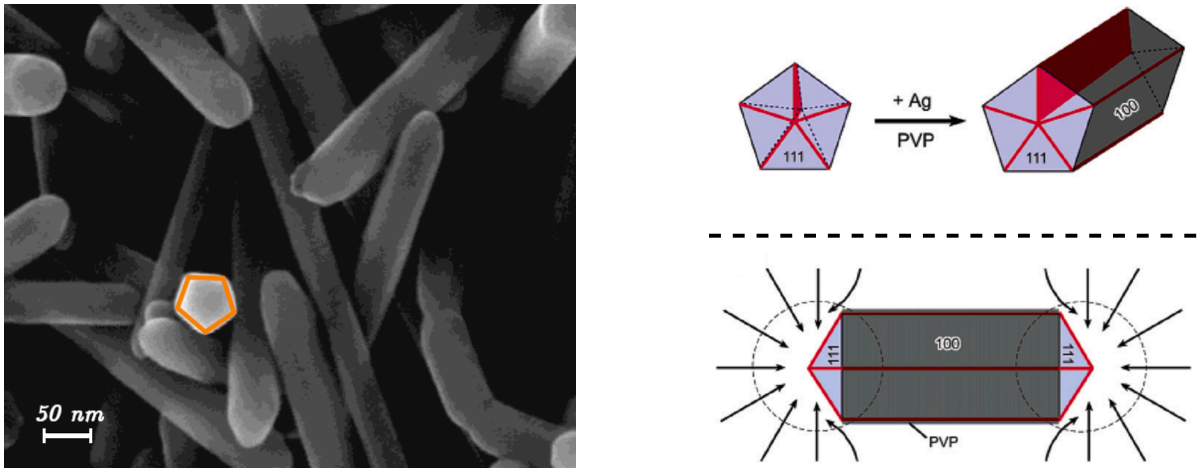

(a) (b)

Figure 3.2. (a) *Scanning electron microscopy (SEM) image of a polyol-grown Silver nanowire showing a pentagonal cross-section, highlighted in orange.* (b) *Schematic of a Silver MTP before and after the polyol process. Adapted from* [5].

As a result, the surface energy of the nanowire is anisotropic since each facet has different packing densities, i.e. the number of atoms per face per unit surface, leading to different surface energies. More packing means that, on the facet, the atoms are more closely packed, leading to a lower surface energy and increased stability. In the case of pentagonal silver nanowires, the (100) facets are the lesser stable facet compared to (111) facets [68–70].

In the context of the phase-field model, anisotropic surface energy can be treated by different approaches, such as anisotropic Cahn-Hilliard and Allen-Cahn coupling (to treat each crystal as an independent non-conserved order parameter), or by using a single conserved order parameter with anisotropic surface energy.

However in this work, anisotropic surface energy are neglected in favor of a simplified isotropic surface energy model as first discussed in Section 2.4. This simplification is motivated by the fact that anisotropic surface energy treatment, and polycrystalline consideration, require a more complex and more computationally expensive implementation of the presented phase-field model [14, 42, 47, 71–74]. Nevertheless, the relevance of crystalline effects on the morphological instability of nanowires is investigated by considering a faceted rod with a pentagonal cross-section.

As recalled in Section 2.4, the surface energy minimization is the driving force in the presented model. In this context, the geometry of the pentagonal cross-section is chosen such that the outer surface area matches the outer surface area of the cylindrical approximation of the nanowire. The side length s of the pentagonal cross-section is defined as such,

$$5s = 2\pi R \implies s = \frac{2}{5}\pi R \ . \tag{3.8}$$

The associated circumradius R_p can then be expressed as,

$$R_p = \frac{\pi}{5\sin\left(\frac{\pi}{5}\right)} R \ . \tag{3.9}$$

This condition ensures that both outer surface areas are equal, provided sufficient mesh refinement. The initial total free energy of the pentagonal cross-section is compared to the circular cross-section for different refinement factor ρ in Table 3.1 and the voxelised pentagonal nanowire is shown in Figure 3.3. As expected, the total free energy difference decreases when the mesh is more refined, i.e. when the refinement factor ρ increases. The condition is thus satisfied starting from $\Delta x = 0.5$.

ρ	$\mathcal{F}_p$	$\mathcal{F}_c$	$\Delta\mathcal{F}$
2.0	1200.14	1223.78	23.64
4.0	1227.18	1232.16	4.98
8.0	1229.8	1232.22	2.42

Table 3.1. *Total free energy (non-dimensional) of the pentagonal cross-section $\mathcal{F}_p$ and the circular $\mathcal{F}_c$ for different mesh sizes Δx. The difference $\Delta\mathcal{F}$ is also provided as a means of comparison. The total free energy is given in unit radius R/L^*.*

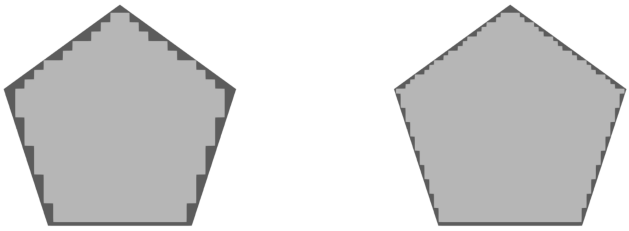

(a) (b)

Figure 3.3. *Voxelisation of the pentagonal cross-section nanowire with* (a) $\rho = 4$ (b) $\rho = 2$.

3.3 Initial perturbation assessment

As mentioned in Section 2.4, the effect of the thermal annealing is modeled by adding a small stochastic perturbation to the initial condition. It is thus crucial to assess the influence of the initial perturbation on the resulting dynamics. To do so, a small reminder on the growth dynamics of small fluctuations in the 1D Cahn-Hilliard is presented, yielding the growth rate dispersion relation.

3.3.1 1D perturbation growth dynamics

The perturbation dynamics in the 1D Cahn-Hilliard equation with constant mobility M is studied by considering an initial uniform composition field c_0 upon which a small fluctuation is added. More specifically, the composition field c is defined as,

$$c(\mathbf{r}, t) = c_0 + \epsilon\, \tilde{c}(\mathbf{r}, t) \ , \tag{3.10}$$

where $\epsilon \ll 1$ and $\tilde{c}(\mathbf{r}, t)$ is the function describing the stochastic fluctuation along x.
The Cahn-Hilliard equation can then be linearized at the first order in ϵ yielding,

$$\frac{\partial \tilde{c}}{\partial t} = M \left(f_0'' \frac{\partial^2 \tilde{c}}{\partial \mathbf{r}^2} - \kappa \frac{\partial^4 \tilde{c}}{\partial \mathbf{r}^4} \right) \ , \tag{3.11}$$

an evolution equation for the stochastic perturbation $\tilde{c}$, where f_0'' is the second derivative of the bulk free energy density f_0 evaluated at c_0.
The time evolution of the perturbation can then be studied by taking its spectral decomposition leading to,

$$\tilde{c}(\mathbf{r}, t) = \int_{-\infty}^{+\infty} \hat{\tilde{c}}(\mathbf{k}, 0) e^{\sigma(\mathbf{k})t} e^{-j\mathbf{k}\cdot\mathbf{r}} d\mathbf{k} \ , \tag{3.12}$$

where $\sigma(\mathbf{k}) = -M\left[f_0'' k^2 + \kappa k^4\right]$ the mode-dependent growth rate of the perturbation, leading to the dispersion relation in Figure 3.4. Whether the perturbation grows or shrinks, i.e. whether the perturbation is unstable or stable, depends on the sign of $\sigma(\mathbf{k})$.

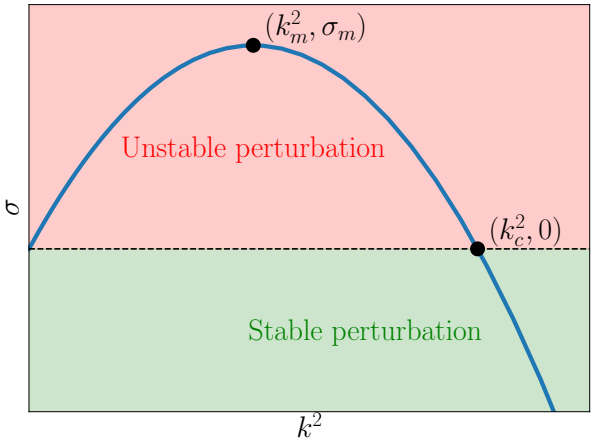

Figure 3.4. *Theoretical dispersion relation of the 1D perturbed Cahn-Hilliard equation. Quantities k_m and k_c are respectively the maximally growing wavenumber, associated with the maximum growth rate σ_m, and the critical wavenumber with a zero growth rate. The unstable (resp. stable) perturbation region, in red (resp. green), is such that wavenumbers, whose growth rate lies in this region, grow (resp. shrink) with time.*

When the curvature of the free energy density is positive ($f_0'' > 0$), the composition field is stable for all modes of the perturbation. However, when the curvature is negative the perturbation is unstable for all modes in the range $0 < k^2 < k_c^2$.

3.3.2 Growth rate estimation

The growth of the perturbation leads to the onset of ovulation as discussed in Chapter 2. Thus, the maximum growth rate σ_m is related to the breakup time t_b of the nanowire as,

$$\sigma_m \propto \frac{1}{t_b} \, . \tag{3.13}$$

The growth rate σ_m can be estimated by performing phase-field simulations of sinusoidal perturbations of the initial radius R of the nanowire. The initial perturbation defined in Equation 2.20 is then updated as,

$$R = R_0(1 + \epsilon \sin(\mathbf{k} \cdot \mathbf{r})) \quad \text{and} \quad R = R_0(1 + \epsilon(0.5 - \texttt{RAND()})) \, . \tag{3.14}$$

The wavenumber selection is then highlighted by comparing the expected maximally growing wavenumber k_m to the numerically obtained wavenumber of a stochastic initial perturbation. In addition, to quantify the effect of the initial perturbation amplitude, two different initial perturbation amplitudes ϵ are considered.

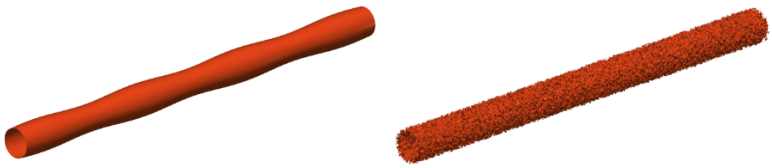

(a) (b)

Figure 3.5. *Contour plot* ($c = 0.5$) *of the initial morphology of an infinitely long free-standing nanowire under (a) a sinusoidal perturbation (b) a random stochastic perturbation.*

3.4 Results

In this section, the results of the phase-field simulations for the case of free-standing nanowires in two configurations, single free-standing nanowire and a junction of two free-standing nanowires. First, the choices of the mesh size and the dimensions of the computational box are discussed.

3.4.1 Sensitivity to numerical parameters

To assess the sensitivity of the simulation results to numerical parameters, a series of tests is conducted by varying both the mesh size and the dimensions of the computational domain. The domain must be large enough such that the periodic boundary conditions do not influence the results. Simulations are carried out in a computational box of size $L_x \times L_y \times L_z$, where $L_x = L_y = L_{box}$ denotes the smallest box dimension, using a mesh size $\Delta x = 0.5$ for a finite nanowire of radius R and length L. The breakup time is examined as a function of the ratio between the smallest box dimension and the nanowire radius, L_{box}/R (L_z is neglected in the analysis as it is the largest dimension of the system).

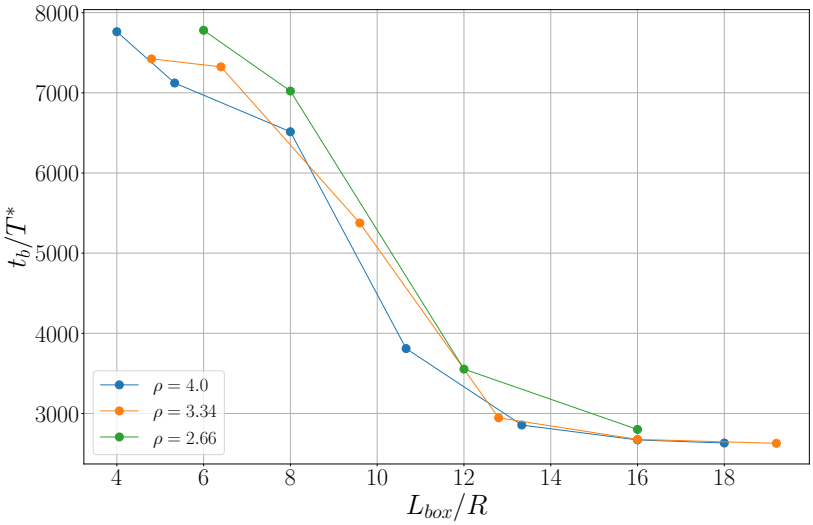

Figure 3.6. *Breakup time t_b/T^* with respect to the ratio between the smallest dimension of the computational box and the nanowire radius L_{box}/R for different values of the refinement factor $\rho = L^*/\Delta x$.*

The computational box size has a significant impact on the accuracy of the simulation results. The breakup time t_b converges to a constant value when the box is sufficiently large as to negates the effect of the periodic boundary condition. However, the computational cost increases with the square of the box smallest dimension, i.e. L_{box} and with the cube of the mesh size Δx. Thus a tradeoff between numerical accuracy and computational cost is necessary. The computational box size and mesh size are chosen such that there is a good balance between both constraints. For the rest of the thesis, the computational box size is set to $L_{box} \approx 13.3R$, with R the radius of the nanowire, since it both minimizes the computational domain size and maximizes the accuracy. The spatial refinement factor is set to $\rho = 4$ ($\Delta x = 0.5$ and $L^* = 2.0$). The temporal refinement is set to $\omega = 0.1$ ($\Delta t = 1.0$ and $T^* = 0.1$). As previously mentioned in Chapter 2, further temporal refinement does not provide a significant increase in accuracy.

3.4.2 Single free-standing nanowire

For the case of a single free-standing nanowire, two configurations are considered, the infinitely long and finite nanowire configurations. The goal is to perform phase-field simulations for different combinations of the characteristic quantities and the independent geometrical parameters, the initial radius R and the length of the nanowire L. The functional dependencies of both the breakup time t_b and the wavelength of the instability λ writes

$$t_b = f(R, L; L^*, T^*, E^*) \quad \text{and} \quad \lambda = g(R, L; L^*, T^*, E^*) \ . \tag{3.15}$$

Numerical experiments reveals that both the breakup time t_b and the wavelength of the instability λ are independent of the characteristic energy E^*. This result is presented in

Figure 3.7 where the total free energy of the system is plotted with respect to time for different values of E^* and constant L^* and T^*. This result can also be obtained by inspecting the Cahn-Hilliard equation with parameters $a\kappa$, aw and M_0/a with a a scaling factor. Different values of a yields different values of E^* while L^* and T^* remain identical. Substituting the parameters in the Cahn-Hilliard equation yields,

$$\frac{\partial c}{\partial t} = \nabla \cdot \left[M_0/a \nabla \left(awg'(c) - a\kappa \Delta c \right) \right] \ . \tag{3.16}$$

Thus, for any ϵ, the rate of change of c remain the same. This further confirms that t_b and λ are independent of the characteristic energy E^*.

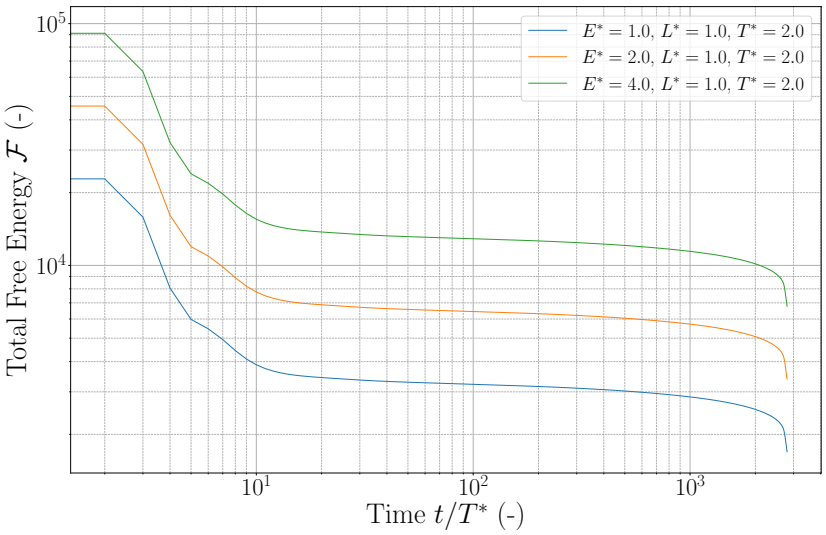

Figure 3.7. *Total free energy of the system with respect to time for different characteristic energy values E^* for constant L^* and T^*. The total free energy $\mathcal{F}$ is not scaled to the characteristic energy E^* for the sake of readability. The dynamics of the system remain the same for different characteristic energy values, suggesting that both the breakup time t_b and the wavelength of the instability λ are independent of E^*.*

Additional numerical experiments reveals that λ is independent of T^*, similarily to the prediction of Mao *et al.* [66] for surface-driven plate retraction.
The functional dependencies of t_b and λ can now be obtained by considering their independent parameters and their dimensionally independent subset of parameters. Buckingham–π theorem leads to the following relations,

$$\frac{t_b}{T^*} = F\left(\frac{R}{L^*}, \frac{L}{L^*}\right) \quad \text{and} \quad \frac{\lambda}{L^*} = G\left(\frac{R}{L^*}, \frac{L}{L^*}\right) \ , \tag{3.17}$$

or similarly,

$$\frac{t_b}{T^*} = F\left(\frac{R}{L^*}, \frac{L}{R}\right) \quad \text{and} \quad \frac{\lambda}{L^*} = G\left(\frac{R}{L^*}, \frac{L}{R}\right) \ , \tag{3.18}$$

with L/R the aspect-ratio Λ of the nanowire [6, 67, 75]. However, for the sake of clarity the inverse aspect ratio Λ is preferred as it naturally vanishes in the infinitely long limit.

Growth rate dispersion relation σ

The growth rate dispersion relation σ is evaluated by performing phase-field simulations of infinitely long free-standing nanowire under a sinusoidal perturbation of the initial radius for two different initial perturbation amplitudes ϵ. The results are reported in Figure 3.8.

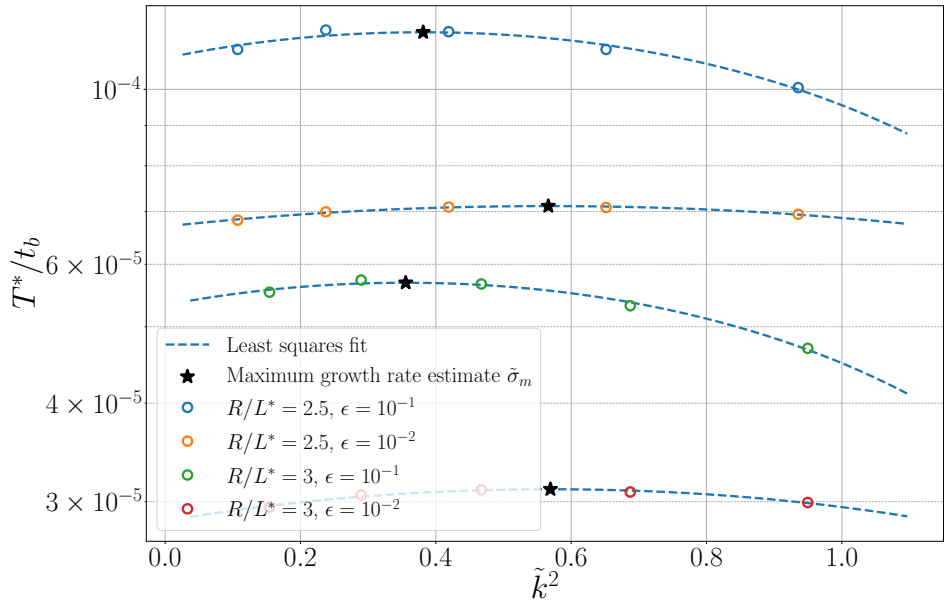

Figure 3.8. *Estimated growth rate $\tilde{\sigma} = T^*/t_b$ with respect to the radius normalized wavenumber $\tilde{k}$ squared. A least squares fit of the data reveals a quadratic relationship in $\tilde{k}^2$ as predicted theoretically. The wavenumber associated to the maximum growth rate varies with the initial perturbation amplitude ϵ.*

The maximally growing wavenumber k_m is estimated to be around $k_m \approx 0.7542R^{-1}$ corresponding to a wavelength of $\lambda_m \approx 8.33R$. This relationship is reported in Figure 3.10 and is taken as the relationship for infinitely long nanowires, i.e. $\Lambda = \infty$. Additional numerical experiments reveal that, under a stochastic perturbation, the same relationship is observed for the wavelength of the instability, highlighting the wavenumber selection mechanism of the instability growth. A comparison of morphological transformation between the sinusoidal and the stochastic perturbed infinitely-long free-standing nanowire is presented in Figure 3.14.

Dependence on the initial radius R/L^*

The functional dependencies being established, both the breakup time t_b/T^* and the wavelength of the instability λ/L^* can be studied with respect to the initial radius R/L^*. The growth rate dispersion relation in Figure 3.8 reveals that the breakup time t_b/T^* of infinitely long nanowires is linked to the initial radius R/L^* as a power law. In addition, the breakup time is influenced by the initial amplitude and nature of the perturbation. The breakup time t_b/T^*

is measured by performing phase-field simulations of finite length nanowires with different initial radii R/L^* and aspect ratios Λ/L^*. The results are presented in Figure 3.9.

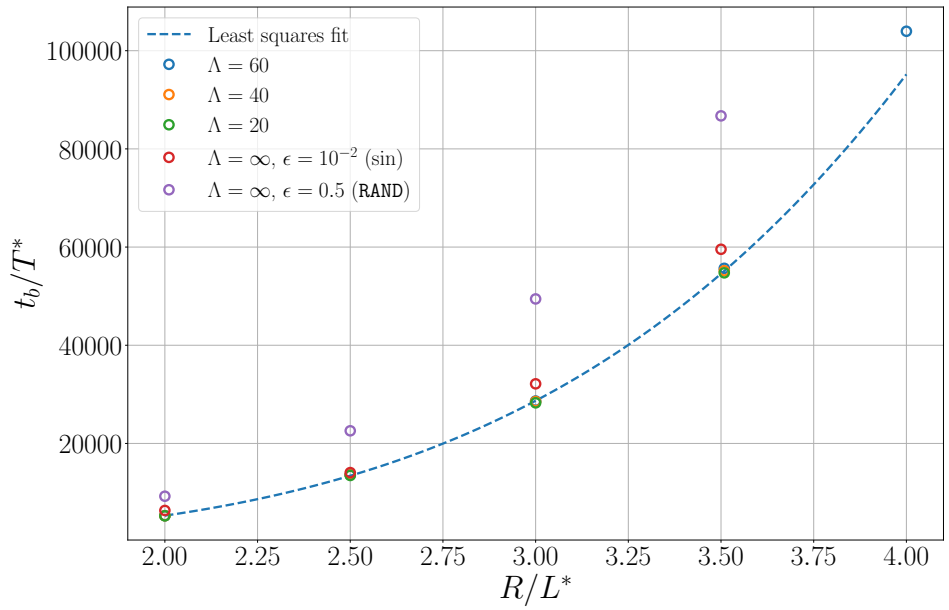

Figure 3.9. *Breakup time t_b/T^* with respect to the initial radius R/L^* for different values of the aspect ratio Λ. A least squares fit is performed revealing a power law relationship between the breakup time and the initial radius. The breakup time appears to be independent of the aspect ratio Λ provided that it is sufficiently large, i.e. $\Lambda \geq \Lambda_c$. The same power law is observed for $\Lambda = \infty$ with a dependence on the initial perturbation amplitude ϵ. For stochastic perturbations, the amplitude needs to be sufficiently large to observe the onset of ovulation.*

A least squares fit of the breakup time t_b/T^* reveals a power law dependance on the initial radius R/L^*,

$$\frac{t_b}{T^*} = \tau_\Lambda \left(\frac{R}{L^*}\right)^{4.16} , \tag{3.19}$$

with $\tau_\Lambda \approx 292.94$, the characteristic breakup time, approximately constant for all aspect ratios Λ. The characteristic breakup time is found to be similar for the case of infinitely long nanowires, albeit a contribution of the amplitude ϵ. This characteristic breakup time is therefore referred to as τ. For the case of finite length nanowires, the breakup dynamics were found to be insensitive to small fluctuations in the composition field. The dependence to the aspect ratio Λ is further investigated in the next section.
Additional numerical experiments are performed on the pentagonal cross-section nanowire in Figure 3.12. The breakup time scaling law is found to be similar to the circular cross-section nanowire, albeit with a smaller characteristic breakup time.

The wavelength of the instability λ/L^* is also measured as the nanodots interdistance as figured in both Figure 3.13 and Figure 3.14. The measurements are performed using the `Ruler` tool provided in the `Paraview` environment and are presented in Figure 3.10.

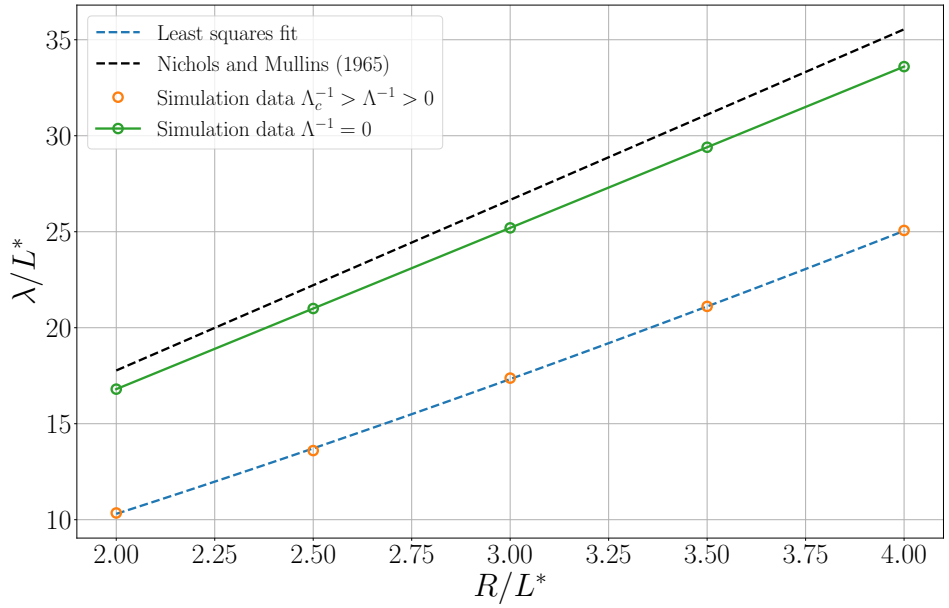

Figure 3.10. *Wavelength of the instability λ/L^* with respect to the initial radius R/L^* for different values of the length L/L^*. The wavelength λ/L^* is found to be independent on the aspect ratio Λ provided that it is sufficiently large, i.e. $\Lambda \geq \Lambda_c$. The wavelength associated to the maximum growth rate is taken from the growth rate dispersion relation. Nichols and Mullins [16] relationship between λ/L^* and R/L^* is plotted as a means for comparison. The instability wavelength is found to be close to the one predicted by Nichols and Mullins.*

The wavelength of the instability λ/L^* is found to follow a linear relationship with the initial radius R/L^* for both infinitely long and finite nanowires. In addition, the numerical results finds the wavelength of finite nanowires to be smaller than for infinitely long nanowires, $\lambda \approx 6.47R$ whereas for infinitely long nanowires $\lambda \approx 8.33R$.

Dependence on the aspect-ratio R/L

The effect of the aspect ratio Λ on the morphological evolution is studied. Following the same approach as for the infinitely long case, the functional dependencies of both the breakup time t_b and the wavelength of the instability λ can be evaluated with respect to the aspect ratio R/L for different values of the initial radius R/L^*. As revealed in the radius dependence section, both the breakup time and wavelength of the instability are found to be independent to the aspect ratio. However, numerical experiments reveal an aspect ratio threshold Λ_c for which the onset of ovulation cannot occur and the nanowire retracts to a sphere as shown in Figure 3.13, discussed in more details in Section 3.5. As can be seen in Figure 3.11, the breakup time t_b/T^* remains constant for all aspect ratios $\Lambda > \Lambda_c$, with Λ_c the critical aspect ratio under which the retraction of the nanowire length is too small for the onset of ovulation to lead to breakup. Both the breakup time t_b and the nanodot spacing λ are found to be independent of the initial perturbation.

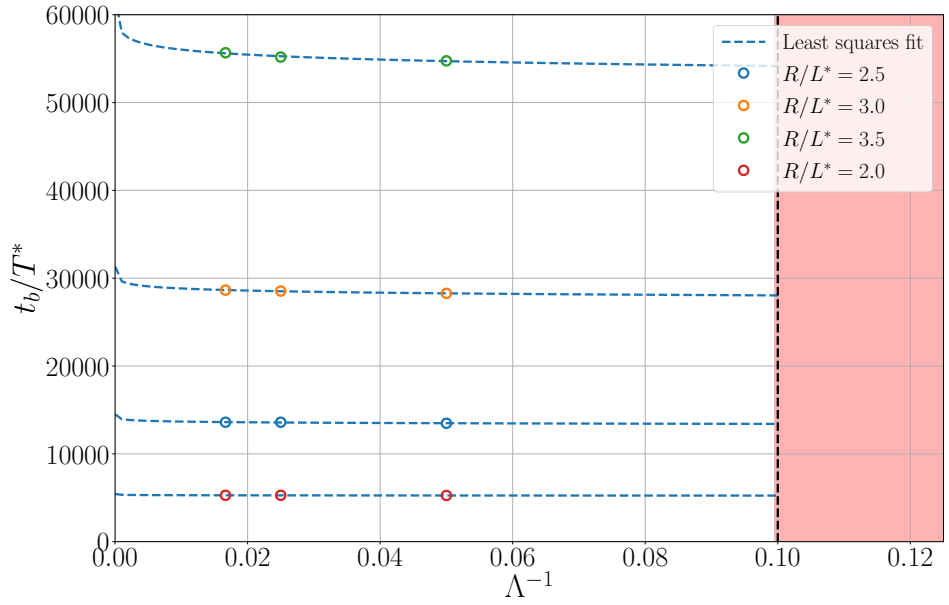

Figure 3.11. *Breakup time t_b with respect to the inverse of the aspect ratio, Λ^{-1}. The breakup time is constant across all Λ until reaching a threshold value Λ_c. For $\Lambda > \Lambda_c$, no breakup is observed.*

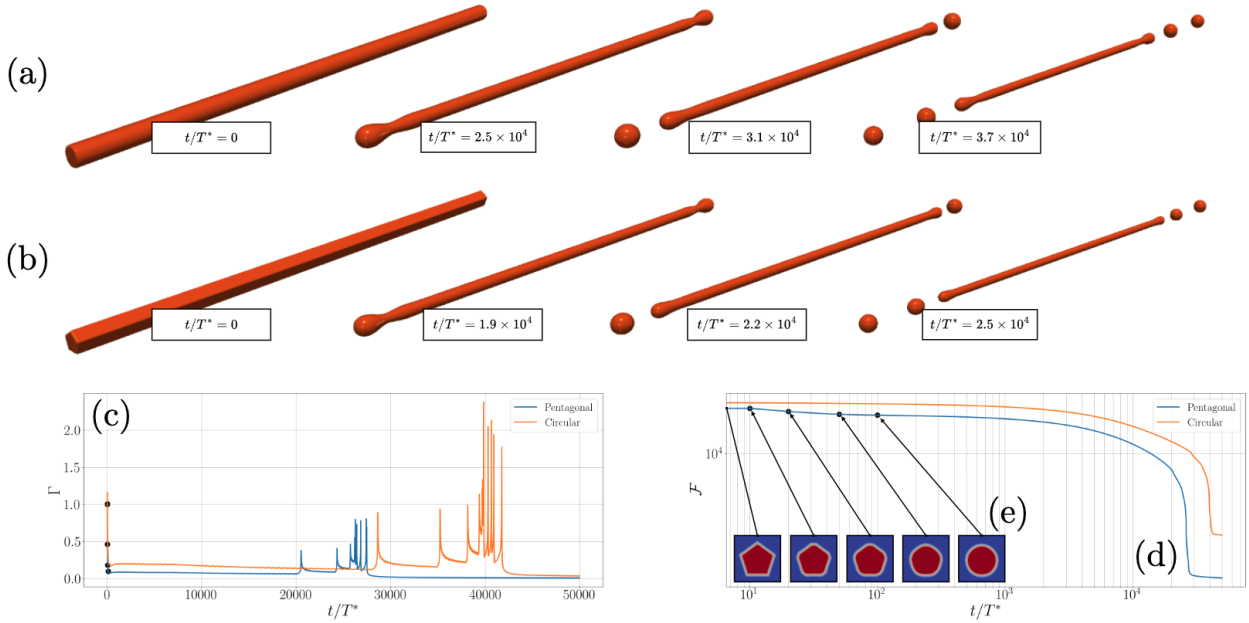

Figure 3.12. *Contour plot $(c+0.5)$ snapshots of the morphological evolution of a* (a) *circular* (b) *pentagonal cross-section nanowire with $R/L^* = 3$ and $\Lambda = 60$. The evolution of* (c) *the driving force Γ* (d) *the total free energy $\mathcal{F}$ during the transformation. In* (e)*, cross-sections of the pentagonal nanowire during the initial stages of the transformation. The breakup occurs faster for the pentagonal cross-section due to the initially high curvature at its corners.*

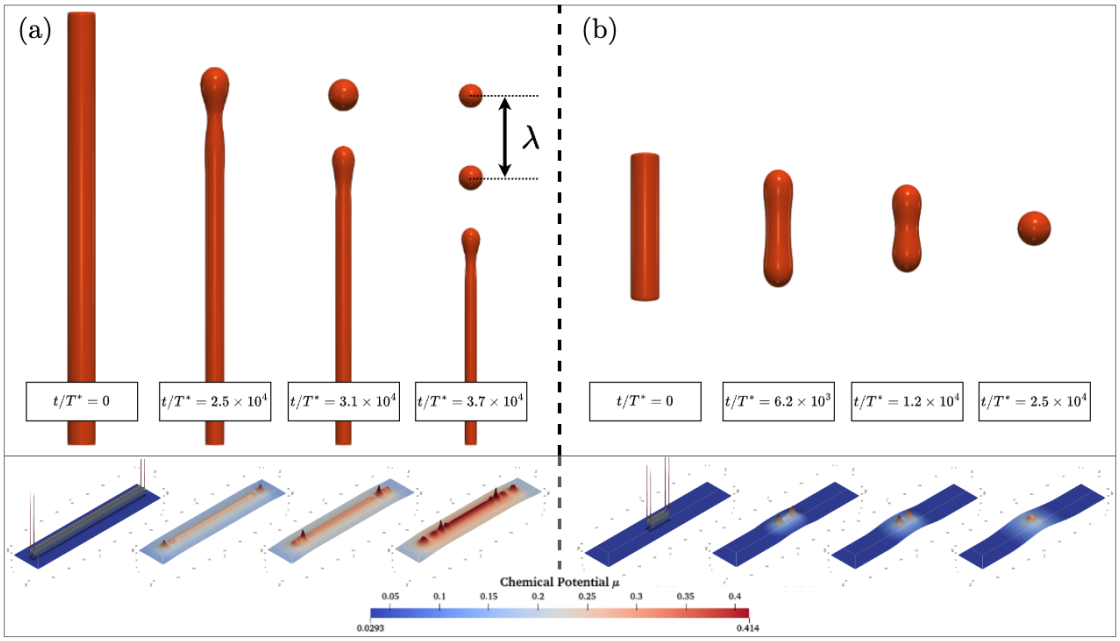

Figure 3.13. *Contour plot* ($c = 0.5$) *snapshots of the morphological evolution of a nanowire of* (a) $\Lambda = 60$ (b) $\Lambda = 10$. *Above* Λ_c, *the nanowire free ends bulge out and retract. As the retraction progresses, necking intensifies at the free ends leading to the formation of a nanodot. Below* Λ_c, *the length is not sufficient to develop sufficient necking at the free ends.*

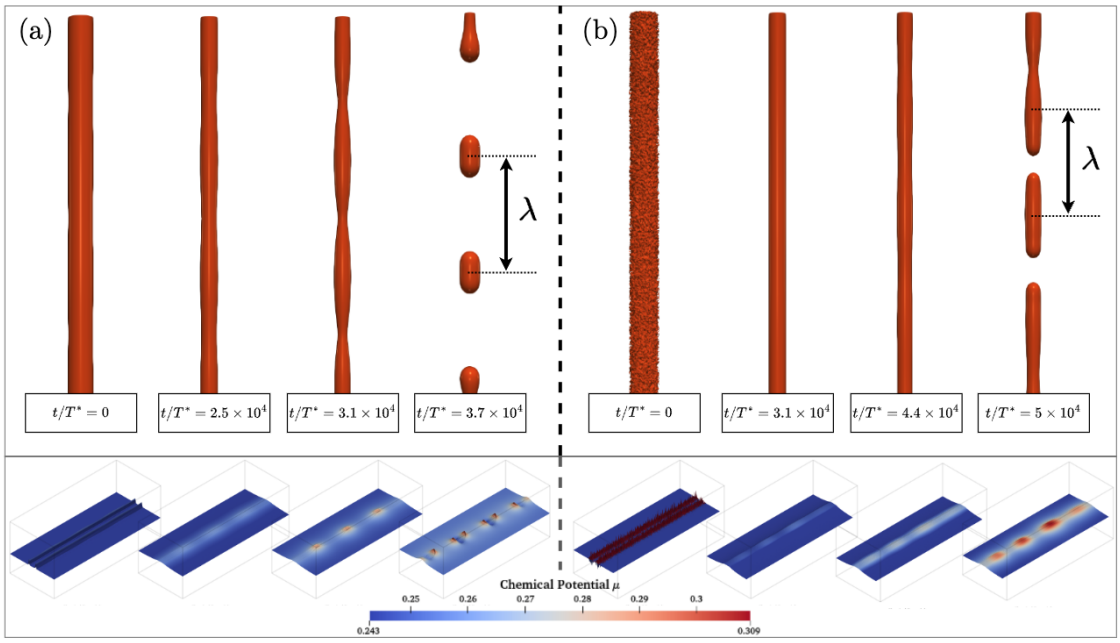

Figure 3.14. *Contour plot* ($c = 0.5$) *snapshots of the morphological evolution of a nanowire with an initial* (a) *sinusoidal* ($k = k_m$, $\epsilon = 10^{-2}$) (b) *stochastic* ($\epsilon = 0.5$) *perturbation. The nanowire starts from a textured morphology, then smoothes out as the dynamics progress until equally spaced bulges grow, leading to necking and eventually the breakup of the nanowire.*

3.4.3 Junction of two free-standing nanowires

Finally, for the case of a junction of two free-standing nanowires, the same method is applied to characterize the functional dependency of the breakup time t_b. The wavelength λ is not considered in the discussion here, as the stability of the junction is, in this case, the most relevant factor. In this context, two characteristic time are studied, $t_{b,1}$ and $t_{b,2}$ corresponding to the break up time of the primary and secondary nanowire respectively. The functional dependencies are thus written as

$$t_{b,i} = h_i(R_1, R_2, L; L^*, T^*, E^*) \ , \tag{3.20}$$

with $i = 1, 2$ for the primary and secondary nanowire, respectively. The relative orientation is neglected in this case as it was already studied by Roy *et al.* [14]. The relative orientation considered in the study is $\theta = 90°$ since it leads to the fastest breakup of the junction.
Similarly to the case of a single free-standing nanowire, the breakup time $t_{b,i}$ is found to be independent of the characteristic energy E^* values. The functional dependencies of the breakup time $t_{b,i}$ can then be expressed as,

$$\frac{t_{b,i}}{T^*} = H_i\left(\frac{R_1}{L^*}, \frac{R_2}{R_1}\right) \ , \tag{3.21}$$

with R_1/R_2 the relative aspect ratio.

Dependence on the initial radius R_1/L^*

Numerical simulations are performed by varying the initial radius R_1/L^* for constant values of the relative aspect ratio R_1/R_2. Both breakup times are measured and reported in Figure 3.15. Numerical fits of the data reveal a power law relationship between both breakup times and the iniital radius R_1/L^*,

$$\frac{t_{b,i}}{T^*} = \tau_i\left(r\right)\left(\frac{R_1}{L^*}\right)^{3.921} \ , \tag{3.22}$$

with $\tau_i(R_1/R_2)$ the characteristic breakup time of the primary ($i = 1$) and secondary ($i = 2$) nanowire for a relative aspect ratio $r = R_1/R_2$. The characteristic breakup time $\tau_i(r)$ is evaluated in the next section. The power law relationship reveals a quartic dependence of the breakup time on the initial radius R_1/L^*, similar to the case of a single free-standing nanowire.

Dependence on the relative aspect-ratio R_1/R_2

Similarly, the functional dependencies of the breakup time $t_{b,i}$ can be studied with respect to the relative aspect ratio R_1/R_2 for different values of the initial radius R_1/L^*. The results are reported in Figure 3.15. Numerical fits also reveal a power law relationship between the breakup time and the relative aspect ratio. Combining both relationships leads to

$$\frac{t_{b,1}}{T^*} \approx \tau_j\left(\frac{R_1}{L^*}\right)^{3.921}\left(\frac{R_1}{R_2}\right)^{0.74} \quad \text{and} \quad \frac{t_{b,2}}{T^*} \approx \tau_j\left(\frac{R_1}{L^*}\right)^{3.921}\left(\frac{R_1}{R_2}\right)^{-4.63} \ , \tag{3.23}$$

with $\tau_j \approx 263.58$, which is close to the characteristic breakup time of a single free-standing nanowire $\tau \approx 292.94$.

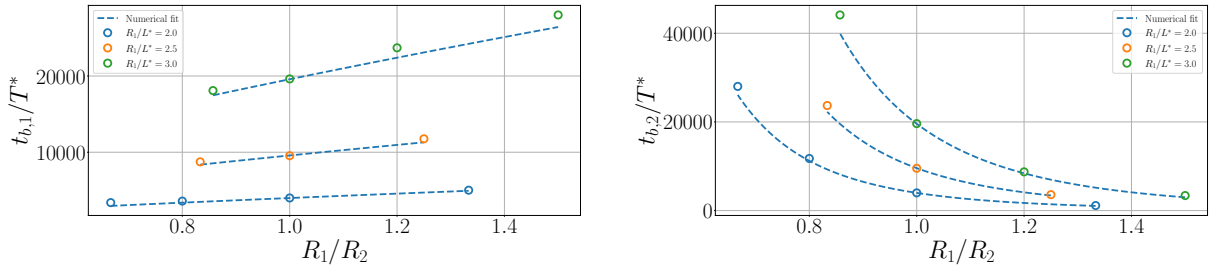

Figure 3.15. *Breakup time of* (a) *the primary nanowire* $t_{b,1}$ (b) *the secondary nanowire* $t_{b,2}$ *with respect to the relative aspect ratio* R_1/R_2 *for different values of the initial radius* R_1/L^*. *Numerical fits of the data reveal a power law relationship between the breakup time, the radius and the relative aspect ratio.*

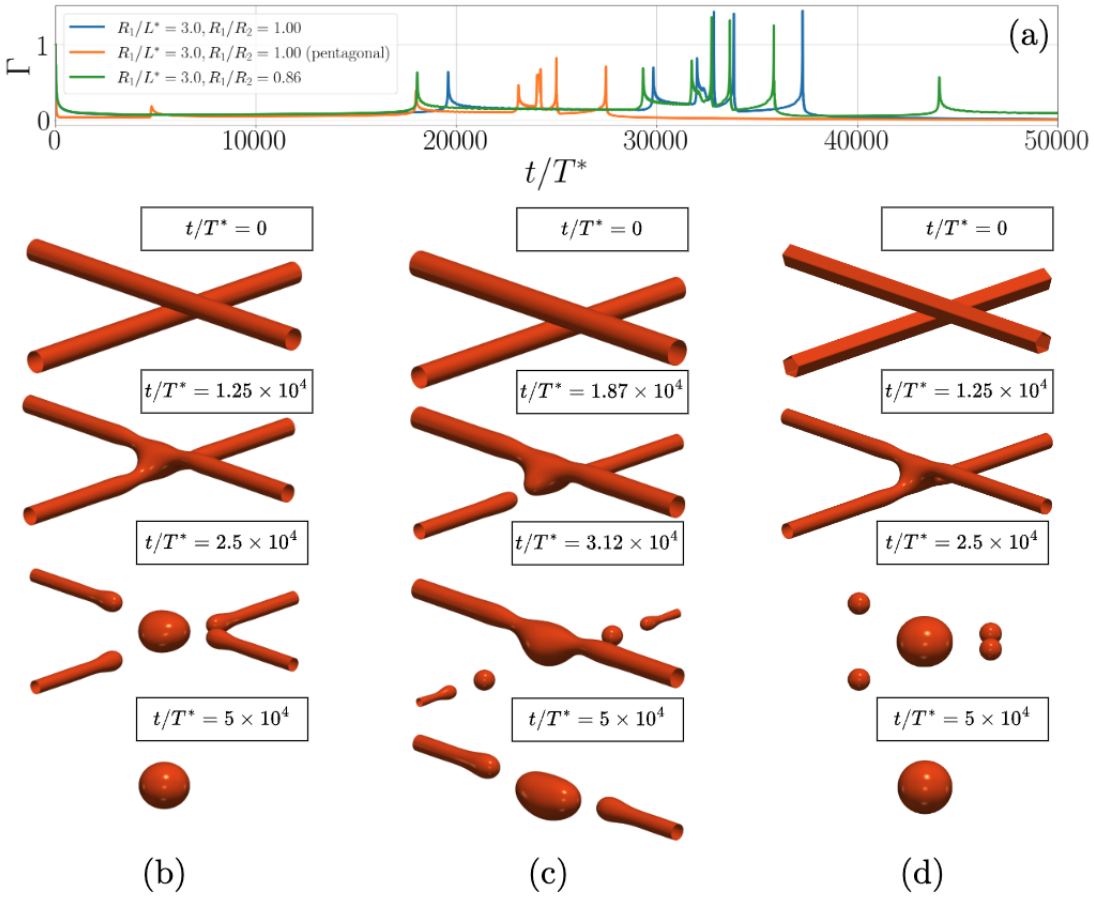

Figure 3.16. *Comparison of the morphological evolution of different junctions of two free-standing nanowires.* (a) *Driving force* Γ *with respect to time. Contour plot* ($c = 0.5$) *snapshots of the morphological evolution of* $R_1/L^* = 3$ *and* (b) $R_1/R_2 = 1$ (c) $R_1/R_2 = 0.86$ (d) $R_1/R_2 = 1.0$ *with a pentagonal cross-section.*

3.5 Discussion

The results obtained from the phase-field simulations of single free-standing nanowires align well with the classical framework made by Nichols and Mullins [16, 17] for the capillarity-driven evolution of solids of revolution.
The maximally growing wavelength measured in the simulations of infinitely long nanowires λ_m is found to be approximately $8.33R$ which closely matches the analytical prediction of $\lambda_m = 2\pi\sqrt{2}R \approx 8.88R$. In addition, for the finite-length nanowires, the measured wavelength, i.e. the distance between resulting nanodots, is observed to be smaller than the maximally growing wavelength. This result is also consistent with the findings of Nichols [17] where the distance between the growing bulges is found to be approximately equal to the critical wavelength, i.e. $\lambda \approx \lambda_m/\sqrt{2}$. This result can be attributed to the interplay between retraction and contra-diffusion [17, 75]. As shown in Figure 3.13, the central region of the nanowire acts as the source of mass transfer while the free ends acts as sinks. The intensity is therefore found to be dependent on the difference in curvature, indicated by the chemical potential μ in Figure 3.13, between the source and the sinks. The free ends grow radially while the source shrinks, leading to the formation of a neck and subsequent breakup. The wavelength of instability is therefore found to be the smallest possible wavelength that allows instabilities to develop, i.e. the critical wavelength λ_c. However, for increasingly large nanowires, one would expect the wavelength to approach the maximally growing wavelength λ_m. However, this is not the case as explained by Nichols [17]. As the rod gets longer, the formation of additional bulges becomes possible, leading to a stabilizing effect. This effect thus leads to the formation of an additional nanodot, and increasingly more nanodots as the length increases. The observation further confirms the relevance of the phase-field approach to model the morphological evolution of nanowires. In addition, the presence of a critical aspect ratio is explained by the same arguments.

A key observation in the present study is the identification of two breakup mechanisms, perturbation-driven and free-end-driven breakup. The latter, as reported in Figure 3.9, leads to a more rapid evolution, with the breakup initiating from the ends of the nanowire, as opposed to the perturbation-driven, where the initial amplitude of the perturbation is found to be a 'limiting factor'. The morphological transformation of an infinitely long nanowire under a stochastic perturbation of amplitude equal to $0.5R$ shown in Figure 3.14 illustrates this argument. The amplitude, while being large enough to be significantly noticeable, leads to breakup times larger than the ones observed for finite-length nanowires. This difference in dynamics further motivates the importance of considering finite-length rods to model the morphological evolution of nanowires. This is further supported by SEM images revealing the formation of nanodots emerging from the nanowire ends, illustrated in Figure 3.17. As for the breakup time scaling law, the quartic dependence on the initial radius R is found to be consistent with the theoretical predictions of Nichols and Mullins [16, 17], of McCallum *et al.* [18] and Balty *et al.* [28]. Furthermore, the expression can be expanded in terms of the physical parameters of the Cahn-Hilliard equation as follows,

$$\frac{t_b}{T^*} \approx \tau \left(\frac{R}{L^*}\right)^4 \implies t_b = \tau \left(\frac{R}{L^*}\right)^4 T^* \tag{3.24}$$

The characteristic time T^* can be expressed as,

$$T^* = \frac{\kappa}{w^2 M_0} = \frac{\kappa}{w D_s} g''(c) \tag{3.25}$$

$$= \frac{\kappa}{\sqrt{w}^2 D_s} \frac{\sqrt{\kappa}}{\sqrt{\kappa}} g''(c) \tag{3.26}$$

$$= \frac{\kappa L^*}{\gamma D_s} g''(c) \ , \tag{3.27}$$

with D_s the surface diffusivity, $g''(c)$ the curvature of the homogeneous free energy $f_0(c) = wg(c)$ and γ the characteristic surface energy.
Injecting the above relationships from Equation 3.5 in the expression of the breakup time t_b leads to the following expression,

$$t_b = \tau \frac{\kappa R^4}{\gamma D_s {L^*}^3} g''(c) \ . \tag{3.28}$$

As recalled in Chapter 1, the homogenous free energy f_0 is a function of the temperature T and its curvature is found to vanish at the critical temperature T_c. Thus, while recovering the expression found by Balty *et al.* [28], the present work introduces a temperature-based criterion for the onset of the instability, where the curvature of the homogeneous free energy $g''(c)$ vanishes at the critical temperature T_c [9, 11].

The analysis of the nanowire morphology reveals that the initial morphology can lead to accelerated breakup kinetics. This further motivates the need of future modeling efforts to include the correct polycrystalline structure of the nanowires. The accelerated kinetics in pentagonal cross-section nanowires can be attributed to the increased curvature gradients at each edge. Nevertheless, the scaling laws remain unchanged, suggesting that the underlying physics is similar.

As for the case of junctions, as previously stated, the study focused on junction with a relative orientation of $\theta = 90°$, which is the configuration identified by Roy *et al.* [14] as exhibiting the fastest breakup kinetics among various relative orientations. This choice facilitates the parametric study while predicting that other angles would lead to slower kinetics without altering the underlying physical interpretation. The numerical results of the junction reveal a power-law scaling of the breakup times $t_{b,1}$ and $t_{b,2}$ with respect to the primary nanowire radius R_1/L^* and the relative aspect ratio R_1/R_2.

To minimize the risk of breakup in nanowire networks, the relative aspect ratio R_1/R_2 should ideally approach unity. Moreover, the behavior of the primary nanowire, whose breakup time depends on the relative aspect ratio R_1/R_2, i.e. the relative size of the two branches, suggests that it can be used to estimate the breakup initiation around localized surface defects. In this context, the defect would act as a short secondary nanowire. As the relative size of the defect decreases, the breakup time increases, and eventually diverges as the size of the defect becomes increasingly negligible with respect to the primary nanowire. This observation is consistent with experimental findings where nanowire degradation can often initiate at regions of substantial local defects.

Additionally, junctions composed of pentagonal cross-section nanowires are found to follow the same morphological transformation as their cylindrical counterparts, albeit with noticeably faster kinetics. This observation further emphasizes the significant role of faceting in the morphological evolution of nanowires. The pentagonal cross-section leads to an increased curvature gradient at the edges, accelerating the breakup process.

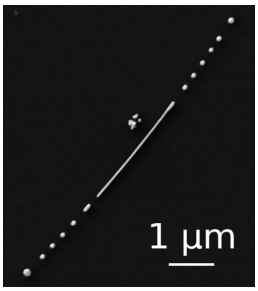

Figure 3.17. *SEM image of an AgNW with nanodots emerging from the free ends. The image is taken from Balty et al.* [28].

A comparison with the earlier work by Roy *et al.* reveals several particular distinctions. While their study provided valuable insights into the application of the phase-field formalism to surface-enhanced diffusion, certain aspects of their numerical framework limited the robustness and generalizability of their results. In particular, their use of a relatively small computational domain, coupled with physical parameters that led to a diffuse interface width larger than the nanowire radius, introduced significant boundary effects and reduced the fidelity of bulk behavior. Moreover, their methodology lacked a systematic non-dimensionalization of the governing equations and parameters, which limits the interpretability and scalability of their findings to other physical systems. In contrast, the present work is built upon a coherent non-dimensional framework, allowing the derivation of scaling laws and making the results directly transferable to a wide range of materials and experimental conditions.

Additionally, their use of a sharp interface definition for the initial condition introduced numerical oscillations during the early stages of the morphological evolution, which in turn led to a mischaracterization of the breakup mechanism. Specifically, this artifact contributed to the incorrect conclusion that perturbation-driven breakup is largely independent of initial amplitude and progresses as rapidly as breakup driven by free-end retraction. The present simulations, by contrast, use a physically consistent diffuse-interface initialization, which captures more accurately the dynamics of instability growth and allows a clearer distinction between the dominant breakup regimes.

Chapter 4

Nanowire on substrate

In this chapter, an extension of the Cahn-Hilliard equation is presented to model the influence of a flat substrate on which the nanowires are deposited. First, the modified Cahn-Hilliard equation is detailed by introducing the concept of Smoothed Boundary Method (SBM) [15, 76–78] and how a contact angle condition is implemented. After the implementation is validated, a brief discussion on how the condition can accurately model the influence of the substrate in the case of nanowire morphological instability is presented. Then, the geometry of the problem is defined. Finally, a comparative analysis is performed, comparing the results between the free-standing and the substrate-influenced configurations.

4.1 Smoothed Boundary Method

Partial differential equations require the definition of boundary conditions for a solution to be unique. However, when solving PDEs numerically, treating the boundary conditions can be challenging. In particular, when the computational domain has complex geometries, the computational cost associated to the construction of a sufficiently accurate grid can be a limiting factor. Fourier spectral methods, while giving very accurate numerical approximations of solutions, are limited to simple geometries and periodic boundary conditions. In this context, Bueno-Orovio *et al.* [79–81] introduced the Spectral Smoothed Boundary Method (SSBM), a domain embedding method that allows the automatic treatment of boundary conditions by reformulating the PDEs through the use of an order-like parameter ψ, inspired by the phase-field formalism. Yu *et al.* [15, 76] expanded the formalism to any boundary condition treatment as the initial work was limited to the no-flux Neumann boundary condition.

4.1.1 Mathematical derivation

The method is based on a diffuse interface description of the boundary condition, similar to the phase-field formalism used in the presented work [15]. In this context, the internal domain is defined using an order-parameter-like field, ψ the domain parameter, which is

defined as,

$$\psi(\mathbf{x},t) = \begin{cases} 1 & \text{if } \mathbf{x} \text{ in } \Omega, \\ 0.5 & \text{if } \mathbf{x} \text{ on } \Gamma_s, \\ 0 & \text{if } \mathbf{x} \text{ in } \Omega_s. \end{cases} , \tag{4.1}$$

where Ω is the internal domain, Γ_s the boundary on which the condition is applied, and Ω_s the external domain.

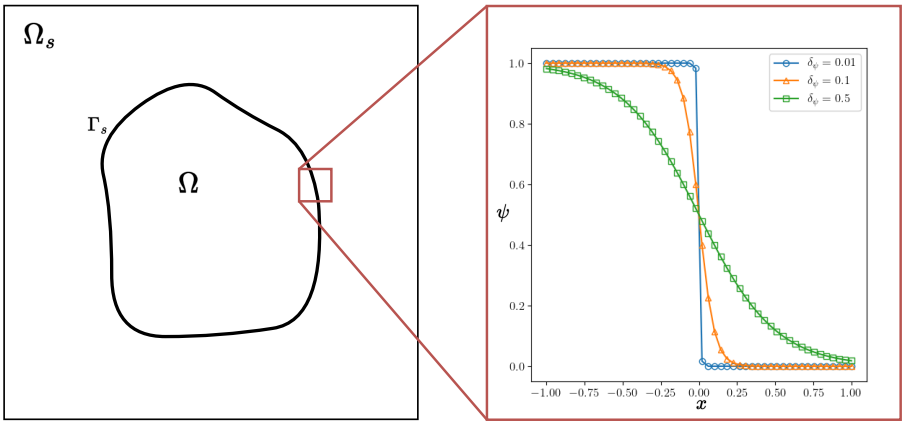

(a) (b)

Figure 4.1. (a) *Example of an irregular domain* Ω *with* Γ_s *the boundary of said domain and* Ω_s *the external domain.* (b) *1D representation of the domain parameter at the boundary* Γ_s *for different value of the characteristic width* δ_ψ *of domain parameter* ψ*.*

Conveniently, the gradient of the domain parameter $\nabla\psi$ describes the inward normal to the boundary Γ_s.
In general, when solving PDEs, the boundary conditions can either be Dirichlet, Neumann or Robin. Both the Dirichlet and Neumann conditions can be rewritten in terms of the domain parameter by considering the following relations. In the case of the Neumann boundary condition, consider the product of the domain parameter by the Laplacian of an arbitrary function H. The product rule identity leads to the following relation,

$$\psi\nabla^2 H = \nabla\cdot(\psi\nabla H) - \nabla\psi\cdot\nabla H \ . \tag{4.2}$$

The relationship involves the gradient of the domain parameter $\nabla\psi$ which, as previously stated, describes the inward normal of the boundary. Indeed, the inward normal $\mathbf{n_s}$ is given by $\nabla\psi/|\nabla\psi|$. In addition, a Neumann boundary condition of an arbitrary function H can be written as

$$\frac{\partial H}{\partial \mathbf{n_s}} = \nabla H\cdot\mathbf{n_s} = N \quad \text{on} \quad \Gamma_s \ . \tag{4.3}$$

As a result, the Neumann boundary condition can be imposed by substituting $\nabla\psi\cdot\nabla H$ with the prescribed condition N,

$$\psi\nabla^2 H = \nabla\cdot(\psi\nabla H) - N|\nabla\psi| \ . \tag{4.4}$$

The gradient of the domain parameter being non-zero only on the boundary Γ_s, the contribution of the second term occurs only on the boundary. With the formalism presented, the following provides the requirements to impose a contact angle Neumann boundary condition to the Cahn-Hilliard equation.

4.1.2 Modified Cahn-Hilliard equation

As stated in Section 1.3, the requirement for the system to reach equilibrium is the minimization of the total free energy. In other terms, the variational derivative of the free energy functional vanishes at equilibrium which leads to the Euler-Lagrange equation defined in Equation 1.8. The Euler-Lagrange equation can be rewritten by multiplying both sides by the gradient of composition ∇c,

$$\frac{\partial f_0}{\partial c}\nabla c - (\kappa\nabla^2 c)\nabla c = \frac{\partial f_0}{\partial c}\frac{\partial c}{\partial \mathbf{x}} - \frac{\kappa}{2}\nabla(|\nabla c|^2) = 0 \ . \tag{4.5}$$

The first term can be rewritten as ∇f_0, and the second term as $\frac{\kappa}{2}\nabla(|\nabla c|^2)$. Integrating both sides leads to the following equality,

$$|\nabla c| = \sqrt{\frac{2}{\kappa} f_0} \ , \tag{4.6}$$

where the integration constant vanishes since f_0 in the bulk vanish. This equality will be particularly useful when defining the desired contact angle condition.
The contact angle θ_B is the dihedral angle [82] formed at the junction between three phases, or in a binary system, the two phases α and β (film – vapor) and the solid surface (substrate).

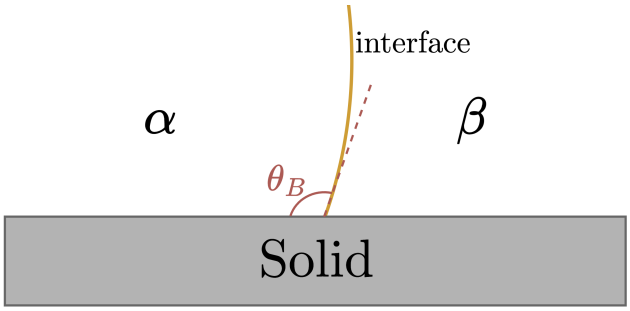

Figure 4.2. *Contact angle θ_B at the junction between three phases i.e. the binary system α–β and the solid surface. Adapted from* [82]

The composition-substrate interaction is modeled by a boundary condition which prescribes a specific contact angle at the junction, which follows Young's equality [82],

$$\gamma_{\alpha\beta}\cos\theta_B = \gamma_{\beta s} - \gamma_{\alpha s} \ , \tag{4.7}$$

where $\gamma_{\alpha\beta}$ is the interfacial energy density between α and β, i.e. the film surface energy density. The prescribed contact angle condition is then imposed by considering,

$$\mathbf{n_c}\cdot\mathbf{n_s} = \cos\theta_B \ , \tag{4.8}$$

where $\mathbf{n_c}$ and $\mathbf{n_s}$ are respectively the outward normal to the α–β interface and the inward normal to the substrate. The outward normal $\mathbf{n_c}$ is expressed as $-\nabla c/|\nabla c|$ (pointing toward $c = 0$), while the inward normal to the substrate is given by $\nabla\psi/|\nabla\psi|$. Therefore, the contact angle boundary condition can be rewritten as

$$\nabla c \cdot \nabla\psi = -|\nabla c| \cos\theta_B |\nabla\psi| \ . \tag{4.9}$$

Substituting Equation 4.6 in the above leads to

$$\nabla c \cdot \nabla\psi = \underbrace{-\sqrt{\frac{2}{\kappa} f_0} \cos\theta_B}_{N} |\nabla\psi| \ . \tag{4.10}$$

The boundary condition expression derived above is similar to the one suggested by Warren *et al.* [83] where the substrate is treated as a sharp wall. In the sharp interface limit, both conditions are equivalent. However, the SBM formalism allows for a diffuse interface description of the boundary condition, which is more suitable for numerical simulations.
Following the same reasoning as [15], the composition field c can be confined within Ω_M by multiplying both sides of Equation 2.1 and Equation 2.2 by the domain parameter ψ. Using the modified Cahn-Hilliard equation leads to

$$\psi \frac{\partial c}{\partial t} = \nabla \cdot (\psi M(c) \nabla\mu) - (M(c)\nabla\mu) \cdot \nabla\psi \tag{4.11}$$

$$\psi\mu = \psi \frac{\partial f_0}{\partial c} - \kappa \nabla \cdot (\psi \nabla c) - \sqrt{2\kappa f_0} \cos\theta_B |\nabla\psi| \ . \tag{4.12}$$

As recalled in Equation 1.11, the term $M(c)\nabla\mu \cdot \nabla\psi$ corresponds to the flux of composition across the substrate, which is null to ensure mass conservation in the domain.

4.1.3 Validation

The proposed approach at modeling a contact-angle condition using the SBM formalism is validated by considering the simple case of a 2D square droplet on a flat substrate under different contact angle conditions. The domain order parameter ψ is defined as

$$\psi(x, y, z) = \frac{1}{2}\left[1 + \tanh\left(\frac{y_\psi - y}{\delta_\psi}\right)\right] \ , \tag{4.13}$$

with y_ψ the position along the y–axis of the interface between the substrate and the domain, and δ_ψ the characteristic width of the substrate diffuse interface.
The square droplet is initialized as a rectangular composition field of size $l \times h$ with $l = 20$ $(-)$ and $h = 100$ $(-)$. The substrate characteristic width δ_ψ is chosen as per Yu *et al.* [15] recommendation, i.e. as a few Δx units. Contour plots of the square droplet for different prescribed contact angles θ_B are shown in Figure 4.3.

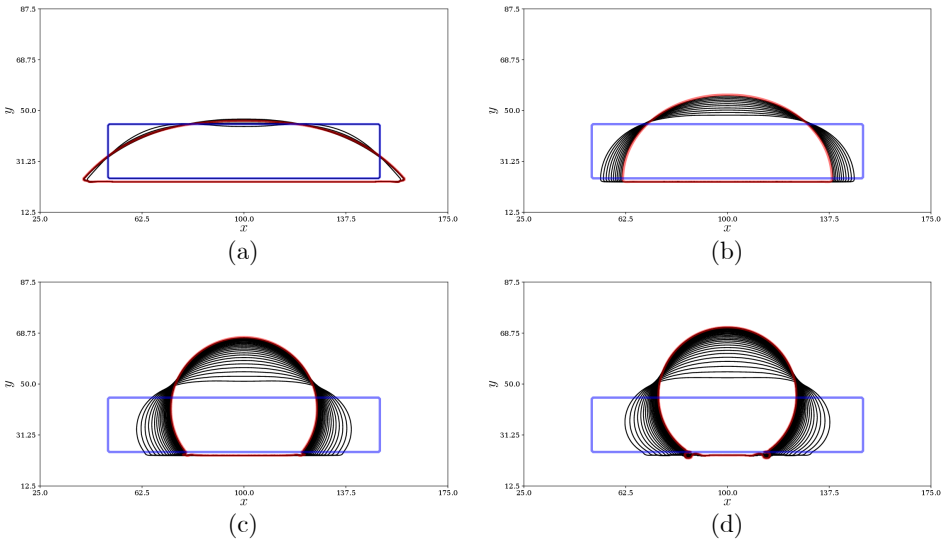

Figure 4.3. *2D profile* ($c = 0.5$) *of the square droplet and its equilibrium profile for different contact angles.* (a) $\theta_B = 45°$ (b) $\theta_B = 90°$ (c) $\theta_B = 135°$ (d) $\theta_B = 180°$. *The initial profile is shown in blue, the profiles at different timesteps in black, and the equilibrium profile, chosen as the profile for which the total free energy is constant, is shown in red. Discrepancy between the prescribed contact angle and the equilibrium contact angle for the case of* $\theta_B = 180°$ *can be indicative of the influence of the spatial refinement on the composition field.*

Numerical experiments show that choosing a too thin substrate, i.e. a small interfacial width, can lead to numerical instabilities due to the sharpness of the boundary. In addition, choosing a too large interfacial width can greatly influence the initial condition of the system. The optimal interfacial width is thus chosen in order to reduce the risk of numerical instabilities whilst keeping the composition field intact. For the rest of the chapter, the substrate interfacial width is taken such that it matches with the composition interfacial width.
The SBM formalism, now implemented and validated, can be used to model nanowires deposited on a flat substrate.

4.2 Model of the configuration

In this section, the configuration of the problem is defined. First, the contact angle condition is discussed from images of spheroidized nanowires. Then, the geometry of the nanowires are defined, for both the circular and pentagonal cross-section approximation. Finally, the configurations are presented for both the single nanowire and the junction of two nanowires.

4.2.1 Contact angle condition

Several SEM images of polyol-grown Silver nanowires after spheroidization are analysed to crudely measure the contact angle between the nanowires and the substrate. An example of

SEM image is shown in Figure 4.4. The experimental contact angle are measured using the `ImageJ` software [84]. The contact angle θ_B can be measured using the relation,

$$\theta_B = \arctan \frac{2h}{w} \ , \tag{4.14}$$

where h is the height of the spheroid and w is the width of the spheroid on the substrate. After measuring the contact angle of 70 spheroids, the contact angle θ_B is found to be in average,

$$\theta_B \approx 105.567 \pm 6.977 \ ^\circ \ . \tag{4.15}$$

As shown in Figure 3.2, the nanowires have a regular pentagonal cross-section. The interior angle of a regular pentagon is 108°. Therefore, it can be assumed that the contact angle θ_B remains constant throughout the spheroidization process and is equal to the initial contact angle, i.e. the interior angle of the nanowire cross-section.

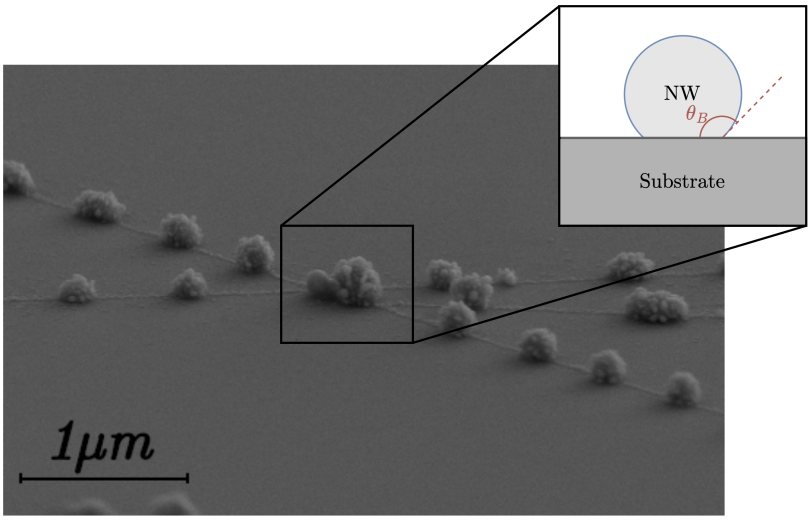

Figure 4.4. *Scanning electron microscopy (SEM) image of a polyol-grown Silver nanowire after spheroidization showing a contact angle θ_B between the spheroids and the flat substrate.*

4.2.2 Geometry

Two configurations of the nanowire shape are considered, the circular approximation and the pentagonal cross-section. As previously established in Section 2.4, surface energy minimization is the driving force behind the morphological instability of the nanowires. Thus, the geometry of the circular approximation of the nanowire is defined such that the outer surface area matches the outer surface area of the pentagonal cross-section nanowire [28]. The cross-section of both configurations is shown in Figure 4.5.

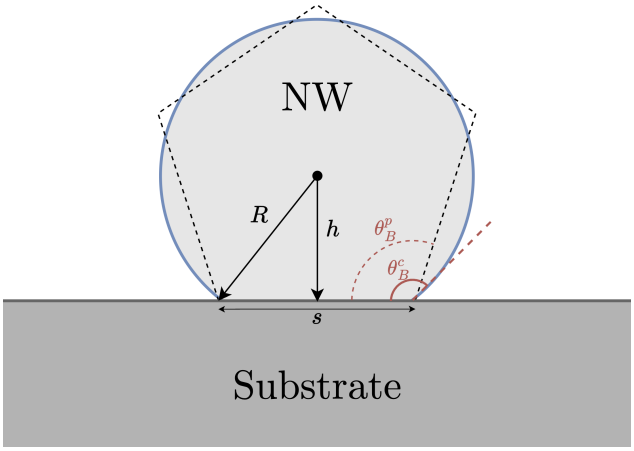

Figure 4.5. *Geometrical configuration of both the pentagonal and circular cross-section. R is the radius of the circular approximation and h is the distance from the center of the circular cross-section to the substrate. The angles θ_B^p and θ_B^c are respectively the contact angle the pentagonal ($= 108°$) and the circular cross-section. The value of θ_B^c is chosen such that the outer surface area in contact with the vapor phase (exterior) matches the outer surface area of the pentagonal cross-section. Adapted from* [28].

Following the same strategy as Balty *et al.* [28], the condition of outer surface matching writes as follows,

$$4s = 2\theta_B^c R \implies s = \frac{\theta_B^c}{2} R \,. \tag{4.16}$$

Using trigonometry, the side length s can also be expressed as, $s = 2R\sin\theta_B^c$. This finally leads to

$$4\sin\theta_B^c = \theta_B^c \implies \theta_B^c \approx 141.8° \,. \tag{4.17}$$

The substrate is located at a distance $h = |R\cos\theta_B^c|$ from the center of the circular cross-section and at a distance $a_p = s/2\cot\frac{\pi}{5}$, i.e. the apothem, from the center of the pentagonal cross-section. These quantities are used in the SBM formalism to define both the contact angle and the position of the substrate in the following.

As for the junction configuration, the primary nanowire is considered in contact with the substrate and the secondary nanowire is in free-standing configuration. This choice is motivated by SEM images which reveals that, in nanowire networks, junctions are often characterised by a nanowire in direct contact with the substrate and a second nanowire which rests on others as shown in Figure 4.6.

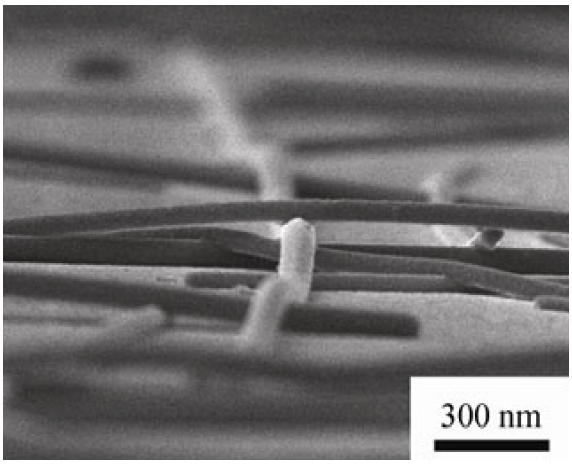

Figure 4.6. *SEM image of a cross-sectional view of an AgNW network. Two nanowires are in contact, with the primary one resting on the substrate and the secondary one resting on others, 'free-standing'. The image also reveals that the nanowires can bend and touch the substrate* [85].

However, since nanowires are mechanically flexible, the secondary nanowire can bend and touch the substrate, as can be seen in Figure 4.6. The presented model can represent such configuration, however, the full dependency on the bending arc is not considered in this work. Schematics of the studied configurations are shown in Figure 4.7.

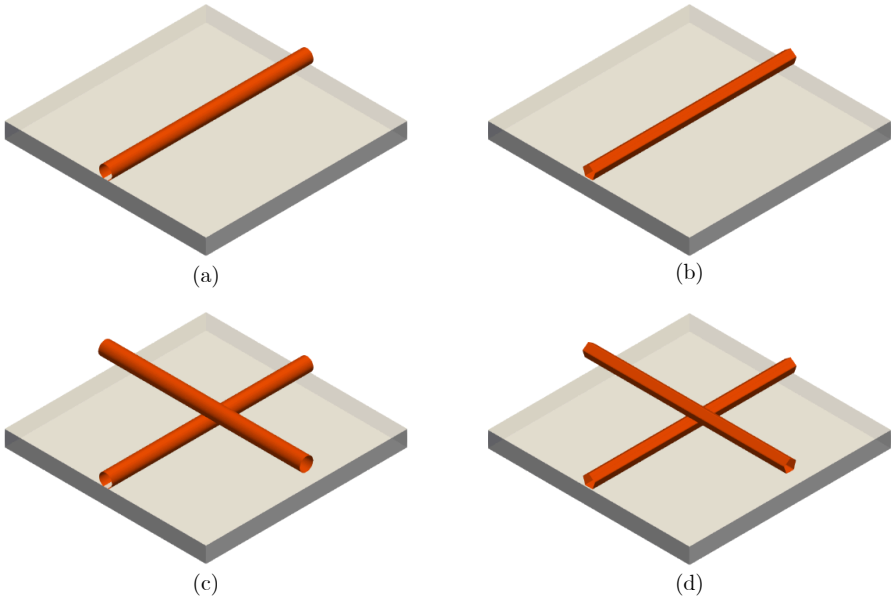

Figure 4.7. *Schematic of a* (a) *single nanowire on substrate with circular cross-section* (b) *single nanowire on substrate with pentagonal cross-section. The other two schematic are of a junction of two nanowires with* (c) *circular* (d) *pentagonal cross-section with the primary one in contact with the substrate.*

4.3 Comparative analysis

In order to assess the influence of the flat substrate on the morphological instability of the nanowires, a comparative analysis is performed between the results obtained in Chapter 3 and the results obtained in the present chapter. First, the case of a single nanowire is investigated in both the circular and pentagonal cross-section configurations. Both the breakup time t_b and the wavelength of the instability λ are studied in the same way as in Chapter 3. Finally, the case of a junction of two nanowires is considered with the primary nanowire in contact with the substrate and the secondary nanowire free-standing.
The sensitivity to numerical parameters yields similar results as in Chapter 3 and is not repeated here. Thus the computational box is taken sufficiently large to avoid boundary effects.

4.3.1 Single nanowire on substrate

Following the same methodology as in Chapter 3, the breakup time t_b and the wavelength of the instability λ are studied for both the circular and pentagonal cross-section configurations. The results are presented in Figure 4.8 and Figure 4.10 respectively. In this case the influence of the presence of a substrate is quantified for both the breakup time and the wavelength of the instability. The results are compared to the free-standing case presented in Chapter 3. The results are only presented for the case of a finite length nanowire since the breakup dynamics are similar to experimental observations as discussed in Chapter 3.

Numerical results show that the breakup time t_b/T^* is significantly influenced by the substrate consideration while still following a similar power law as in the free-standing case as figured in Figure 4.10. The relationship between the breakup time and the initial radius R/L^* writes,

$$t_b/T^* \approx \tau(\theta_B)(R/L^*)^{4.12} \ , \tag{4.18}$$

with $\tau(\theta_B) \approx 426.52K(\theta)$ the characteristic breakup time with respect to the contact angle θ_B.
Comparing the results to the free-standing case, for the case of a prescribed contact angle $\theta_B = 180°$, the curve is close and consistent with the reference case. The dependence on the prescribed contact angle θ_B is highlighted through a non-linear function of θ_B. An attempt to fit the numerical results is performed in Figure 4.9, where the numerical results are compared to McCallum's analytical model [18]. The numerical results are found to be consistent with the analytical model of McCallum *et al.* [18]. The normalized estimated growth rate $\tilde{\sigma}_m$ is found to have a similar sigmoid-like shape as the one predicted in their study. A slight discrepancy between a prescribed contact angle $\theta_B = 180°$ and the free-standing case is observed. The discrepancy is more apparent in Figure 4.11 where the morphological transformation of a free-standing nanowire is compared to the case of a prescribed contact angle $\theta_B = 180°$.

The wavelength of the instability λ/L^* is also studied using the same approach as in Chapter 3. The results are presented in Figure 4.10. Numerical fitting of the data reveals a linear relationship between the wavelength and the initial radius R/L^*. In addition, the slope of the linear fit is found to be dependent on the prescribed contact angle θ_B. The same slope is found for both the contact angle $\theta_B = 180°$ and the free-standing configuration, i.e. $\lambda \approx 6.47R$.

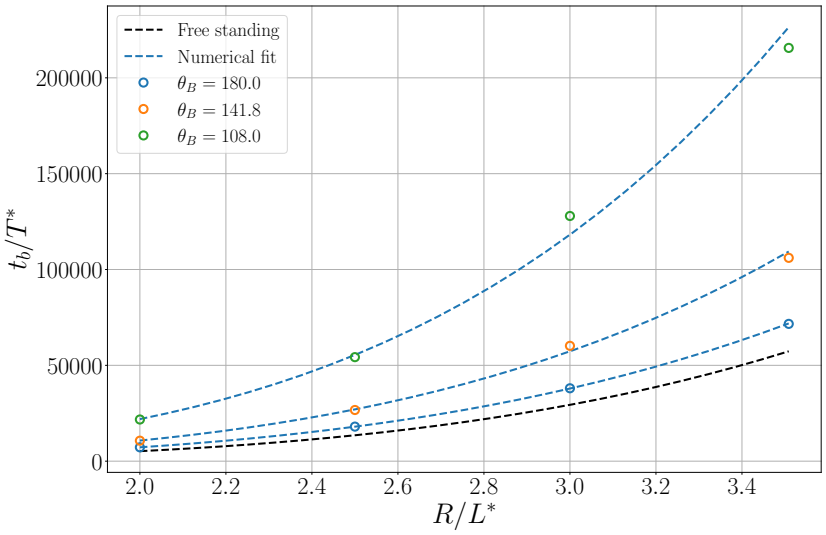

Figure 4.8. *Numerical results of the breakup time t_b/T^* with respect to the initial radius R/L^* for different values of the prescribed angle θ_B. Numerical fits reveal a power law relationship between both quantities. The power law is found to be consistent with the free-standing case, albeit with a different prefactor which is dependent on the prescribed angle θ_B. The results from the free-standing case are shown in black and are consistent with the prescribed contact angle $\theta_B = 180°$.*

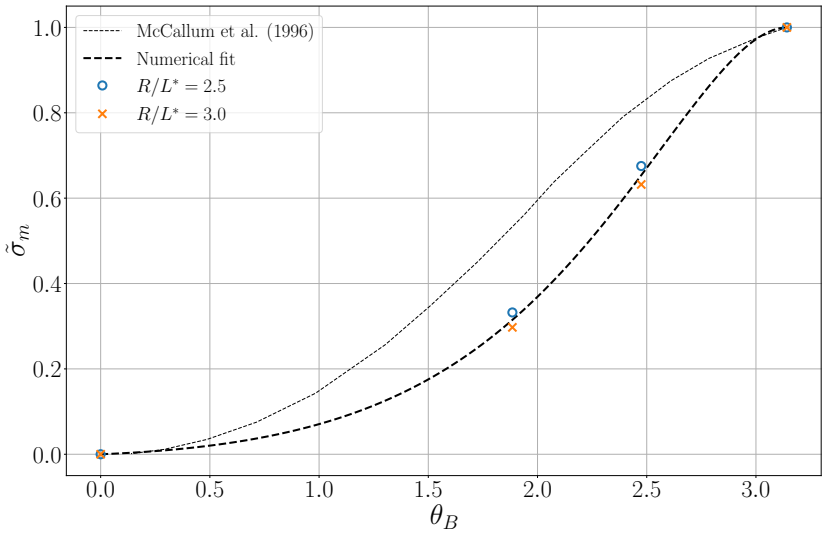

Figure 4.9. *Numerical fit of the relation between the prescribed angle θ_B and the scaled maximum growth rate $\tilde{\sigma}_m$. The numerical results are compared to McCallum's analytical model [18]. Both curves follow a sigmoid-like shape.*

For contact angles $\theta_B = 141.8°$ and $108°$, the wavelength is found to be $\lambda \approx 8.9R$ and $\lambda \approx 12.3R$ respectively. Additional numerical experiments on the pentagonal cross-section configuration with a contact angle $\theta_B = 108°$ yield a wavelength $\lambda \approx 7.6R$. In addition, the morphological transformation is found to be slower for the pentagonal approximation.

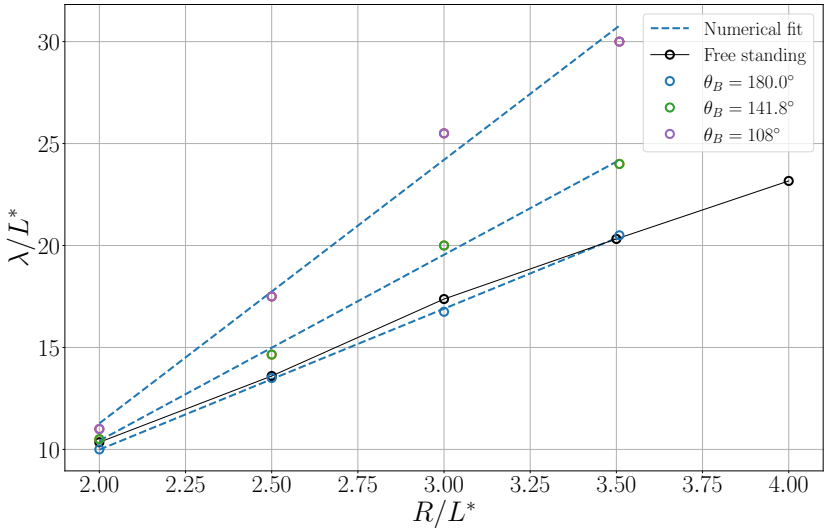

Figure 4.10. *Numerical results for the wavelength of the instability λ/L^* with respect the initial radius R/L^* for different values of the prescribed angle θ_B. Numerical fits reveal a linear relationship between both quantities. The slope is found to be dependent on the prescribed angle θ_B.*

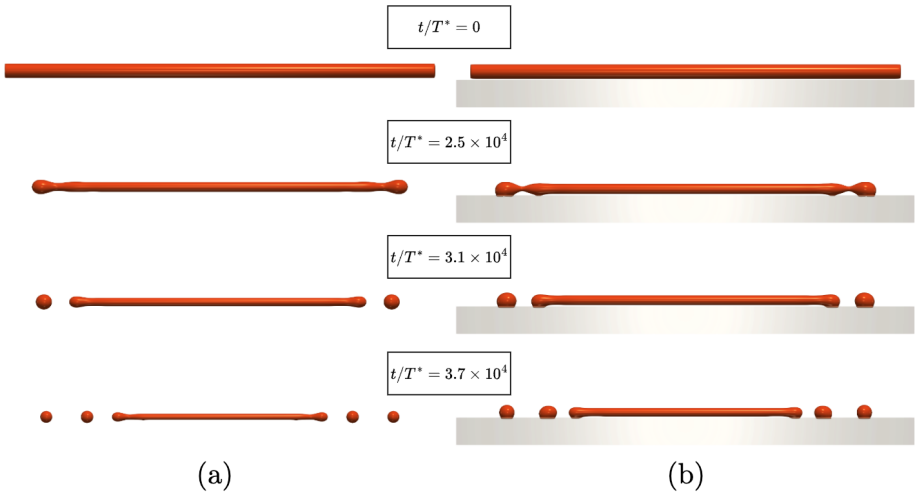

Figure 4.11. *Comparison of the morphological transformation between the free-standing model and the SBM model.* (a) *Free standing nanowire* (b) *Nanowire on substrate with a prescribed angle $\theta_B = 180°$. Both nanowires evolve at a similar rate, which further validates the SBM formalism.*

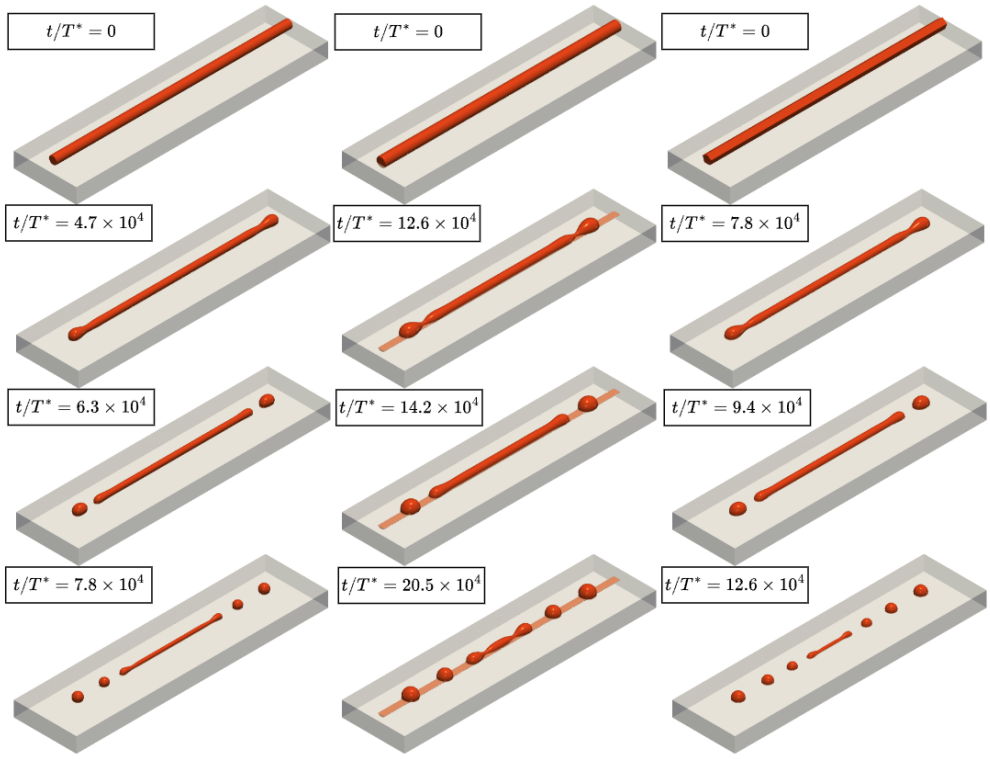

Figure 4.12. *Contour plot* ($c = 0.5$) *snapshots of the morphological transformation of a single nanowire on substrate with a prescribed contact angle* (a) $\theta_B = 141.8°$ *and* (b) $\theta_B = 108°$ (c) $\theta_B = 108°$ *(pentagonal cross-section). The observed configurations highlight the influence of the contact angle on the morphological transformation.*

4.3.2 Junction of nanowires on substrate

Similarly to the single nanowire case, a comparative analysis is performed for the junction configuration to assess the influence of the substrate on the junction overall stability. In particular, the free-standing configuration is compared to the substrate-supported (for the primary nanowire) configuration with a contact angle $\theta_B = 141°$. Snapshots of the morphological evolution at various time steps, shown in Figure 4.13, indidicate that the breakup times of the secondary nanowire $t_{b,2}$ in both configuration are comparable, yielding a ratio $t_{b,2}^{sub}/t_{b,2}^{free} \approx 1$. In contrast, for the primary nanowire, the presence of the substrate significantly delays the onset of ovulation and the subsequent fragmentation. Inspecting the ratio of breakup times, $t_{b,1}^{sub}/t_{b,1}^{free} \approx 2$, reveals a two-fold increase in the stability induced by the substrate.
In a second analysis, the influence of the prescribed contact angle is evaluated by comparing different substrate-supported configurations. The snapshots of the morphological transformation in Figure 4.14 reveal that the primary nanowire, in contact with the substrate, breaks up at later times compared to the secondary nanowire. However, when the secondary nanowire is in contact with the substrate, the junction is found to be slightly more stable, i.e. the minimum breakup time is larger than the other configurations.

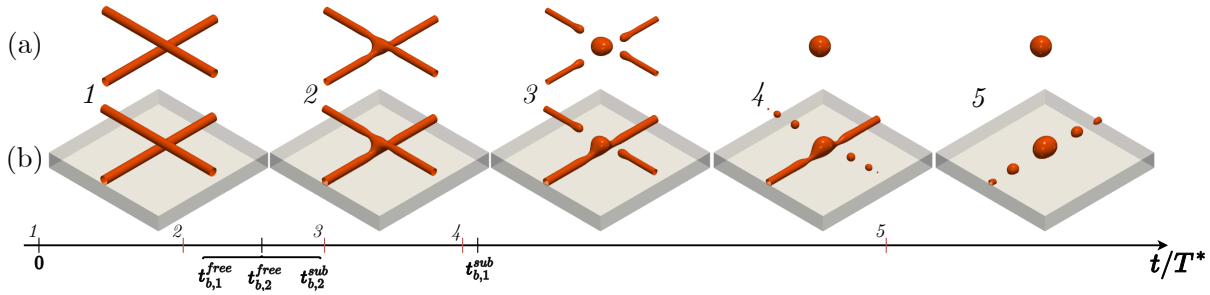

Figure 4.13. *Morphological transformation of a junction of nanowires with* (a) *free-standing primary nanowire* (b) *substrate supported primary nanowire with a prescribed angle* $\theta_B = 141.8°$ *and free-standing secondary nanowire. The breakup times of both nanowires are also denoted as (a)* $t^{free}_{b,i}$ *(b)* $t^{sub}_{b,i}$*. The free-standing secondary nanowire breaks at a similar time between the fully free-standing configuration and the substrate-supported configuration. The primary nanowire, on the other hand, breaks after a longer period of time.*

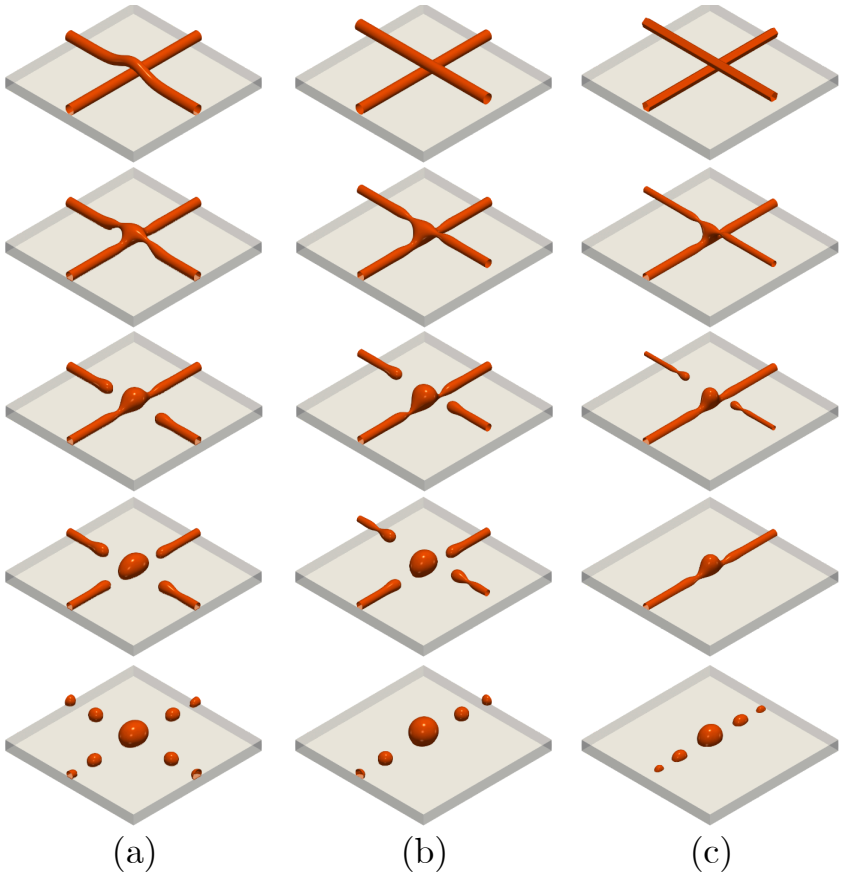

Figure 4.14. *Contour plot* ($c = 0.5$) *snapshot of the morphological instability of a junction in different configurations at different stages of transformation.* (a) *Two substrate-supported nanowires with a bended secondary nanowire* (b) *A substrate-supported nanowire with a free-standing nanowire* ((c) *pentagonal cross-section). The snapshots reveal a slight increase in the overall stability of the junction when both nanowires are in contact with the substrate.*

4.4 Discussion

The results obtained for substrate-deposited nanowires are found to be consistent with the theoretical and numerical findings of McCallum *et al.* [18], albeit here studied in the broader and more flexible context of the phase-field formalism. Notably, the same scaling laws identified in the free-standing case remain valid, reinforcing *a posteriori* the relevance of initially focusing on free-standing nanowires to capture the dominant mechanism of breakup dynamics. The substrate acts as a stabilizing constraint by restricting the admissible modes of perturbation, which in turn slows down the evolution and leads to an observable shift in the instability wavelength.

As shown in the free-standing simulations, the instability wavelength extracted from finite-length nanowires is close to the theoretically predicted critical wavelength [17]. When examining substrate-supported configurations, the maximally growing wavelength can similarly be estimated as a function of the prescribed contact angle θ_B, and the predictions align well with the results from McCallum *et al.* [18].

These observations support the conclusions of Balty *et al.*, where a reduction in the set of unstable modes due to geometric constraints leads to delayed breakup. However, it is also found that the actual spacing between nanodots in the free-standing case is consistently smaller than the maximally growing wavelength predicted by linear theory. This discrepancy persists even in more realistic geometries such as pentagonal cross-sections with $\theta_B = 108°$, where the observed wavelengths remain below those measured experimentally by Langley *et al.* [21] and Balty *et al.* [28].

Such differences strongly support the consideration of anisotropic effects in the model. Indeed, directional dependence of surface properties, arising from crystalline anisotropy, may substantially alter the selection of unstable modes and the breakup kinetics.

In the case of nanowire junctions, simulations reveal that the primary nanowire, in contact with the substrate, breaks up at significantly later times compared to its free-standing counterpart. This delayed breakup is attributed to the stabilizing influence of the substrate, which restricts available perturbation modes and slows the morphological evolution. Additional numerical experiments on approximated flexed nanowires show an increase in breakup time. These findings suggest that mild mechanical pressing might offer a potential strategy for enhancing thermal stability during annealing of nanowire networks, as also suggested in Tokuno *et al.* study, comparing mechanically pressed against thermal annealed nanowire network [85].

It is important to note, however, that this interpretation is made in the absence of any explicitly modeled mechanical strain. As previously discussed by Cahn [10], elastic stresses can strongly influence the chemical potential and the morphological stability of the structure.

Chapter 5

Conclusion and perspectives

The increasing demand for transparent electronics has stimulated research into alternatives to traditional transparent conducting materials. Silver nanowire networks have emerged as promising candidates thanks to their excellent electrical and optical properties. However, their limited thermal stability, manifested as morphological instability and breakup of nanowires at elevated temperatures, remains a major obstacle to their practical application.

The core objective of this thesis was first to further assess the relevance of phase-field modeling as a tool to study the morphological instability of metallic nanowires, and to develop a numerical framework to understand the breakup mechanism of metallic nanowires and subsequently to finally propose potential optimization strategies for stabilizing nanowire networks. Experimental studies have offered qualitative insights, but their limitations in capturing and generalizing the underlying mechanisms necessitate the use of robust numerical models. In this context, the phase-field method has gained traction as a flexible tool for modeling microstructural physics, and especially interface-driven morphological evolutions.

To tackle this problem, a phase-field framework based on the Cahn-Hilliard equation was adopted. The numerical implementation, introduced in Chapter 2, involved a Fourier spectral semi-implicit scheme. The solver was validated through numerical experiments and benchmarks, made available by the ever-growing phase-field community, to ensure consistency and convergence. A key extension in Chapter 4 involved the implementation of the Smoothed Boundary Method (SBM), allowing a diffuse representation of complex geometries and enforcement of custom boundary conditions, responding to the main limitation of spectral-based methods.

In Chapter 3, the framework was used to revisit and extend the earlier work of Roy *et al.* on nanowire breakup. The study focused on two geometrical configurations: a single free-standing nanowire and a junction of two free-standing nanowires. The results lead to the identification of power-law scaling relationships for the breakup time and the instability wavelength, consistent with theoretical predictions. In addition, a disentanglement of the two dominant breakup mechanisms was achieved: perturbation-driven, governed by the initial perturbations, and free-end-driven, initiated from the free ends of the nanowire. The results found the wavelength of the instability in finite nanowires to be smaller than the

expected maximally growing wavelength, as predicted by previous theoretical work. An extension to more realistic geometries was also performed, mainly the consideration of a pentagonal cross-section, which revealed accelerated breakup due to the initial faceting of the nanowire.

In Chapter 4, the model was generalized to study substrate-supported nanowires using SBM. The presence of the substate was shown to significantly alter the dynamics of the morphological instability, leading to slower dynamics and modified wavelength of instability. The observed effects were in agreement with the theoretical predictions by McCallum *et al.* for infinitely long cylindrical films. A comparative analysis between different prescribed contact angles revealed that the presence of the substrate does not alter the scaling laws derived for the free-standing case but instead modifies the instability landscape, mainly an increase of stability as the contact angle decreases, i.e. as the contact between the primary nanowire and the substrate increases.

The findings of this thesis establish the phase-field method as a robust and flexible tool for studying surface-driven morphological instabilities in metallic nanowires. The consistent reproduction of known scaling laws across various configurations validates its application to nanoscale systems and bridges a critical gap between theory, simulation, and experiment.

While the presented model captures the essential physics, the study also highlights limitations and room for improvement. Notably, the simplified isotropic surface energy approximation neglects crystallographic anisotropy, which is expected to play a substantial role in real systems. Furthermore, the absence of elastic effects, temperature-dependent diffusion parameters, and grain-boundary considerations limits the model's applicability to complex annealing scenarios. Finally, the present work would benefit from an experimental campaign to discuss the quantitative predictive fidelity of the presented model and to correctly identify the model parameters which best suit real-world nanowires.

To conclude, *an in-house computational framework to study the morphological instability of metallic nanowires was developed* and validated against known results from the literature. The numerical framework was also optimized by adapting and aiding the model by: implementing a diffuse filtering scheme to alleviate and diminish the emergence and propagation of unwanted numerical oscillations, adopting a semi-implicit scheme which alleviates the constraints on the discretisation parameters, and by implementing an adapted voxelisation scheme to define physically-consistent initial conditions.

In addition, *the relevance of the phase-field formalism* was assessed by constructing scaling laws in light of Balty *et al.* findings from their experimental work.
Finally, *different relevant configurations of metallic nanowires were explored* and shed light on possible optimization strategies to improve the stability of metallic nanowire network, mainly that an initial surface treatment of the substrate would lead to improved stability.

Perspectives for Future Work

Beyond the current scope, several promising directions could be explored to further enhance the physical accuracy and applicability of the phase-field model. Coupling the Cahn-Hilliard equation with the Allen-Cahn equation under the Kim-Kim-Suzuki formalism would allow tracking of the individual grains composing the nanowire, thereby enabling grain-boundary-driven phenomena to be captured explicitly. Such an approach also allows anisotropic behavior to be modeled via the non-conserved phase-field specific mobility L, enabling crystallographic orientation-dependent kinetics.

An alternative strategy for incorporating anisotropy would use the explicit definition of a surface energy density that depends on the interface normal, directly within the Cahn-Hilliard formulation. This would allow directional surface energy minimization effects to be accounted for without introducing an additional field variable.

Moreover, the phase-field formalism can be extended to multiphysics contexts by incorporating the correct energetic contributions of various physical fields like elastic strain, temperature, electric fields, and even magnetic interactions. Recent developments have introduced phase-field frameworks that couple electro-thermo-mechanical fields for modeling metallic interconnects [86]. This approach could be adapted to model the interplay between thermal, mechanical, and morphological effects in nanowire networks or explore different annealing strategies numerically.

Nevertheless, it should be acknowledged that the phase-field method remains computationally intensive, especially when targeting realistic 3D morphologies over long physical timescales. Future work may also investigate optimization strategies aimed at reducing computational overhead. Leveraging on the sheer amount of data that the phase-field model outputs, data-driven surrogate models could be a promising route to reduce the computational overhead of the model and allow the consideration of more complex multi-physics coupling.

Declaration on AI-assisted technologies in the writing process

The author declares that the content of this thesis is the product of his own personal work, research and ideas, and that any use of AI-assisted technologies has been done solely for the rephrasing of text, without any contribution to the content of ideas or the structure of the thesis.

Bibliography

[1] D. Bellet et al. “Transparent Electrodes Based on Silver Nanowire Networks: From Physical Considerations towards Device Integration”. In: *Materials* 10.6 (June 2017). DOI: 10.3390/ma10060570.

[2] S. K. Maurya et al. “Recent Progress in Transparent Conductive Materials for Photovoltaics”. In: *Energies* 15.22 (Jan. 2022). DOI: 10.3390/en15228698.

[3] V. H. Nguyen et al. “Advances in Flexible Metallic Transparent Electrodes”. In: *Small* 18.19 (2022), p. 2106006. DOI: 10.1002/smll.202106006.

[4] H. Sohn et al. “Silver Nanowire Networks: Mechano-Electric Properties and Applications”. In: *Materials* 12.16 (Jan. 2019). DOI: 10.3390/ma12162526.

[5] Y. Sun et al. “Polyol Synthesis of Uniform Silver Nanowires: A Plausible Growth Mechanism and the Supporting Evidence”. In: *Nano Lett.* 3.7 (July 2003), pp. 955–960. DOI: 10.1021/nl034312m.

[6] J. Jiu and K. Suganuma. “Metallic Nanowires and Their Application”. In: *IEEE Transactions on Components, Packaging and Manufacturing Technology* 6.12 (Dec. 2016), pp. 1733–1751. DOI: 10.1109/TCPMT.2016.2581829.

[7] M. Lagrange et al. “Optimization of silver nanowire-based transparent electrodes: Effects of density, size and thermal annealing”. In: *Nanoscale* 7 (Oct. 2015). DOI: 10.1039/C5NR04084A.

[8] J. W. Cahn and J. E. Hilliard. “Free Energy of a Nonuniform System. I. Interfacial Free Energy”. In: *The Journal of Chemical Physics* 28.2 (Feb. 1958), pp. 258–267. DOI: 10.1063/1.1744102.

[9] J. W. Cahn. “Free Energy of a Nonuniform System. II. Thermodynamic Basis”. In: *The Journal of Chemical Physics* 30.5 (May 1959), pp. 1121–1124. DOI: 10.1063/1.1730145.

[10] J. W. Cahn. “On spinodal decomposition”. In: *Acta Metallurgica* 9.9 (Sept. 1961), pp. 795–801. DOI: 10.1016/0001-6160(61)90182-1.

[11] D. Lee et al. “Physical, mathematical, and numerical derivations of the Cahn–Hilliard equation”. In: *Computational Materials Science* 81 (Jan. 2014), pp. 216–225. DOI: 10.1016/j.commatsci.2013.08.027.

[12] J. Zhu et al. "Coarsening kinetics from a variable-mobility Cahn-Hilliard equation: Application of a semi-implicit Fourier spectral method". In: *Phys. Rev. E* 60.4 (Oct. 1999), pp. 3564–3572. DOI: 10.1103/PhysRevE.60.3564.

[13] J. S. Langer, M. Bar-on, and H. D. Miller. "New computational method in the theory of spinodal decomposition". In: *Phys. Rev. A* 11.4 (Apr. 1975), pp. 1417–1429. DOI: 10.1103/PhysRevA.11.1417.

[14] A. Roy, A. Varma, and M. P. Gururajan. "Phase-field study of surface diffusion enhanced break-ups of nanowire junctions". 2021.

[15] H.-C. Yu, H.-Y. Chen, and K. Thornton. "Extended smoothed boundary method for solving partial differential equations with general boundary conditions on complex boundaries". In: *Modelling Simul. Mater. Sci. Eng.* 20.7 (Oct. 2012), p. 075008. DOI: 10.1088/0965-0393/20/7/075008.

[16] F. A. Nichols and W. W. Mullins. "Morphological Changes of a Surface of Revolution due to Capillarity-Induced Surface Diffusion". In: *Journal of Applied Physics* 36.6 (June 1965), pp. 1826–1835. DOI: 10.1063/1.1714360.

[17] F. A. Nichols. "On the spheroidization of rod-shaped particles of finite length". In: *Journal of Materials Science* 11.6 (June 1976), pp. 1077–1082. DOI: 10.1007/BF02396641.

[18] M. S. McCallum et al. "Capillary instabilities in solid thin films: Lines". In: *Journal of Applied Physics* 79.10 (May 1996), pp. 7604–7611. DOI: 10.1063/1.362343.

[19] L. Bardet et al. "Silver Nanowire Networks: Ways to Enhance Their Physical Properties and Stability". In: *Nanomaterials* 11 (Oct. 2021), p. 2785. DOI: 10.3390/nano11112785.

[20] Kevin F. Brennan. "Introduction to semiconductor devices: for computing and telecommunications applications". en. 1. paperback print. Cambridge: Cambridge Univ. Press, 2010. ISBN: 978-0-521-83150-5 978-0-521-15361-4.

[21] D. Langley et al. "Flexible transparent conductive materials based on silver nanowire networks: a review". In: *Nanotechnology* 24.45 (Nov. 2013), p. 452001. DOI: 10.1088/0957-4484/24/45/452001.

[22] G. Haacke. "New figure of merit for transparent conductors". In: *Journal of Applied Physics* 47.9 (Sept. 1976), pp. 4086–4089. DOI: 10.1063/1.323240.

[23] S. Bergin et al. "The effect of nanowire length and diameter on the properties of transparent, conducting nanowire films". In: *Nanoscale* 4 (Mar. 2012), pp. 1996–2004. DOI: 10.1039/c2nr30126a.

[24] D. P. Langley et al. "Metallic nanowire networks: effects of thermal annealing on electrical resistance". In: *Nanoscale* 6.22 (2014), pp. 13535–13543. DOI: 10.1039/C4NR04151H.

[25] J. A. F. Plateau. "Statique expérimentale et théorique des liquides soumis aux seules forces moléculaires". Gauthier-Villars, 1873.

[26] Lord Rayleigh. "On The Instability Of Jets". In: *Proceedings of the London Mathematical Society* 10.1 (1878), pp. 4–13. DOI: 10.1112/plms/s1-10.1.4.

[27] D. F. Rutland and G. J. Jameson. "A non-linear effect in the capillary instability of liquid jets". In: *J. Fluid Mech.* 46.2 (Mar. 1971), pp. 267–271. DOI: 10.1017/S0022112071000521.

[28] F. Balty et al. "Insight into the morphological instability of metallic nanowires under thermal stress". In: *Journal of Colloid and Interface Science* 673 (Nov. 2024), pp. 574–582. DOI: 10.1016/j.jcis.2024.06.074.

[29] M. E. Tuckerman and G. J. Martyna. "Understanding Modern Molecular Dynamics: Techniques and Applications". In: *J. Phys. Chem. B* 104.2 (Jan. 2000), pp. 159–178. DOI: 10.1021/jp992433y.

[30] A. Bartels and J. Mosler. "On the variational formulation and implementation of Allen-Cahn and Cahn-Hilliard-type phase field theories". In: *PAMM* 15.1 (2015), pp. 273–274. DOI: 10.1002/pamm.201510127.

[31] P. Voorhees. "Lectures on Phase Field Modeling". https://github.com/usnistgov/pfhub/wiki/Peter-Voorhees-Lectures. 2018.

[32] N. Moelans, B. Blanpain, and P. Wollants. "An introduction to phase-field modeling of microstructure evolution". In: *Calphad* 32.2 (June 2008), pp. 268–294. DOI: 10.1016/j.calphad.2007.11.003.

[33] S. B. Biner. "Programming Phase-Field Modeling". Cham: Springer International Publishing, 2017. DOI: 10.1007/978-3-319-41196-5.

[34] D. Wheeler et al. "PFHub: The Phase-Field Community Hub". In: *JORS* 7.1 (Sept. 2019), p. 29. DOI: 10.5334/jors.276.

[35] 'PFHub. "The Phase Field Community Hub'". Accessed: Aug. 16. 2024. URL: https://pages.nist.gov/pfhub/.

[36] H. Emmerich. "Advances of and by phase-field modelling in condensed-matter physics". In: *Advances in Physics* 57.1 (Jan. 2008), pp. 1–87. DOI: 10.1080/00018730701822522.

[37] G. Gottstein. "Physical Foundations of Materials Science". Berlin, Heidelberg: Springer Berlin Heidelberg, 2004. DOI: 10.1007/978-3-662-09291-0.

[38] A. M. Jokisaari et al. "Benchmark problems for numerical implementations of phase field models". In: *Computational Materials Science* 126 (Jan. 2017), pp. 139–151. DOI: 10.1016/j.commatsci.2016.09.022.

[39] J. S. Langer, M. Bar-on, and H. D. Miller. "New computational method in the theory of spinodal decomposition". In: *Phys. Rev. A* 11.4 (Apr. 1975), pp. 1417–1429. DOI: 10.1103/PhysRevA.11.1417.

[40] H. Wu. "A Review on the Cahn-Hilliard Equation: Classical Results and Recent Advances in Dynamic Boundary Conditions". In: *era* 30.8 (2022), pp. 2788–2832. DOI: 10.3934/era.2022143.

[41] X. Xiao, X. Feng, and Z. Shi. "Efficient numerical simulation of Cahn-Hilliard type models by a dimension splitting method". In: *Computers & Mathematics with Applications* 136 (Apr. 2023), pp. 54–70. DOI: 10.1016/j.camwa.2023.01.037.

[42] F. Xue et al. "Phase-field framework with constraints and its applications to ductile fracture in polycrystals and fatigue". In: *npj Comput Mater* 8.1 (Jan. 2022), pp. 1–15. DOI: 10.1038/s41524-022-00700-2.

[43] J. Kim. "A generalized continuous surface tension force formulation for phase-field models for multi-component immiscible fluid flows". In: *Computer Methods in Applied Mechanics and Engineering* 198.37 (Aug. 2009), pp. 3105–3112. DOI: 10.1016/j.cma.2009.05.008.

[44] S. G. Kim and W. T. Kim. "Phase-Field Modeling of Solidification". In: *Handbook of Materials Modeling: Methods*. Ed. by S. Yip. Dordrecht: Springer Netherlands, 2005, pp. 2105–2116. DOI: 10.1007/978-1-4020-3286-8_109.

[45] A. Cartalade et al. "Simulations of Phase-field Models for Crystal Growth and Phase Separation". In: *Procedia Materials Science* 7 (Jan. 2014), pp. 72–78. DOI: 10.1016/j.mspro.2014.10.010.

[46] B. König, O. J. J. Ronsin, and J. Harting. "Two-dimensional Cahn–Hilliard simulations for coarsening kinetics of spinodal decomposition in binary mixtures". In: *Phys. Chem. Chem. Phys.* 23.43 (2021), pp. 24823–24833. DOI: 10.1039/D1CP03229A.

[47] K. Chockalingam et al. "2D Phase field modeling of sintering of silver nanoparticles". In: *Computer Methods in Applied Mechanics and Engineering* 312 (Dec. 2016), pp. 492–508. DOI: 10.1016/j.cma.2016.07.002.

[48] C. Pesce and A. Münch. "How do degenerate mobilities determine singularity formation in Cahn-Hilliard equations?" Accessed: Apr. 24, 2024. Jan. 13, 2021. arXiv: arXiv:2101.05116. URL: http://arxiv.org/abs/2101.05116.

[49] J. W. Cahn and J. E. Taylor. "Surface motion by surface diffusion". In: *Acta Metallurgica et Materialia* 42.4 (Apr. 1994), pp. 1045–1063. DOI: 10.1016/0956-7151(94)90123-6.

[50] Abhinav Roy. "Variable Mobility Cahn-Hilliard Equation: Numerical Formulation and Algorithm". 2021. DOI: 10.13140/RG.2.2.29738.13760/4.

[51] D. Li and T. Tang. "Stability analysis for the Implicit-Explicit discretization of the Cahn-Hilliard equation". arXiv.org, , Accessed: Feb. 28, 2024. Aug. 2020. URL: http://arxiv.org/abs/2008.03701.

[52] G. E. Rhead. "Surface self-diffusion and faceting on silver". In: *Acta Metallurgica* 11.9 (Sept. 1963), pp. 1035–1042. DOI: 10.1016/0001-6160(63)90191-3.

[53] T. Wejrzanowski and K. J. Kurzydlowski. "Modeling of Size Effects in Diffusion Driven Processes at Nanoscale - Large Atomic and Mesoscale Methods". In: *DF* 12 (Sept. 2017), pp. 38–73. DOI: 10.4028/www.scientific.net/DF.12.38.

[54] L. Q. Chen and J. Shen. "Applications of semi-implicit Fourier-spectral method to phase field equations. Computer Physics Communications, 108(2-3), 147–158 | 10.1016/s0010-4655(97)00115-x". In: *Computer Physics Communications* 108.2 (Feb. 1998), pp. 147–158. DOI: 10.1016/S0010-4655(97)00115-X.

[55] S. Širca and M. Horvat. "Spectral Methods for PDE". In: *Physicists: Compendium for Students, S. Sirca and M. Horvat, Eds., Berlin*. Ed. by Computational Methods for. Heidelberg: Springer, 2012, pp. 575–620. DOI: 10.1007/978-3-642-32478-9_11.

[56] P. J. Olver. "Introduction to Partial Differential Equations". Undergraduate Texts in Mathematics. Cham: Springer International Publishing, 2014. DOI: 10.1007/978-3-319-02099-0.

[57] A. Sinhababu and A. Bhattacharya. "A pseudo-spectral based efficient volume penalization scheme for Cahn–Hilliard equation in complex geometries". In: *Mathematics and Computers in Simulation* 199 (Sept. 2022), pp. 1–24. DOI: 10.1016/j.matcom.2022.03.015.

[58] B. Fornberg. "A Practical Guide to Pseudospectral Methods". In: *on Applied and Computational Mathematics*. Ed. by Cambridge Monographs. Cambridge: Cambridge University Press, 1996. DOI: 10.1017/CBO9780511626357.

[59] J. Ansel et al. "PyTorch 2: Faster Machine Learning Through Dynamic Python Bytecode Transformation and Graph Compilation". In: *Proceedings of the 29th ACM International Conference on Architectural Support for Programming Languages and Operating Systems, Volume 2, La Jolla CA USA: ACM, Apr. 2024*. Apr. 2024, pp. 929–947. DOI: 10.1145/3620665.3640366.

[60] C. Geuzaine and J.-F. Remacle. "Gmsh: a three-dimensional finite element mesh generator with built-in pre- and post-processing facilities". In: *Int. J. Numer. Meth. Engng* ().

[61] U. Ayachit. "The ParaView Guide: A Parallel Visualization Application". Accessed: Aug. 20, 2024. Jan. 2015. URL: https://www.semanticscholar.org/paper/The-ParaView-Guide.

[62] R. C. Ball, T. M. A. Fink, and N. E. Bowler. "Stochastic Annealing". In: *Phys. Rev. Lett.* 91.3 (July 2003), p. 030201. DOI: 10.1103/PhysRevLett.91.030201.

[63] Mitko Aleksandrov, Sisi Zlatanova, and David Heslop. "Voxelisation Algorithms and Data Structures: A Review". In: *Sensors* 21 (Dec. 2021), p. 8241. DOI: 10.3390/s21248241.

[64] N. D. Katopodes. "Chapter 13 - Level Set Method". In: *Free-Surface Flow*. Ed. by N. D. Katopodes. Butterworth-Heinemann, 2019, pp. 804–828. DOI: 10.1016/B978-0-12-815485-4.00019-X.

[65] A. A. Sonin. "Department of Mechanical Engineering MIT Cambridge, MA 02139".

[66] Z. Mao and M. J. Demkowicz. "Mobility inference of the Cahn–Hilliard equation from a model experiment". In: *Journal of Materials Research* 36.13 (July 2021), pp. 2830–2842. DOI: 10.1557/s43578-021-00266-7.

[67] P. G. K. Amos et al. "Mechanisms of pearlite spheroidization: Insights from 3D phase-field simulations". In: *Acta Materialia* 161 (Dec. 2018), pp. 400–411. DOI: 10.1016/j.actamat.2018.09.043.

[68] E. Marzbanrad et al. "How morphology and surface crystal texture affect thermal stability of a metallic nanoparticle: the case of silver nanobelts and pentagonal silver nanowires". In: *Physical Chemistry Chemical Physics* 17.1 (2015), pp. 315–324. DOI: 10.1039/C4CP04129A.

[69] V. N. Gorshkov, V. V. Tereshchuk, and P. Sareh. "Diversity of anisotropy effects in the breakup of metallic FCC nanowires into ordered nanodroplet chains". In: *CrystEngComm* 22.15 (2020), pp. 2601–2611. DOI: 10.1039/C9CE01893J.

[70] C. Liang and Y. Yu. "Understanding the formation of multiply twinned structure in decahedral intermetallic nanoparticles". In: *IUCrJ* 6 (2019), pp. 447–453. DOI: https://doi.org/10.1107/S2052252519002562.

[71] A. Roy and M. P. Gururajan. "Phase Field Modelling of Morphologies Driven by Tetragonal Interfacial Energy Anisotropy". In: *Crystal Growth & Design* 21.3 (Mar. 2021), pp. 1591–1603. DOI: 10.1021/acs.cgd.0c01424.

[72] P. Bellon and Q. Li. "Anisotropic Cahn-Hilliard free energy and interfacial energies for binary alloys with pairwise interactions". In: *Acta Materialia* 215 (Aug. 2021), p. 117041. DOI: 10.1016/j.actamat.2021.117041.

[73] S. Torabi et al. "A New Method for Simulating Strongly Anisotropic Cahn-Hilliard Equations". Vol. 3. Jan. 2007.

[74] S. Torabi et al. "A new phase-field model for strongly anisotropic systems". In: *Proc. R. Soc. A.* 465.2105 (May 2009), pp. 1337–1359. DOI: 10.1098/rspa.2008.0385.

[75] P. G. Kubendran Amos et al. "Phase-field analysis of volume-diffusion controlled shape-instabilities in metallic systems-II: Finite 3-dimensional rods". In: *Computational Materials Science* 144 (Mar. 2018), pp. 374–385. DOI: 10.1016/j.commatsci.2017.12.046.

[76] H.-C. Yu, H.-Y. Chen, and K. Thornton. "Smoothed Boundary Method for Solving Partial Differential Equations with General Boundary Conditions on Complex Boundaries". Accessed: Aug. 14, 2024. Dec. 7, 2009. arXiv: arXiv:0912.1288. URL: http://arxiv.org/abs/0912.1288.

[77] J. Yang, J. Wang, and J. Kim. "Energy-stable method for the Cahn–Hilliard equation in arbitrary domains". In: *International Journal of Mechanical Sciences* 228 (Aug. 2022), p. 107489. DOI: 10.1016/j.ijmecsci.2022.107489.

[78] Y. Li, J.-I. Choi, and J. Kim. "Multi-component Cahn–Hilliard system with different boundary conditions in complex domains". In: *Journal of Computational Physics* 323 (Oct. 2016), pp. 1–16. DOI: 10.1016/j.jcp.2016.07.017.

[79] A. Bueno-Orovio and V. M. Pérez-García. "Spectral smoothed boundary methods: The role of external boundary conditions". In: *Numerical Methods Partial* 22.2 (Mar. 2006), pp. 435–448. DOI: 10.1002/num.20103.

[80] Alfonso Bueno-Orovio, Víctor M. Pérez-García, and Flavio H. Fenton. "Spectral Methods for Partial Differential Equations in Irregular Domains: The Spectral Smoothed Boundary Method". In: *SIAM Journal on Scientific Computing* 28.3 (2006), pp. 886–900. DOI: 10.1137/040607575. eprint: https://doi.org/10.1137/040607575. URL: https://doi.org/10.1137/040607575.

[81] A. Bueno-Orovio. "Fourier embedded domain methods: Periodic and Cinf extension of a function defined on an irregular region to a rectangle via convolution with Gaussian

kernels". In: *Applied Mathematics and Computation* 183.2 (2006), pp. 813–818. DOI: https://doi.org/10.1016/j.amc.2006.06.029.

[82] H. G. Lee and J. Kim. "Accurate contact angle boundary conditions for the Cahn–Hilliard equations". In: *Computers & Fluids* 44.1 (May 2011), pp. 178–186. DOI: 10.1016/j.compfluid.2010.12.031.

[83] J. A. Warren et al. "Phase field approach to heterogeneous crystal nucleation in alloys". In: *Phys. Rev. B* 79.1 (Jan. 2009), p. 014204. DOI: 10.1103/PhysRevB.79.014204.

[84] C. A. Schneider, W. S. Rasband, and K. W. Eliceiri. "NIH Image to ImageJ: 25 years of image analysis". In: *Nature Methods* 9.7 (2012), pp. 671–675. DOI: 10.1038/nmeth.2089.

[85] T. Tokuno et al. "Fabrication of silver nanowire transparent electrodes at room temperature". In: *Nano Res.* 4.12 (Dec. 2011), pp. 1215–1222. DOI: 10.1007/s12274-011-0172-3.

[86] X.-W. Wu, M. Chen, and L.-L. Ke. "An electro-thermo-mechanical coupling phase-field model of defect evolution induced by electromigration in interconnects". In: *International Journal of Mechanical Sciences* 285 (Jan. 2025), p. 109792. DOI: 10.1016/j.ijmecsci.2024.109792.